

Performance of a Passive, Wireless, Resonant Force Sensor for Smart Orthopedic Implants

Dustin Schroeder

Submitted in Partial Fulfillment of the Requirements
for the Degree of

MASTER OF SCIENCE

Approved by:

Eric H. Ledet, Ph.D., Thesis Adviser

Deva Chan, Ph.D., Member

Deanna Thompson, Ph.D., Member



Department of Biomedical Engineering
Rensselaer Polytechnic Institute
Troy, New York

[August 2020]
Submitted June 2020

© Copyright 2020
By
Dustin Schroeder
All Rights Reserved

TABLE OF CONTENTS

LIST OF TABLES	viii
LIST OF FIGURES	x
ACKNOWLEDGEMENT	xviii
ABSTRACT	xx
1. INTRODUCTION	1
1.1 Spine Anatomy	1
1.1.1 Bony Anatomy	1
1.1.2 Disc Anatomy	2
1.1.3 Spine Biomechanics.....	3
1.1.4 Biomechanical Spine Models	4
1.2 Disc Degeneration	7
1.2.1 Etiology.....	7
1.2.2 Biomechanics	7
1.2.3 Pathology	8
1.2.4 Prevalence of Neck Pain.....	9
1.3 Degenerative Disc Disease Management	9
1.3.1 Treatment Methods	9
1.3.2 Anterior Cervical Discectomy and Fusion.....	10
1.3.3 Fusion Effects on Spine Biomechanics.....	11
1.4 Smart Implants.....	12
1.4.1 Smart Spinal Implants.....	12
1.4.2 Smart Interbody Implants	14
1.5 Passive Resonator Sensors	17
1.5.1 Overview of Resonant Sensor Function	17
1.5.2 Measuring Resonant Frequency.....	18
1.5.3 Biomedical Applications of Passive Resonant Sensors	20
1.5.4 Advantages Over Conventional Sensors in Instrumentation	22
2. PROBLEM STATEMENT AND SPECIFIC AIMS	24
3. SPECIFIC AIM 1: METHODS.....	25
3.1 Sensor Model Derivation.....	25

3.2	Frequency Behavior.....	25
3.3	Inductive Behavior and Mathematical Derivation	26
3.3.1	Coil Inductance	28
3.3.2	Mutual Inductance	30
3.4	Capacitive Behavior and Mathematical Derivation	31
3.4.1	Coil Capacitance	31
3.4.2	Mutual Capacitance	37
3.5	Resistive Behavior and Mathematical Derivation.....	39
3.6	Mechanical Behavior and Mathematical Derivation.....	39
4.	SPECIFIC AIM 1: RESULTS.....	42
5.	SPECIFIC AIM 2A: RATIONALE BEHIND SENSOR DESIGN	45
5.1	Disc Morphometry.....	45
5.2	Expected Loads in the Cervical Spine.....	47
5.3	Sensor Design to Facilitate Fusion	48
5.4	Considerations for Fabrication	49
5.4.1	Examples of Manufactured Coils/Sensors	50
5.4.2	PCB as a Candidate Fabrication Method	52
5.4.3	PCB Manufacture and Material Properties	52
5.5	Final Design Constraints	54
5.6	EAGLE Designs	55
5.6.1	First Generation Coil Designs.....	55
5.6.2	Second Generation Coil Designs	56
5.6.3	Third Generation Coil Designs	60
5.7	Intervening Layer Selection	61
5.7.1	Candidate Materials for the Intervening Layer.....	61
5.7.2	Suitability of Parylene C for Force Sensors.....	63
6.	SPECIFIC AIM 2A: METHODS	66
6.1	Coil Design and Manufacture.....	66
6.2	Preparing Coils for Parylene Deposition.....	66
6.3	Parylene Layer Deposition	67
6.4	Coil Bonding	69

6.5	SEM Measurement of Deposition Thickness	70
6.6	SEM Imaging of Parylene Deposition Quality	70
7.	SPECIFIC AIM 2A: RESULTS	72
7.1	Coil Manufacture and Characterization.....	72
7.1.1	First Generation Coils	72
7.1.2	Second Generation Coils.....	74
7.1.3	Third Generation Coils	75
7.2	Coil Preparation for Parylene Deposition.....	77
7.3	Parylene Deposition.....	79
7.4	Sensor Bonding	82
7.5	Thickness Measurement	85
7.6	Parylene C Deposition Quality	90
7.7	Challenges in Sensor Manufacturing Quality.....	93
8.	SPECIFIC AIM 2B: EXPERIMENTAL PROTOCOL	97
8.1	Coil Characterization.....	97
8.1.1	Measuring Resonant Frequency.....	97
8.1.2	Measuring Coil L and C.....	99
8.2	Test Setup	100
8.2.1	Coil and Antenna Setup	100
8.2.2	MTS and Extensometer Setup	101
8.3	Air Gap Displacement Protocol.....	104
8.4	Solid Sensor Compression Protocol	106
8.5	Fabrication and Characterization of Solid Sensors with Varying Thicknesses.....	108
9.	SPECIFIC AIM 2B: RESULTS	109
9.1	Results of Coil Characterization.....	109
9.1.1	Designed Coil Characterization	109
9.1.2	Other Coil Characterization	112
9.1.3	Parylene C Coated Coil Characterization	113
9.2	Analysis of Coil Characterization	114
9.3	Results of Air Sensor Testing.....	118

9.4	Analysis of Air Sensor Testing.....	122
9.4.1	Model Accuracy for Air Sensors	122
9.4.2	Challenges in Air Sensor Measurement.....	129
9.5	Results of Frequency-Force Behavior	132
9.6	Analysis of Frequency-Force Behavior (Sensitivity)	135
9.7	Varying Thickness Parylene C Layers	138
9.7.1	Results of Fabrication and Testing of Varying Thickness Sensors	138
9.7.2	Analysis of Varying Thickness Sensors	139
10.	DISCUSSION	141
10.1	Implications of Modeling Resonant Sensor Behavior.....	141
10.1.1	Passive Resonant Force Sensor Physics	141
10.1.2	Model Iteration and Refinement	141
10.1.3	Improvements and Future Work	142
10.1.4	Significance and Translation.....	143
10.2	Implications of Rapid Prototyping of Force Sensors	143
10.2.1	Sensor Design Constraints	143
10.2.2	PCB Fabrication Methods.....	144
10.2.3	Modified Parylene C Deposition	145
10.2.4	Improvements and Future Work	146
10.2.5	Significance and Translation.....	147
10.3	Implications of Accurate Predictability of Resonant Force Sensors	147
10.3.1	Coil Model Validation	147
10.3.2	Air Sensor Model Validation	147
10.3.3	Solid Sensor Model Validation.....	148
10.3.4	Improvements and Future Work	149
10.3.5	Significance and Translation.....	149
10.4	Overall Significance	149
11.	CONCLUSION	151
	REFERENCES	152
	APPENDICES	171
	Appendix A Additional Figures	171

A.1	Gen 1 Air Sensor Figures.....	171
A.2	Gen 2 Air Sensor Figures.....	174
A.3	Gen 3 Air Sensor Figures.....	177
A.4	Gen 1 Solid Sensor Figures.....	178
A.5	Gen 2 Solid Sensor Figures.....	181
A.6	Gen 3 Solid Sensor Figures.....	185
A.7	Gen 1 Sensitivities for Solid Sensors.....	188
A.8	Gen 2 Sensitivities for Solid Sensors.....	189
A.9	Gen 3 Sensitivities for Solid Sensors.....	189
Appendix B Permissions		189
B.1	Permissions for Section 1.....	189
B.2	Permissions for Section 5.....	190

LIST OF TABLES

Table 1: Mean lower cervical spine interbody space morphologies.	46
Table 2: Mean lower cervical spine disc heights.	46
Table 3: Relevant material properties of FR4 substrates used in force sensor development, manufacture, and testing [87]-[90].	53
Table 4: Engineering constraints derived from physiological constraints and manufacturing constraints.	54
Table 5: First-generation coil design parameters.	55
Table 6: Minimum and maximum geometric parameter constraints for second-generation coil parametric study.	57
Table 7: Geometric parameters of the selected second-generation designs.	59
Table 8: Selection of polymers and ceramic composites that are close to or fit within the defined intervening layer mechanical and electrical constraints.	62
Table 9: Relevant material properties of parylene C for force sensors [97]-[100].	64
Table 10: SEM measured thicknesses and their respective input dimer masses. *Indicates sensor is product of two deposition runs.	88
Table 11: SEM measured parylene C thicknesses across their entire diameter.	94
Table 12: Measured geometric parameter means in first generation designs.	109
Table 13: Measured geometric parameter means in second generation designs.	110
Table 14: Measured geometric parameter means in third generation designs.	110
Table 15: Mean measured coil resonant frequencies in MHz.	111
Table 16: Coil viability in each generation.	111
Table 17: Additional coil geometries measured for model validation.	112
Table 18: Mean measured frequencies (in MHz) of large PCB coils and microfabricated coils for further model validation.	113

Table 19: Comparison of measured and predicted resonant frequencies for third generation coils with 0, 36, and 54 μ m thick layers of parylene C.....	113
Table 20: Percent errors of predicted coil behavior. Red and orange shading indicate error less than 5% and 10%, respectively.	115
Table 21: Percent errors of predicted frequency behavior for additional PCB and microfabricated coils. Green and red shading indicate error less than 5% and 10%, respectively. Gray indicates errors outside of 10%.....	116
Table 22: Percent errors of predicted resonant frequencies for parylene coated coils.	118
Table 23: Percent errors of predictions for first generation air sensors over a 50-1000 μ m range.	123
Table 24: Percent errors of predictions for second generation air sensors over a 50-1000 μ m range.....	125
Table 25: Percent errors for third generation air sensors over a 20-1000 μ m range.	128
Table 26: Mean R ² value between measured and predicted air sensor frequency-displacement curves.	128
Table 27: Adjusted sensitivities of first-generation solid sensors. Units are in MHz/N.....	188
Table 28: Adjusted sensitivities of second-generation solid sensors. Units are in MHz/N.....	189
Table 29: Adjusted sensitivities of third generation solid sensors. Numbers after G3 indicate parylene layer thickness. Units are in MHz/N.	189

LIST OF FIGURES

Figure 1: The spine acts as the main supporting structure of the human musculoskeletal system, facilitating load distribution and movement [1].....	1
Figure 2: The disc is composed of the nucleus pulposus, the annulus fibrosus, and cartilaginous end plates [5].....	2
Figure 3: Snidjers et al’s computational model describes cervical mechanics. Significant assumptions were made to predict loading behavior, including treating the C3-C7 vertebrae as a single fused unit [8].....	5
Figure 4: Stress-strain behavior varies greatly over the course of degeneration [17].	8
Figure 5: A cervical interbody spacer (left) is typically used in conjunction with an anterior cervical plate (right) and screw system after discectomy to facilitate arthrodesis [29], [30].	10
Figure 6: Smart spine fusion rods are highly modified to incorporate force sensing capabilities [40].....	13
Figure 7: Rohlmann <i>et al</i> ’s smart anterior vertebral replacement was used to measure <i>in vivo</i> forces in the lumbar spine [42].....	14
Figure 8: Ledet <i>et al</i> ’s smart interbody spacer implant was used to measure <i>in vivo</i> forces in the lumbar intervertebral disc space [44].	15
Figure 9: A load cell is housed in a custom PEEK interbody spacer tailored to a goat’s C3-C4 disc space.	16
Figure 10: Coils can be represented as a serial RLC circuit.	18
Figure 11: Sensor deformation caused by an applied load changes its electrical behavior, causing the measured resonant peak to shift. The chart’s X axis is resonant frequency, and the Y axis is return loss magnitude.....	18
Figure 12: The quality factor, or the bandwidth and magnitude of the signal, dictates ease of sensor measurement. A small bandwidth with high return loss gives a more accurate measure of a sensor’s resonance. Note return-loss is negative.	20
Figure 13: Microfabricated resonant sensors developed in our lab were used to measure intracompartmental pressures.	21
Figure 14: Microfabricated resonant sensors developed by Dion <i>et al</i> were used to measure forces in a modified TKA patellar implant [56].....	22

Figure 15: A depicted cross-section of a passive resonant sensor shows the relevant coil and sensor geometries used in frequency calculations. The large yellow component is the substrate supporting the coil. The smaller orange components are the coil traces themselves. 26

Figure 16: Drazan *et al*'s lumped constant circuit model describes the physics of the anti-aligned, parallel, disconnected passive resonant sensors. The dots above the inductors indicate mutual inductance between coils in parallel. The dotted line indicates mutual capacitance between coils in parallel..... 27

Figure 17: Intra-trace “parallel plate” capacitance contributes to unchanging parasitic capacitances that reduce sensitivity. The orange columns represent copper traces, and the gray component represents the substrate. The arrows indicate capacitive behavior. 33

Figure 18: This is a typical stack of materials used in our sensors. The parylene layer is considered above the trace layer, and the alumina and PCB layers are considered below the trace layer..... 35

Figure 19: The “full map” of adjacent dielectric materials allows for a more accurate model of parasitic capacitance. The air gap layer accounts for voids present in the intervening layer. 36

Figure 20: Cervical vertebral morphometry is key to smart implant design. Relevant parameters are upper endplate width (EPWu), lower endplate width (EPWl), upper endplate depth (EPDu), and lower endplate depth (EPDl) [67]..... 45

Figure 21: Example of a handmade sensor comprised of two epoxy-set, handwound coils separated by PDMS..... 50

Figure 22: Example of a microfabricated force sensor comprised of two Borofloat coils with etched copper traces, separated by parylene C polymer. 51

Figure 23: Four first-generation coils were designed and laid out in EAGLE to fit within custom cervical interbody implants. Center and corner drill-holes were included as alignment features. 56

Figure 24: Six second-generation coils designs were selected and laid out in EAGLE. A second corner drill-hole was added for more consistent alignment in air testing and solid sensor fabrication. 59

Figure 25: Design G2D15 was laid out in EAGLE as the candidate for a third generation run of coils. This design was selected for fabrication of a set of sensors with varying intervening layer thicknesses as part of model validation. 60

Figure 26: Parylene C dimer is pyrolyzed into its monomer form, then it as it cools down, it polymerizes into a uniform, conformal layer on a downstream surface..... 68

Figure 27: First generation coil designs are designated as G1D2, G1D3, G1D7, G1D8 from left to right ascending.....	73
Figure 28: Going from top left to right, then bottom left to right, second-generation coils are designated as G2D3, G2D9, G2D16, G2D1, G2D7 G2D15.	74
Figure 29: Third-generation coils are a singular design.	75
Figure 30: Image 30A shows a first-generation coil with incomplete etching on the trace base. Image 30B shows a third-generation coil with more complete etches. Both images were taken using an optical microscope.....	76
Figure 31: Traces with orthogonal walls provide more predictable electrical behavior than traces with incomplete etch profiles.	77
Figure 32: Untreated substrates coated with parylene C easily delaminates when a sharp edge is inserted between the substrate and parylene C. The lighter colors near the corners indicate delaminated parylene C.....	78
Figure 33: Coated coils had noticeably lighter coloration, and the copper traces lost their luster. Thicker layers were more opaque and lighter in coloration.	79
Figure 34: These coils were all done in the same parylene deposition run, yet they clearly exhibit different parylene layer thicknesses. Uneven depositions were apparent within coils.....	80
Figure 35: Profilometry scans of a coated coil showed uneven Parylene C deposition. Note the decrease in average trace height as well as general drop off towards the right side of the coil diameter.....	80
Figure 36: The red arrows in 36A indicate encroaching parylene on the chamber seal itself. The red arrow in 36B indicates the solid polymer buildup along the chamber wall.	81
Figure 37: Coils were placed roughly at the same radius from the center of the platform for consistent deposition for each batch.	82
Figure 38: Camera-assisted alignment was used in the die bonder for accurate alignment of coils. The screen shows a coil close to alignment, as indicated by the red arrows. A perfect overlap would show no overlap in alignment holes.....	83
Figure 39: This axial and transverse view of a completed PCB sensor shows successful bonding.	84
Figure 40: FR4 blanks were coated alongside coils. Films were partially cut, and a profilometer measured parylene C thickness by measuring the height difference between the parylene C and the underlying substrate.	85

Figure 41: A stack of sensors was cast in resin and bisected for SEM imaging and variable thickness model validation. The red arrows indicate each of the eight sacrificed, bisected sensors in this resin cast. The red bracket indicates the inner diameter of the coils secured by a metal post. 86

Figure 42: Bisected solid sensors were SEM imaged to assess intervening layer thickness and deposition quality. This SEM image shows a bisected parylene C force sensor’s overlapping traces. 87

Figure 43: Another SEM image of a bisected solid sensor’s traces shows the non-uniform profile of the annealed parylene C layers as indicated by the red line. Trace aspect ratio reduces deposition uniformity. Uneven trace etches are also exemplified in this image. 89

Figure 44: The thick parylene sample in image 44A has large defects compared to the thin parylene sample in image 44B. Both were taken at the same magnification. 91

Figure 45: This SEM image shows a “boulder” defect on the surface of the thick parylene sample. 91

Figure 46: The arrow indicates an example of voids, or “air gaps”, that formed during sensor bonding due to copper trace aspect ratio and layer non-uniformities. 92

Figure 47: The pictured coil’s original copper trace width and space underneath the parylene are each ~75 μm 93

Figure 48: Arrangement of antenna and NA for coil resonance characterization. 98

Figure 49: The machined AlSi fixture allows for continuous monitoring of coils and sensors during testing. 100

Figure 50: Figure 50A shows drilled alignment holes for posts to rest in. Figure 50B shows an example of aligned coils for air testing. Superior fixture not shown for clarity. 101

Figure 51: An MTS 2/G configured for sensor compression testing has custom fixtures, an antenna, and a network analyzer for sensor measurement. 102

Figure 52: An MTS extensometer was attached to the fixtures via knife-blades and secured with rubber bands for improved displacement readings. 103

Figure 53: A pair of coils are aligned and secured to the superior and inferior fixtures for air gap displacement testing. 105

Figure 54: Solid sensors are centered on the inferior fixture, then the superior fixture is brought into contact with the sensor for compression testing. 107

Figure 55: Concentric circles approximation can break down in coils with less turns. 117

Figure 56: Four first generation air sensors were tested mechanically with an air gap to determine the displacement-frequency relationship. Error bars show one standard deviation based on three measurements..... 119

Figure 57: Six second generation air sensors were tested mechanically to determine their mean frequency-displacement behavior. Error bars show one standard deviation based on three measurements..... 120

Figure 58: Third generation air sensors were mechanically tested to determine their mean frequency-displacement behavior. A plot showing the resonant frequency vs. displacement behavior of third generation air coils as tested on an MTS. Error bars show one standard deviation based on three measurements..... 121

Figure 59: Third generation air sensors were mechanically tested over a small displacement range of 20 to 90 μm to determine mean frequency-displacement behavior. Error bars show one standard deviation based on three measurements. 122

Figure 60: Measured and predicted frequency-displacement behavior for the G1D2 design is compared. Error bars show one standard deviation based on three measurements. 123

Figure 61: Measured and predicted frequency-displacement behavior of the G2D15 design is compared Error bars show one standard deviation based on three measurements. 124

Figure 62: Measured and predicted frequency-displacement behavior of the G3D15 design is compared Error bars show one standard deviation based on three measurements. 126

Figure 63: Measured and predicted frequency-displacement behavior of the G3D15 design is compared over a smaller 20-90 μm range. Error bars show one standard deviation based on three measurements..... 127

Figure 64: Effects of underloading versus overloading an air sensor in preload. The gray components indicate the fixture, and the brown components indicate the coils..... 130

Figure 65: Extensometer-controlled displacement reduces the variance between measurements in air sensors. Error bars show one standard deviation based on three measurements..... 131

Figure 66: Mean measured versus predicted frequency-load behavior of a solid G1D2 sensor is compared. Error bars show one standard deviation based on three measurements. 132

Figure 67: Mean measured versus predicted frequency-load behavior of a solid G2D1 sensor is compared. Error bars show one standard deviation based on three measurements. 134

Figure 68: Mean measured versus predicted frequency-load behavior of a solid G3D15 sensor is compared. Error bars show one standard deviation based on three measurements. 135

Figure 69: The measured slope (MHz/N) of each solid sensor ranged from -0.25 MHz/N to a little over -3 MHz/N.....	136
Figure 70: The predicted slope (MHz/N) of each solid sensor ranged from -0.05 MHz/N to a little over -0.4 MHz/N, with a lone outlier at -1.8 MHz/N.....	137
Figure 71: All eleven parylene C G3D15 sensors are measured and plotted to build a frequency-parylene C thickness curve.	139
Figure 72: G1D2 air sensor. Error bars show one standard deviation based on three measurements.....	171
Figure 73: G1D3 air sensor. Error bars show one standard deviation based on three measurements.....	172
Figure 74: G1D7 air sensor. Error bars show one standard deviation based on three measurements.....	172
Figure 75: G1D8 air sensor. Error bars show one standard deviation based on three measurements.....	173
Figure 76: G2D1 air sensor. Error bars show one standard deviation based on three measurements.....	174
Figure 77: G2D3 air sensor. Error bars show one standard deviation based on three measurements.....	174
Figure 78: G2D7 air sensor. Error bars show one standard deviation based on three measurements.....	175
Figure 79: G2D9 air sensor. Error bars show one standard deviation based on three measurements.....	175
Figure 80: G2D15 air sensor. Error bars show one standard deviation based on three measurements.....	176
Figure 81: G2D16 air sensor. Error bars show one standard deviation based on three measurements.....	176
Figure 82: G3D15 air sensor. Error bars show one standard deviation based on three measurements.....	177
Figure 83: G1D2P34 solid sensor. Error bars show one standard deviation based on three measurements.....	178

Figure 84: G1D2P910 solid sensor. Error bars show one standard deviation based on three measurements.....	179
Figure 85: G1D2P1112 solid sensor. Error bars show one standard deviation based on three measurements.....	179
Figure 86: G1D7 solid sensor. Error bars show one standard deviation based on three measurements.....	180
Figure 87: G1D8 solid sensor. Error bars show one standard deviation based on three measurements.....	180
Figure 88: G2D1 solid sensor. Error bars show one standard deviation based on three measurements.....	181
Figure 89: G2D9 solid sensor. Error bars show one standard deviation based on three measurements.....	182
Figure 90: G2D15 – 150 μm solid sensor. Error bars show one standard deviation based on three measurements.....	182
Figure 91: G2D15 – 100 μm solid sensor. Error bars show one standard deviation based on three measurements.....	183
Figure 92: G2D15 – 74 μm solid sensor. Error bars show one standard deviation based on three measurements.....	183
Figure 93: G2D16 solid sensor. Error bars show one standard deviation based on three measurements.....	184
Figure 94: G3D15 – 50 μm solid sensor. Error bars show one standard deviation based on three measurements.....	185
Figure 95: G3D15 – 74 μm solid sensor. Error bars show one standard deviation based on three measurements.....	186
Figure 96: G3D15 – 98 μm solid sensor. Error bars show one standard deviation based on three measurements.....	186
Figure 97: G3D15 – 150 μm solid sensor. Error bars show one standard deviation based on three measurements.....	187
Figure 98: G3D15 – 167 μm solid sensor. Error bars show one standard deviation based on three measurements.....	187

Figure 99: G3D15 – 169 μm solid sensor. Error bars show one standard deviation based on three measurements..... 188

ACKNOWLEDGEMENT

My incredible journey as a graduate student at RPI is unfortunately coming to an end. I have learned so much in my time here, and I have met many amazing people. I would first like to thank my advisor, Dr. Eric Ledet, for his wisdom and eternal patience. Thank you for being an excellent role model in and out of research. Your mentorship and optimism will stick with me for the rest of my life, and I will fondly remember skiing with you and laughing at ugly Christmas sweaters at your holiday parties. I credit my growth as a person to your influence. Once again, thank you for letting me be a part of your lab, and thank you for everything.

I would like to thank my committee members, Dr. Deanna Thompson and Dr. Deva Chan, for being a part of my education and growth as a graduate student. Thank you for your patience and invaluable feedback on my research.

I would like to thank the Biomedical Engineering department and the Center for Disability Services for allowing me to continue my research as a graduate student. I gained invaluable experiences through my teaching assistantship and CFDS fellowship that cannot be found in a lab.

I would like to thank everybody in the Innovative Medical Devices Laboratory (formerly the Musculoskeletal Mechanics Lab!). Dr. Matthew Dion, Dr. Josh Peterson, and Dr. John Drazan, you all were excellent role models as graduate students, and you were patient with my endless inquiries into your work and lives as graduate students. I would like to thank Dr. Drazan especially for his guidance and sage advice as I navigated my first year and first steps into my research.

I would like to thank my senior graduate student, Liz Capogna, for her ability to answer any question that I had regarding Troy, RPI, and research. I still crack up whenever I think about that day we spent coming up with names for the rabbits. I would like to thank my junior graduate students, Ben Liddle, Rebecca Levy, and Madelyn Stout, for your help and feedback on my

research. I'd like to thank Ben especially for his invaluable insight into sensor physics. Also, Benjamin, you're more than welcome to use my desk as a standing desk. I would also like to thank my undergraduate researchers, Kate Batzinger and Khaled Abdoun, who assisted me in my research. I know all of you guys will absolutely be successful in your lives.

I would like to thank cMDIS for their key support in my research. I spent a lot of time in the clean room, so thank you to all of the staff who trained me and assisted me with the equipment. I owe a massive thank you to Bryant Colwill for his patience and understanding as I worked to wrap up my research. You provided invaluable insight into my struggles with my sensor fabrication, and I would not have been able to make my research as successful as it was without your assistance.

I would like to thank my family for their eternal support in all my endeavors. You guys will always be there for me, even if I wanted to be a scruffy barista in Portland, Oregon. Mom and Dad, you have provided so much for me, and I am blessed to be your son. Hilary and Heidi, you guys are the best sisters ever, and I always appreciate sharing silly memes with you and our conversations on the phone. Your support has been instrumental to my perseverance through this work.

Finally, I want to thank my girlfriend, Erin, for her infinite patience and love as I struggled through the ups and downs of my time in graduate school. You never fail to make me smile, and your ability to put up with my bad puns and poor comedic timing is something I cherish. Thank you again for your love and support.

ABSTRACT

Smart orthopedic implants are invaluable tools for elucidating physiologically relevant data *in vivo*. These data can be used to validate biomechanical models and to improve implant designs. Smart spinal fusion implants could provide insight into the mechanisms of degenerative disc disease (DDD), as well as the role of biomechanics in the fusion healing process.

Due to the size constraints and complexity of the lower cervical spine, nobody has successfully measured the forces passing through the interbody disc space in the cervical spine *in vivo*. Wireless, passive resonant force sensors may provide an alternative to conventional sensor technology such as strain gages used to measure loads. Wireless, passive resonant force sensors are low cost, have a small footprint, are durable, and are simple, making them an attractive alternative for instrumenting a smart cervical interbody implant.

Our wireless, passive resonant force sensors are composed of two mirrored, parallel, Archimedean spiral coils separated by a solid insulating dielectric material that deforms in response to an applied load. An axial load causes a deformation in the intervening dielectric layer, changing the mutual capacitive and inductive interactions between the coils. This change in electrical behavior results in a measurable change in resonant frequency which correlates to the applied load.

In this research, a predictive model of passive resonant force sensor behavior was developed as a tool to efficiently and rapidly design force sensors for various smart orthopedic implant applications. More specifically, this model was used to develop wireless, passive resonant force sensors for use in a cervical interbody implant.

Low cost, rapid prototyping of force sensors was enabled through use of printed circuit board (PCB)-based coils. PCB coils are simple and quick to batch produce and were used to

fabricate a wide array of sensor geometries to test against the model for validation. Parylene C was used as an intervening layer due to its material properties and unique, conformal deposition process. These combined manufacturing techniques allowed us to produce high-quality force sensors that were able to accurately measure physiologically relevant loading conditions.

Results showed that the model accurately predicted the resonant frequency of coils and air sensors over a wide range of geometries and configurations. The analytical model was further validated through measurement of solid force sensor behavior under compression. The model accurately predicted the resonant frequencies of fabricated force sensors, and the sensors exhibited high sensitivity to applied loads while remaining within predefined, physiologically relevant design constraints.

We built a model that can be used by researchers and engineers to design and build passive resonant force sensors for smart orthopedic implants. We developed techniques for rapid and inexpensive fabrication of passive resonant sensors. We also successfully demonstrated real-time, wireless force sensing with rapidly prototyped, PCB-based, resonant force sensors designed via the model. This predictive model will be a useful tool for medical researchers and engineers to determine whether their smart orthopedic implants utilizing these novel wireless, passive, resonant force sensors will function as needed.

1. INTRODUCTION

1.1 Spine Anatomy

1.1.1 Bony Anatomy

The primary purpose of the spine is to facilitate force distribution and movement throughout the musculoskeletal system. It also protects the spinal cord. The spine consists of five distinct regions: the cervical region, the thoracic region, the lumbar region, the sacrum, and the coccyx as shown in Figure 1. There are seven cervical vertebrae, twelve thoracic vertebrae, and five lumbar vertebrae. The cervical and lumbar regions exhibit a lordotic curve, while the thoracic region exhibits a kyphotic curve. These curves allow for additional flexibility and shock absorption in the spine [1]-[3].

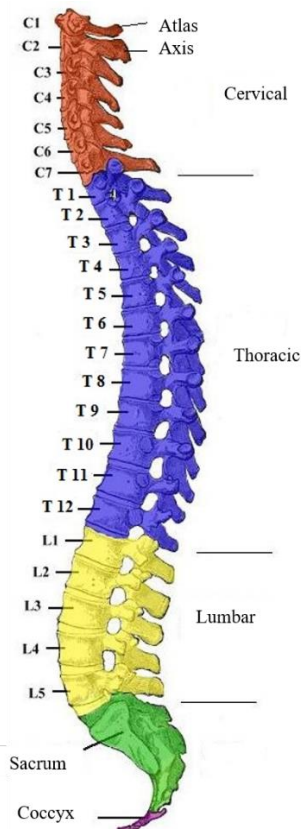


Figure 1: The spine acts as the main supporting structure of the human musculoskeletal system, facilitating load distribution and movement [1].

A vertebra is comprised of the vertebral body anteriorly and the neural arch and posterior elements posteriorly. The vertebral body is the primary load bearing component of the vertebra, and between adjacent vertebral bodies are the intervertebral discs. The neural arch is composed of the pedicles, lamina, facets, articular processes, transverse processes, and spinous processes. The arch connects to the vertebral body via the pedicles, forming a foramen that surrounds and protects the spinal cord. The facet, or zygapophyseal joints, allow for posterior articulation of adjacent vertebrae and help regulate motion of the spine. The transverse and spinous processes provide attachment points for ligaments and musculature [2], [3]. The basic shape and function of vertebrae is the same throughout C3 to L5, but there are differences in proportions between each region.

1.1.2 Disc Anatomy

The intervertebral disc is an avascular, fibrocartilaginous structure that is composed of the nucleus pulposus, the annulus fibrosus, and the cartilaginous endplates. This structure provides the primary means for motion of the spine, and it also serves as the main distributor of compressive load throughout the spine [4].

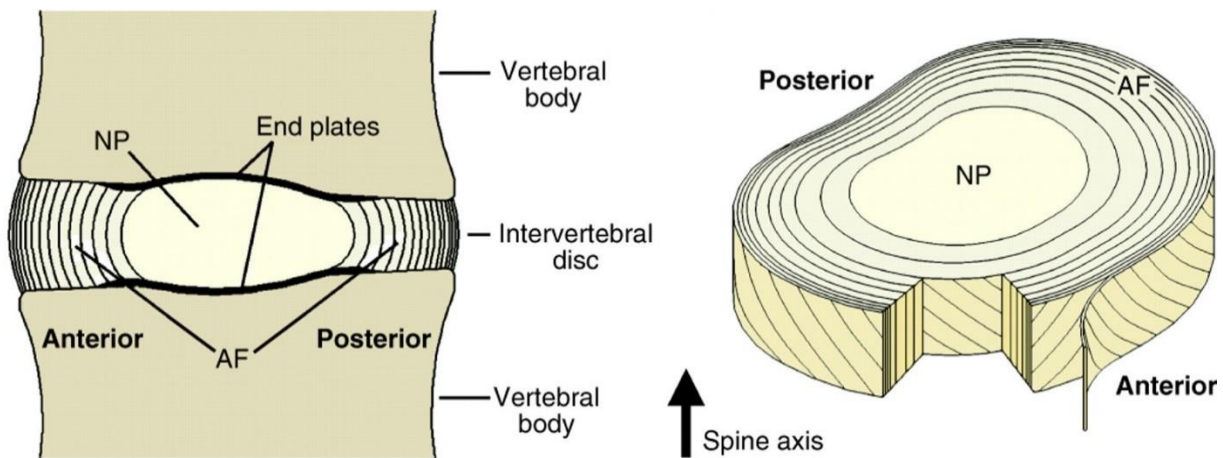


Figure 2: The disc is composed of the nucleus pulposus, the annulus fibrosus, and cartilaginous end plates [5].

The nucleus pulposus is a gel-like structure centered in the disc. It is composed of proteoglycans, collagens, and water, which gives it hydrostatic properties. These properties allow the nucleus pulposus to serve as the main load bearing component in the disc and act as a shock absorber. The annulus fibrosus consists of concentric rings of collagen I fibers. These fibers follow an approximate 25 to 45 degree inclination from the transverse plane with adjacent rings having opposing fiber directions. The resultant structure allows for resistance to shear stresses as well as resistance from internal pressure exerted by the nucleus pulposus. The cartilaginous endplate is a hyaline cartilage structure that bridges the nucleus and annulus to the bony endplate. It sits superior and inferiorly of the disc, and it constrains the nucleus pulposus [2], [6].

Each vertebra is connected by discs to comprise a flexible, load bearing structure. The vertebrae and discs work in conjunction with supporting connective tissue and muscle to facilitate movement in the spine.

1.1.3 Spine Biomechanics

The functional spine unit (FSU) is the smallest section of the spine that can represent entire spine biomechanical behavior. It consists of two adjacent vertebrae separated by an intervertebral disc, forming a three joint complex that is supported by longitudinal ligaments, process ligaments, and the ligamenta flava (joining the laminae).

Each FSU has six degrees of freedom, allowing for flexion, extension, lateral bending, and rotation. Bony features like the facets limit and facilitate movement in various directions, depending on the region of the spine. Cervical vertebrae have sloped articulating surfaces, both on their facets and endplates, to facilitate a primary flexion-extension motion pattern. Thoracic facet joints limit motion along the sagittal plane while facilitating rotation and lateral bending. The ribs, spanning from vertebrocostal joints to the sternum, provides stability and limited movement for

the thoracic region. Lumbar facet and endplate angles facilitate flexion-extension motion patterns while limiting lateral bending and greatly limiting rotation. Ligaments also regulate motion by restricting movement within physiological limits and dissipating energy during rapid movements [2].

The intervertebral disc undergoes compression and tension during normal bending motion patterns. The disc also experiences shear stresses during rotation and eccentric bending. The disc can also withstand high loads, though supporting elements like the endplates and facets tend to fail well before the disc itself does [7]. There is a substantial body of research that describes these loading patterns, as this information is critical for understanding how the spine responds to everyday activities.

1.1.4 Biomechanical Spine Models

Biomechanical modeling of the spine involves use of imaging, graphical models and finite element analyses to determine biomechanical parameters such as pattern of motion, axes of rotation, loads, and moments. Inputs are informed by measured movements and forces. For example, one such model examines the kinematic behavior of the cervical spine using a six degrees of freedom, 8-link computational model, as shown in Figure 3.

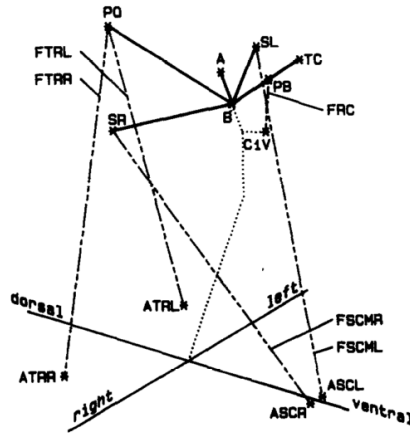


Figure 3: Snidjers et al's computational model describes cervical mechanics. Significant assumptions were made to predict loading behavior, including treating the C3-C7 vertebrae as a single fused unit [8].

This model is informed by axes of rotation, head and vertebrae positions, ligament attachment, and primary musculature attachment. Inputting external loads and accelerations returned resultant vertebrae positions as well as joint reaction forces at the atlanto-occipital joint [8]. Current biomechanical modeling techniques involve input assisted optimization, where outputs describing a range of motion and forces are created through real-world inputs. Electromyography and patient specific muscle morphometry inform these models [9], [10]. FEA in particular is becoming more popular as computational capabilities increase [11].

In addition to mathematical and computational modeling of the spine, cadaveric modeling of the spine includes *in vitro* testing of both animal and human models to determine spine kinematics and loading. Typically, a load or displacement is applied to the cadaver model to determine characteristic spinal behavior. Many *in vitro* studies have looked at cervical kinematics by applying pure moments to cadaveric spines [12]. Vertebral rotations and displacements are measured, though other relevant biomechanical information is often limited.

More accurate simulation of cervical spine biomechanics can be achieved by adding complex applied loads. For example, the primary flexion-extension motion pattern in the cervical spine can be simulated using a simulated compressive force, known as a follower load, directed through C1-C7's instantaneous axes of rotations [13]. This method provides data similar to *in vivo* flexion-extension load-displacement behavior and flexibility. Other attempts to replicate soft tissue stability and function include work in simulating segmental motion patterns by implementing variable bending moments at each vertebra. The reported kinematics are shown to be closer to *in vivo* kinematics than cadaveric models with simple loads or moments [14].

These various biomechanical models highlight the complexity of modeling the spine. A myriad of factors plays a role in spinal movement and forces. These computational and cadaveric models are limited by assumptions and simplifications in modeling supporting soft tissue. Variations in morphologies, experimental setup, and supporting physiological inputs lead to high variability and conflicting reported numbers. The best models try and emulate *in vivo* conditions as accurately as possible, though these methods are limited compared to actual, *in vivo* measurement.

In vivo kinematic measurements of applied and resultant forces, motion patterns, and other parameters serve as reference for cadaveric and computational models. However, no examples exist in literature of direct, *in vivo* cervical loading and force measurement. Additionally, pathologies associated with cervical loading are not as well understood due to the lack of reliable information. Accurate modeling and measurement of spine biomechanics can drive improved understanding and treatment of pathologies such as neck and back pain.

1.2 Disc Degeneration

1.2.1 Etiology

Degenerative disc disease (DDD) is a condition that reflects degenerative changes in the intervertebral disc over time. These changes include loss of proteoglycans and subsequent water content, gradual changes in annulus composition and structure, and most importantly, loss of height. Known contributors to degenerative disc disease include aging, genetic factors, nutrition, metabolic disorders, low-grade infections, neurogenic inflammation, autoimmune response, and mechanical factors¹⁵. Mechanical factors are a common cause of cervical spondylosis.

Mechanically driven disc degeneration is caused by repeated vibration, eccentric movements such as combined torsion and flexion, and excessive compression [15], [16]. Cadaveric intervertebral discs subjected to cyclic, compressive loading leads to mechanical disruptions in the form of annulus tearing, delamination, endplate defects, and reduced disc height. Herniation also occasionally occurs due to the repeated stressing of these spines [16]. Spinal loading over a lifetime naturally leads to mechanically related disc degeneration.

1.2.2 Biomechanics

Degeneration results in loss of disc height and abnormal load transmission through the FSU. Changes in biomechanics lead to changes in stress-strain behavior and the instantaneous axes of rotation of each FSU, as shown in Figure 4.

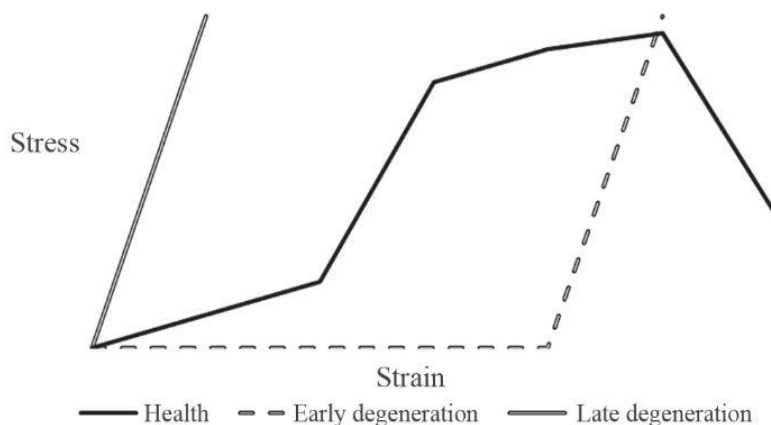


Figure 4: Stress-strain behavior varies greatly over the course of degeneration [17].

These changes in mechanical behavior exacerbate further degeneration. Degenerated discs experience atypical stresses, damaging the annulus and endplates and producing osteophytes that result in further abnormal loading and motion [16], [17]. Changes to the annulus can also cause nucleus to expand and extrude, resulting in an instantaneous axis of rotation shift. Range of motion can increase in early stages, but it decreases later at stages of degeneration. Late degeneration shows a fibrotic nucleus pulposus, resulting in stiff, linearly elastic behavior [17]. These biomechanical changes in the cervical spine can ultimately lead to neck pain.

1.2.3 Pathology

Degenerated discs can cause specific and non-specific, chronic neck pain in a few ways. Cervical radiculopathy, or nerve root compression, occurs with the narrowing of nerve root foramen. The loss of disc height also contributes by further placing pressure on nerve roots exiting the vertebra [18].

Cervical myelopathy occurs when osteophytes grow from the posterior disc into the spinal canal. The altered mechanics of the degenerated disc induce these bone growths. The resultant loss

of space in the canal results in a higher likelihood of impingement during motion. Impingement may also occur with a herniated disc, compressing the spinal cord and causing significant pain. The ligamentum flavum can lose elasticity over time and impinge on the spinal cord itself [19]. Additionally, severely degenerated discs can be infiltrated by sinuvertebral nerve growth, and any newly innervated discs can evoke a pain response when strained [20]. If disc degeneration and the resultant neck pain gets bad enough, many patients opt for treatment.

1.2.4 Prevalence of Neck Pain

Neck and back pain is the number one cause of disability in the world. More specifically, neck pain can be a significant limiting factor in day to day activities [21]. The overall prevalence of neck pain in the general population is 23.1% [22]. More than 11.5% of adults worldwide have activity-limiting neck pain over a 12-month period [23]. There is still a limited understanding of neck pain etiology compared to lower back pain, but there are ongoing efforts to understand the scope of the problem [24]. Neck pain is primarily attributed to traumatic injury and disc degeneration, or cervical spondylosis, of which the latter is caused by several factors such as aging and mechanical overloading.

1.3 Degenerative Disc Disease Management

1.3.1 Treatment Methods

Initial management of DDD and the pathologies associated with it involves conservative treatment. Conservative care involves physical therapy and pain management. When conservative care fails to address DDD pathologies and neck pain, surgical intervention is considered [25]. There are several surgical approaches to resolving cervical spondylotic related pain, including laminectomy, laminoplasty, discectomy, arthrodesis, and total arthroplasty. Each case is unique,

but generally, cervical discectomy and fusion is accepted as the safest and most effective surgical method of relieving neck pain [26]-[28].

1.3.2 Anterior Cervical Discectomy and Fusion

First developed by Bailey and Badgley in 1960, anterior cervical discectomy and fusion (ACDF) involves removal of the disc and fusion of the two adjacent vertebrae via bony growth. The anterior approach to the disc avoids the posterior vertebral elements and the spinal cord. Discectomy alleviates myelopathic pain, and a spacer in the interbody space restores disc height and any related myelopathy and radiculopathy may be reduced. The spacer can either be a bone graft, usually an autograft from the iliac crest, or an artificial interbody implant. These interbody implants can be either ramps or cages with space for bone grafts or bone growth promoters. The vertebrae and interbody spacer are typically secured with an anterior cervical plate and screws [28].



Figure 5: A cervical interbody spacer (left) is typically used in conjunction with an anterior cervical plate (right) and screw system after discectomy to facilitate arthrodesis [29], [30].

Proper design of these implants is critical to fast and effective healing. Optimal bone growth is dependent upon proper loading of the surgical site. Too little strain will limit bone growth and fail in bridging and fusing the vertebrae. Too much strain will cause the bone growth to become a fibrous “false joint” known as a pseudarthrosis [31], [32]. Both fusion outcomes result in post-operative complications.

1.3.3 Fusion Effects on Spine Biomechanics

Motion patterns in the cervical spine change drastically with plated, fused vertebrae. Interbody spaces typically experience compression during flexion and tension during extension, but the presence of a plate can reverse those loading trends [33]. Fused vertebrae also gradually lose their ROM [34]. While ACDF is effective in alleviating neck pain, the procedure can lead to a cascade of events that result in the acceleration of adjacent disc degeneration [35]. Immobilized joints result in hypermobility in adjacent FSUs, and the adjacent FSUs exhibit increased stress as a result. These mechanical factors exacerbate adjacent disc degeneration.

An improved understanding of this biomechanical behavior could provide insight into why adjacent disc degeneration is accelerated after ACDF approaches. Attempting to model this behavior is more complicated than modeling a normal, healthy human cervical spine.

Comprehensive understanding of loads transmitted through the interbody spaces in the cervical spine is paramount for optimizing fusion efficacy and recovery. Conventional biomechanical models are still limited in elucidating interbody loads and forces due to the complexity of the spine. Therefore, *in vivo* measurement of intervertebral forces remains the strongest approach for informing optimal fusion interbody implant design.

1.4 Smart Implants

Smart implants are therapeutic implants that are instrumented with sensors to measure physiological conditions inside the body. Smart implants are used to measure physiological parameters such as forces, pressures, strains, temperatures, and more. Smart orthopedic implants provide patient-specific data for personalized care. In the research setting, smart implants also provide *in vivo* data to drive next generation implant design. These data are used to develop future implant designs and improve patient outcomes [36]-[38].

1.4.1 Smart Spinal Implants

Smart instrumentation of the spine was first done in the 1960's with Waugh's work on corrective scoliosis rods with strain gage sensors [39]. Results from this work show strain gage instrumented corrective rods provided insight into attachment failure. In more recent spine biomechanics research, smart pedicle screw rods have been used to measure *in vivo* forces during daily activities during the course of spine fusion. These rods contain an extensively modified cartridge that houses six strain gauges, a telemetry transmitter, and inductive power circuit.

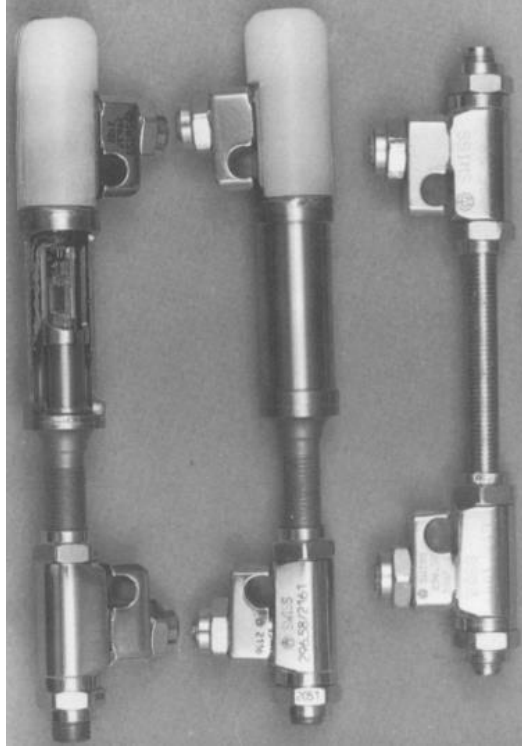


Figure 6: Smart spine fusion rods are highly modified to incorporate force sensing capabilities [40].

These rods are affixed to the posterior elements of the lumbar spine. This device measures component forces and moments, providing a three-dimensional picture of loading patterns in the lumbar region. However, the system is loaded in parallel with the spine and therefore measurements only provide insight into loads in the implant and not those in the spine. Thus, rod and screw systems provide limited insight into intervertebral disc biomechanics [40], [41].

Smart vertebral body replacements have been used to measure *in vivo* forces in the anterior lumbar spine and subsequently through intervertebral discs. However, the implant is highly modified to house six strain gauges, as well as supporting telemetry and power supplies, to measure component forces passing through the device [42], [43].



Figure 7: Rohlmann *et al*'s smart anterior vertebral replacement was used to measure *in vivo* forces in the lumbar spine [42].

This device provides rare insight into the *in vivo* biomechanics of the human lumbar spine during daily activities. However, vertebral body replacement alters the biomechanics of the lumbar spine, and so the data are not reflective of normal physiologic spinal loading.

1.4.2 Smart Interbody Implants

Smart interbody implants can provide significant advantages over other spinal smart implants in that they can measure anterior/vertebral body forces with little to no modification of posterior elements and minimal disruption to spinal musculature. However, because of the challenges associated with the small physical size of the disc space, there is limited work using this approach. In one study, a smart interbody cage device was developed that utilized sixteen, direct wired strain gauges to measure component forces in real time [44].

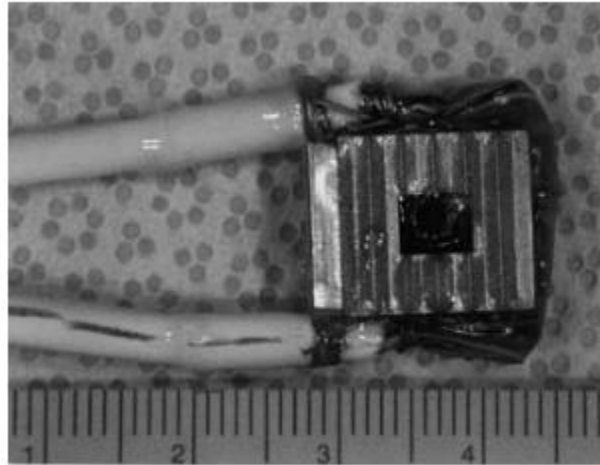


Figure 8: Ledet *et al*'s smart interbody spacer implant was used to measure *in vivo* forces in the lumbar intervertebral disc space [44].

In this study, the smart implants were used to examine loads transferred through the L4-L5 intervertebral space during daily activities in the baboon lumbar spine. This study contributes valuable information to the limited understanding of *in vivo* lumbar biomechanics.

Peterson *et al* used custom interbody implants with wired load cells. These implants were placed in the cervical spine of a goat along with various anterior cervical plate geometries. This smart implant was used to measure axial loads transmitted through the intervertebral disc space, as seen in figure 9 [33].

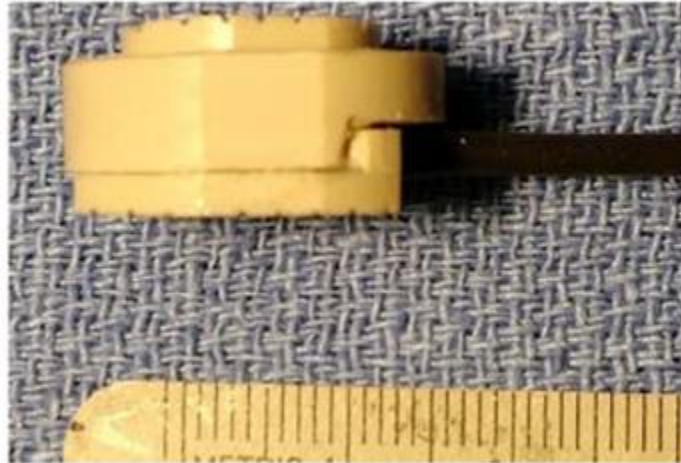


Figure 9: A load cell is housed in a custom PEEK interbody spacer tailored to a goat's C3-C4 disc space.

This study demonstrated that fusion healing progress can be correlated to measured loads. It also revealed the contributions of various anterior fusion plate geometries to load sharing through the spine, providing insight into optimal plate designs for spinal fusion. Furthermore, this study revealed that a plated spine alters cervical biomechanics. Unlike a normal, healthy disc, a plated interbody implant experiences tension in flexion and compression in extension. This study demonstrated that smart implants are useful in informing their effects on biomechanical behavior. Ideally, future interbody implant *in vivo* studies will shift away from animal models to provide an even more accurate look into spine biomechanics.

Ledet, Peterson, and Rohlmann's works are the most recent studies in direct, *in vivo* measurement of spine loading. Other groups are making efforts to develop implant technology for *in vivo* measurement of spine biomechanics, but these *in vivo* studies have not been realized yet [45].

There is a dearth of biomechanical spine data derived from direct, *in vivo* measurements. Of that, there is even less focused on the cervical spine. Instrumentation of smart cervical spinal

implants poses an even greater challenge than lumbar implants because of the cervical spine's size and increased mobility. Peterson *et al*'s work is the only example of direct, *in vivo* measurement of cervical biomechanics which is limited to an animal model. Direct *in vivo* data would be invaluable for informing theories of human cervical biomechanics. These *in vivo* data would also be beneficial to optimizing implant designs used in spinal arthrodesis, such as interbody cages and vertebral fixation plates and screws.

1.5 Passive Resonator Sensors

Historically, smart implants have been instrumented with sensors such as strain gages. These sensors, however, limit smart implant design. These sensors require supporting circuitry for power, signal conditioning, and telemetry. They require significant modification of the implants, making it harder for smart implant technology to translate to clinical applications.

Passive resonator sensors present a viable alternative to conventional sensor technology used in implant instrumentation. Passive resonant sensors measure physiological parameters without the need for an active power source by passively responding to an electromagnetic signal. Data can be transmitted wirelessly, and all complex signal processing and conditioning can be done externally in a device polling the sensors.

1.5.1 Overview of Resonant Sensor Function

Our passive resonator sensor is comprised of two anti-aligned, or mirrored, planar, parallel Archimedean spiral coils separated by a solid dielectric. With the solid dielectric between, the coils exhibit mutual inductive and capacitive behavior. Each coil can be represented by an RLC circuit, as shown in Figure 10, that resonates when exposed to an oscillating electromagnetic field [46].

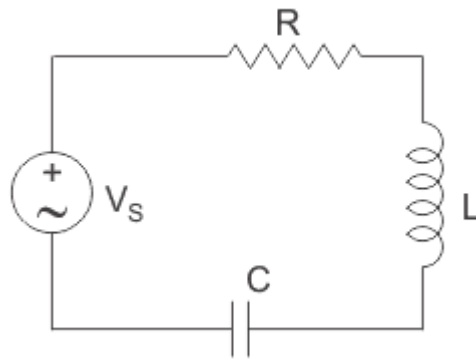


Figure 10: Coils can be represented as a serial RLC circuit.

The two adjacent coils form a more complex, physically disconnected RLC circuit that also resonates when exposed to an electromagnetic field. Importantly, when the distance between the two coils changes, the inductance and capacitance of the system changes, and the resultant resonance changes, as shown in Figure 11. This behavior can be exploited to measure various physiological conditions.

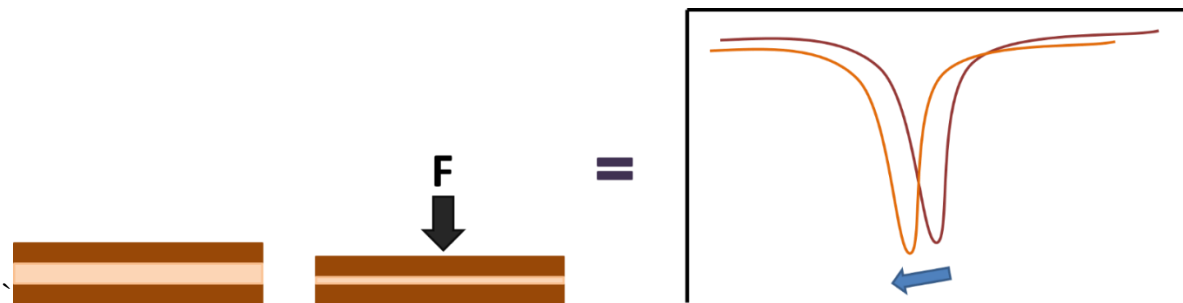


Figure 11: Sensor deformation caused by an applied load changes its electrical behavior, causing the measured resonant peak to shift. The chart's X axis is resonant frequency, and the Y axis is return loss magnitude.

1.5.2 Measuring Resonant Frequency

Typically, the frequency of resonant circuits is measured with a grid dip meter or network analyzer. Network analyzers measure the S11 parameter, which is indicative of resonant frequency

and signal quality. The S11 parameter describes a single port in the network analyzer sending and receiving the same electromagnetic signals. An antenna is connected to this port, and the system then generates an oscillating electromagnetic signal. The antenna inductively couples with the resonant circuit, and the circuit resonates at a particular frequency in response. The S11 parameter, or return-loss parameter, is the ratio between the output signal's voltage and the incident signal's voltage on the same port, normalized by some reference impedance in the system. The incident signal voltage is dependent upon how much of the outgoing signal the RLC circuit absorbs via resonance. This normalized voltage ratio is reported as the return-loss parameter [47], [48]. Q factor is another term for this measurable energy absorption that occurs in a resonant circuit. High Q indicates that coils resonate at a tight frequency band with a high magnitude return loss, while low Q indicates that coils resonate at a wide frequency band with a low magnitude return loss, as shown in Figure 12

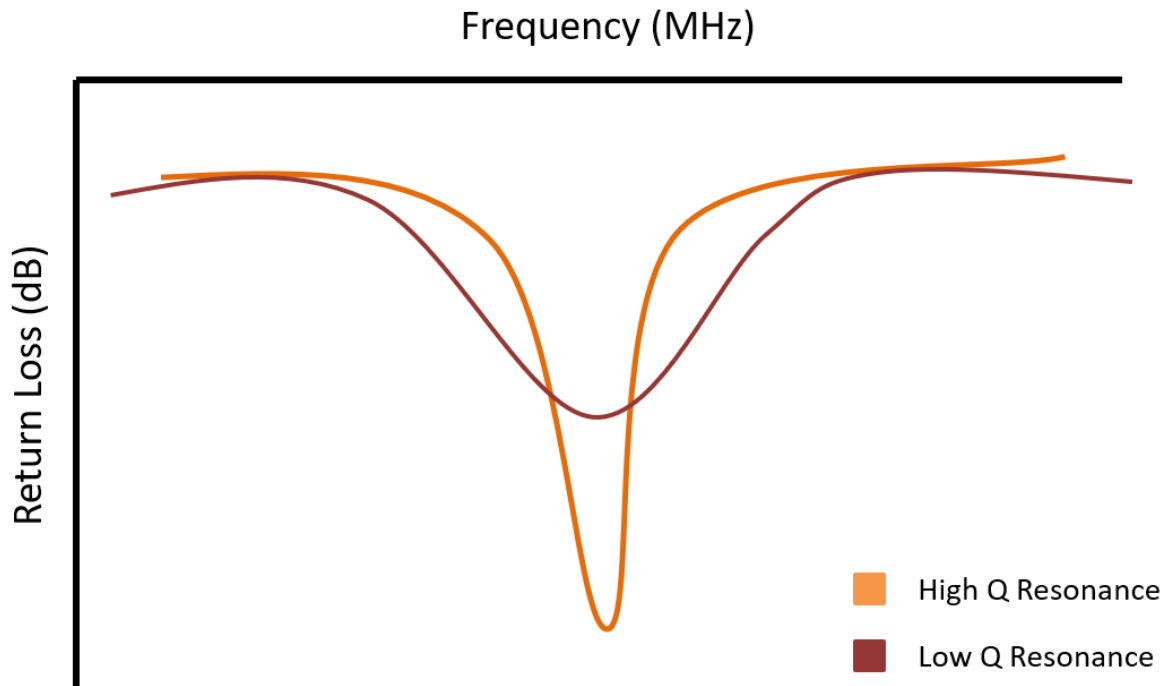


Figure 12: The quality factor, or the bandwidth and magnitude of the signal, dictates ease of sensor measurement. A small bandwidth with high return loss gives a more accurate measure of a sensor's resonance. Note return-loss is negative.

A higher Q means that the signal is easier to resolve and measure, but it may be harder to capture initially due to the smaller bandwidth [49].

1.5.3 Biomedical Applications of Passive Resonant Sensors

Passive, wireless resonant sensors first found use in biomedical applications in the 1960's. Collins *et al* introduced the novel idea of using passive resonator sensors as an intraocular pressure sensor. The simple and small device sits in the eye, enabling continuous measurement without disruption of normal eye movement [50]. Subsequent work with passive, wireless resonant sensors appears in monitoring cardiovascular pressures, running long term blood pressure measurements, and instrumenting the eye to monitor glaucoma [51]-[53].

Use of resonant sensors in orthopedic applications is a novel concept. Wachs *et al* proposed the novel concept of using wireless, passive resonant sensors for *in vivo* orthopedic applications [54]. Drazan *et al* successfully fabricated and used these wireless, passive resonant sensors to continuously monitor intracompartmental pressures for compartment syndrome [55].

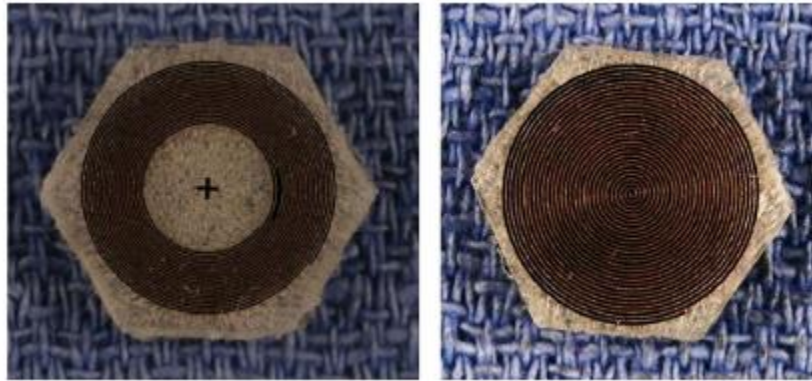


Figure 13: Microfabricated resonant sensors developed in our lab were used to measure intracompartmental pressures.

This study showed passive resonant pressure sensors are capable of continuous measurement of relevant physiological conditions. Their ability to measure physiological pressures without active power allows them to be implanted completely within the body without exposing the patient to infection risks. Dion *et al* implemented resonant sensors directly into a modified patellar implant as part of a total knee arthroplasty, as shown in Figure 14.

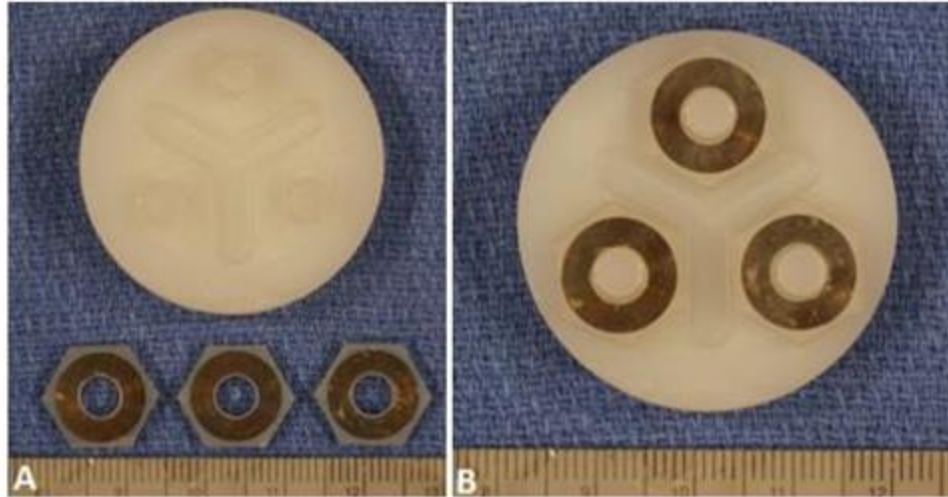


Figure 14: Microfabricated resonant sensors developed by Dion *et al* were used to measure forces in a modified TKA patellar implant [56].

Passive resonant sensors were successfully used in this study as force sensors. Sensors were housed in a commercially available implant without requiring significant modification to the implant itself. In addition to its contributions to understanding of total knee arthroplasty biomechanics, this work also laid the framework for *in vivo* study of forces in a clinical orthopedic setting using these passive resonant sensors [56].

1.5.4 Advantages Over Conventional Sensors in Instrumentation

The advantages of these passive resonant sensors over other conventional sensors includes their adaptability to many different measurands. Passive resonant coils can be batch produced inexpensively thanks to their simple design. A passive resonant sensor measures physiological data with exposure to an oscillating electromagnetic field, eliminating the need for complex circuit conditioning, telemetry, and power supply. This in turn reduces the footprint of the sensor, allowing it to be used in smaller spaces. The lack of percutaneous leads also increases the passive

resonant sensors' reliability, and it greatly reduces risk of infection for *in vivo* applications [36], [37], [57].

While smart implants have been used as tools to better understand spine biomechanics for decades, there are still many unanswered questions. A small, simple force sensor integrated into a spinal implant may provide the means to enhance our understanding of cervical spine biomechanics. However, to date, there have been no smart cervical implants that are suitable for clinical use. This is in part because the sensor technology underlying smart implants is too bulky and complex for this application. There is a need for a better understanding of resonant force sensors before they can be employed in smart cervical implants. Accurate modeling of resonant force sensors will allow us to rapidly develop sensor designs for a wide array of smart cervical implant configurations.

2. PROBLEM STATEMENT AND SPECIFIC AIMS

The goal of this work is to develop a model that can reliably predict the behavior of a wireless, passive resonator force sensor. A wide array of sensor designs was developed and tested for application in the cervical spine. Coils were rapidly prototyped and fabricated using printed circuit board (PCB) manufacturing techniques. Force sensors were built and tested for model validation.

Specific Aim 1: Develop a force sensor model

Develop and validate a passive resonator sensor-based force transducer model.

Specific Aim 2A: Develop improved sensor fabrication methods

Develop fabrication methods for rapid prototyping of passive resonant force sensors.

Specific Aim 2B: Develop force sensors for model validation

Design, develop, and validate functional, wireless, implantable force transducers that can measure physiologically relevant axial loads in the cervical spine context of a smart cervical cage.

3. SPECIFIC AIM 1: METHODS

3.1 Sensor Model Derivation

Sensor behavior can be broken down into its constituent inductive, capacitive, and resistive elements. Individual coils behave as resonant RLC circuits, and paired coils behave as a more complex resonant RLC circuit. Therefore, sensor behavior was first determined at the coil level. Once coil level behavior was accurately modeled, the mutual behavior between coils was then calculated. These calculations were combined to determine the resonant response of the sensors.

3.2 Frequency Behavior

The resonant frequency of the individual coils and of the assembled sensors can be represented by:

$$f_0 = \frac{1}{2\pi\sqrt{L_{total}C_{total}}} \quad (1)$$

where L_{total} and C_{total} are the sum of the lumped inductances and capacitances, respectively. These values are based on coil and sensor geometric properties, material properties, and the environment. The geometric properties primarily dictate coil and sensor resonant frequency. Figure 15 shows coil and sensor geometries considered in modeling resonant behavior.

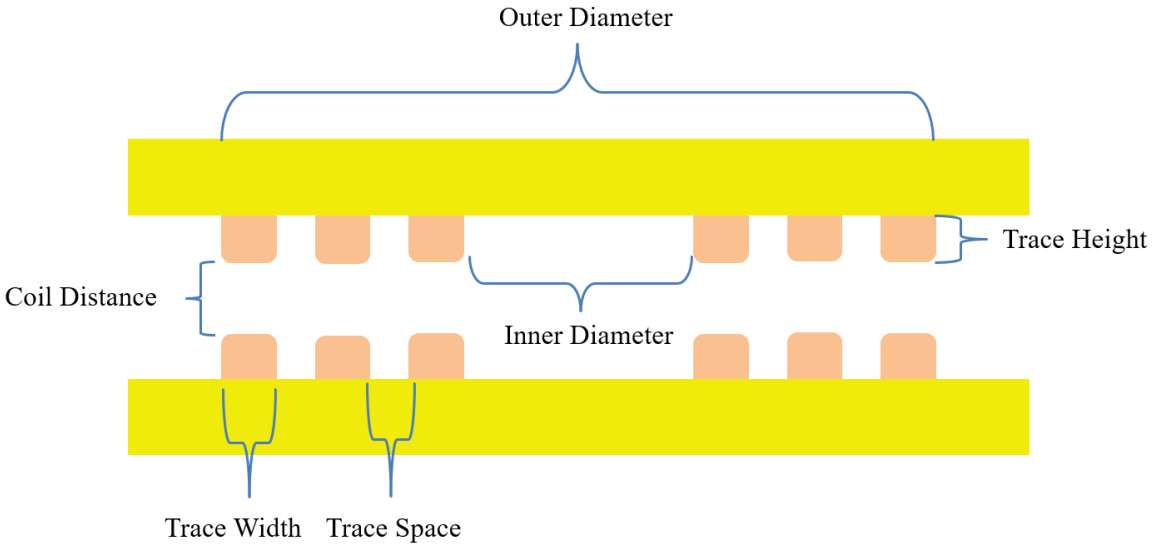


Figure 15: A depicted cross-section of a passive resonant sensor shows the relevant coil and sensor geometries used in frequency calculations. The large yellow component is the substrate supporting the coil. The smaller orange components are the coil traces themselves.

Outer diameter refers to the diameter across the outermost edges of the coil trace. Inner diameter refers to the diameter across the innermost edges of the coil trace. Trace width refers to the width of the coil trace. Trace space refers to the width of the space between coil traces. Trace height refers to the height of the coil traces above the substrate. Coil distance indicates the distance between two coils. Individual coils possess self-inductance and self-capacitance and when two coils are brought in proximity to each other, they exhibit mutual inductance and mutual capacitance. Thus, individual coils and sensors (coil pairs) each exhibit a unique characteristic resonance.

3.3 Inductive Behavior and Mathematical Derivation

A sensor's total inductance is defined as:

$$L_{total} = \frac{L_{coil\ 1}L_{coil\ 2} - M^2}{(L_{coil\ 1} + L_{coil\ 2}) - 2M} \quad (2)$$

where L_{coil} is the individual coil inductance and M is the mutual inductance between coils. This expression is derived from the summation of the equivalent circuit's coupled inductors in parallel using Kirchhoff's Voltage Law (KVL). Figure 16 shows an equivalent circuit for the paired coil sensor⁵⁸.

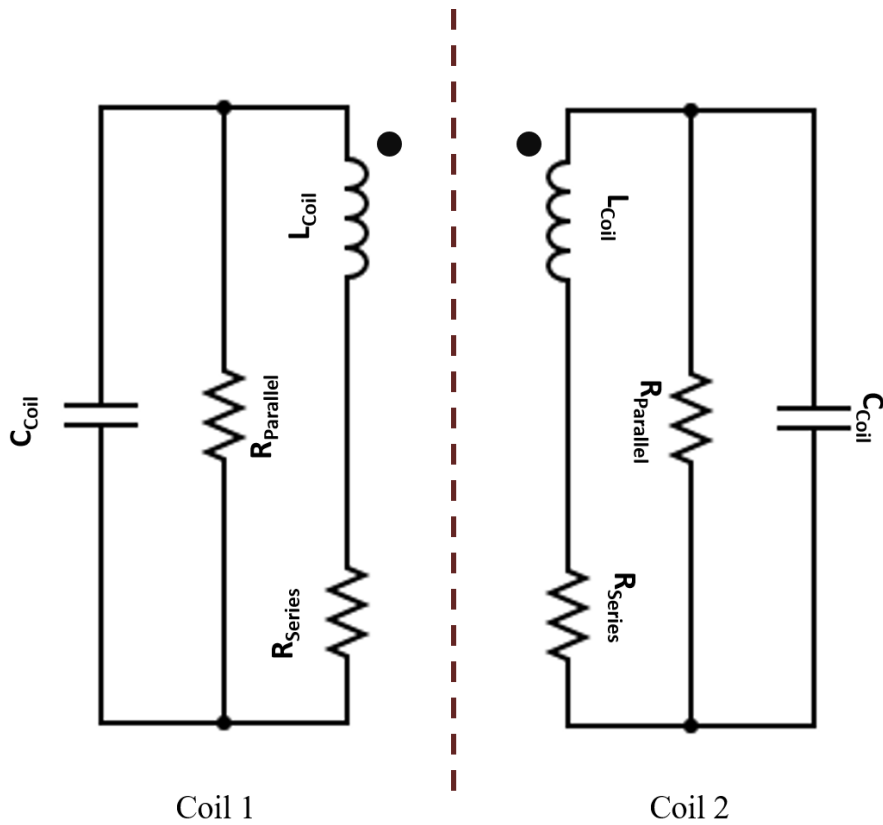


Figure 16: Drazan *et al*'s lumped constant circuit model describes the physics of the anti-aligned, parallel, disconnected passive resonant sensors. The dots above the inductors indicate mutual inductance between coils in parallel. The dotted line indicates mutual capacitance between coils in parallel.

This equivalent circuit depicts two separate RLC resonant circuits with only mutual interactions between the two. Physically disconnecting the coils creates a parallel, inductive coupling.

Mirroring the coils results in the negative mutual inductance term in the found in the denominator of Equation 2 [58], [59]. Physical disconnection of the coils also ensures that only mutual inductive and capacitive interactions are occurring, and no serial connections occur between the coils. Therefore, changes in electrical behavior are only affected by a sensor's environment or deformations of the intervening layer.

3.3.1 Coil Inductance

The individual coil inductance can be modeled using two approximation methods. The first method, proposed by Zierhofer *et al* in 1996 [60] approximates circular, planar, spiral coils as a series of concentric rings. The inductance of each ring is calculated using the following equation:

$$L(a, R) = \mu_0 a \left(\ln \left(\frac{8a}{R} \right) - 2 \right) \quad (3)$$

where a is ring radius, R is trace width divided by two, and μ_0 is permeability of free space. After finding the inductance of each ring, the mutual inductance between each interacting ring on the coil is determined using the following expression:

$$M(a, b, \rho = 0, d = 0) = \mu_0 \sqrt{ab} \left[\left(\frac{2}{\kappa} - \kappa \right) K(\kappa) - \frac{2}{\kappa} E(\kappa) \right] \quad (4)$$

where

$$\kappa \equiv \left(\frac{4ab}{(a+b)^2 + d^2} \right)^{\frac{1}{2}} \quad (5)$$

where $K(k)$ and $E(k)$ are the complete elliptic integrals of the first and second kind, respectively. ρ is the distance between each ring's center axis or alignment between two rings, a and b are the radii of interacting rings, and d is the distance between coils. ρ and d are zero as the rings are on the same plane and concentric. The individual ring inductances are then summed, as well as each possible ring-ring mutual interaction on the same coil, using the following expression

$$L_a = \sum_{i=1}^{N_a} L(a_i, R) + \sum_{i=1}^{N_a} \sum_{j=1}^{N_a} M(a_i, a_j, \rho = 0, d = 0) (1 - \delta_{i,j}) \quad (6)$$

Where N_a is the number of concentric rings in a coil, and $\delta_{i,j} = 1$ when $i = j$, and $\delta_{i,j} = 0$ otherwise (to properly index and avoid determining M between the same ring). The interaction of the intra-coil rings in relation to each other ring is described via a_i and a_j .

The second method, proposed by Mohan *et al* in 1999 [61] approximates the inductive behavior of various planar coil geometries. This model:

$$L_{coil} = \frac{\mu_0 n^2 d_{avg}}{2} \ln \left(\frac{2.46}{\rho} + 0.2\rho^2 \right) \quad (7)$$

is derived from approximating orthogonal current sheets in planar, circular spiral coils, where μ_0 is permeability of free space, n is number of turns, d_{avg} is the average diameter of the coil, and ρ is the fill ratio, which can be described as

$$\rho = \frac{(d_{out} - d_{in})}{(d_{out} + d_{in})} \quad (8)$$

where d_{out} and d_{in} are the outer and inner diameters of the coil, respectively.

Both expressions are appropriate for approximating most coil inductances, but they have limitations for different coil designs. Mohan's model is less accurate when the coil trace width to trace space ratio exceeds three. Zierhofer *et al*'s model loses accuracy as the number of turns in a spiral decrease. The concentric ring approximation does not truly represent the changing radius of an Archimedean spiral, and this discrepancy is reflected in coils with a summed trace width and space larger than 10% of the coil average diameter.

3.3.2 Mutual Inductance

Mutual inductance between two coils is determined similarly to Zierhofer's single coil inductance approximation [60]. Instead of determining intra-coil inductances, this approximation is used to determine inter-coil inductance:

$$M_{ab} = \sum_{i=1}^{N_a} \sum_{j=1}^{N_b} M(a_i, b_j, \rho, d) \quad (9)$$

Where N_a and N_b are the number of concentric rings in the mutually interacting coils, and a_i and b_j are the radii of approximated rings within their respective coils. ρ and d are the same variables as defined for single coil inductances.

Some key assumptions are made in estimating the inductance. First, the axes of the coils are assumed to be perfectly aligned for calculating mutual inductance (i.e. that ρ equals zero). Second, individual sensor coils are assumed to be equivalent, meaning $L_{coil 1} = L_{coil 2}$. The relevant geometric inputs for approximation of sensor inductance are the number of turns on a coil, the trace width, the trace spacing, the inside and outside diameters of the coil(s), and the distance between coils in a sensor.

3.4 Capacitive Behavior and Mathematical Derivation

A sensor's total capacitance can be defined by the following expression

$$C_{total} = C_{mutual} + (C_{par1} + C_{par2}) \tag{10}$$

where C_{par} is defined as the individual coil capacitance and C_{mutual} is the parallel plate capacitance between the two coils. Like coil inductance, this expression is derived from the summation of the equivalent circuit's capacitances found in figure 16.

3.4.1 Coil Capacitance

Individual coil capacitance is characterized by small capacitances within the coil and between it and its surroundings. These capacitances contribute to the whole capacitance when determining resonant behavior of coils and sensors, but they are intrinsic capacitances and do not

change with an external stimulus. This individual coil capacitance is described as parasitic capacitance [62], [63], which is defined as

$$C_{par} = \frac{(C_{pul} * l)}{n} \quad (11)$$

where C_{pul} is the coil's effective capacitance per unit length, l is the trace length, and n is the number of turns. The capacitance per unit length is defined as the sum of the capacitive intra-trace interactions plus the interactions between the traces and each dielectric layer immediately surrounding the coil, expressed as:

$$C_{pul} = \varepsilon_{r-eff} C_0 = C_0 + C_{01} + \dots + C_{0i} \quad (12)$$

Where ε_{r-eff} represents the total effect of adjacent dielectric layers on intra-coil capacitance, C_0 indicates the intra-trace capacitance in free space, and C_{0i} indicates the capacitance between the traces and adjacent dielectric layers. The third dimension of trace height creates an additional capacitive interaction where there is parallel plate capacitance occurring between traces, as shown in figure 17.

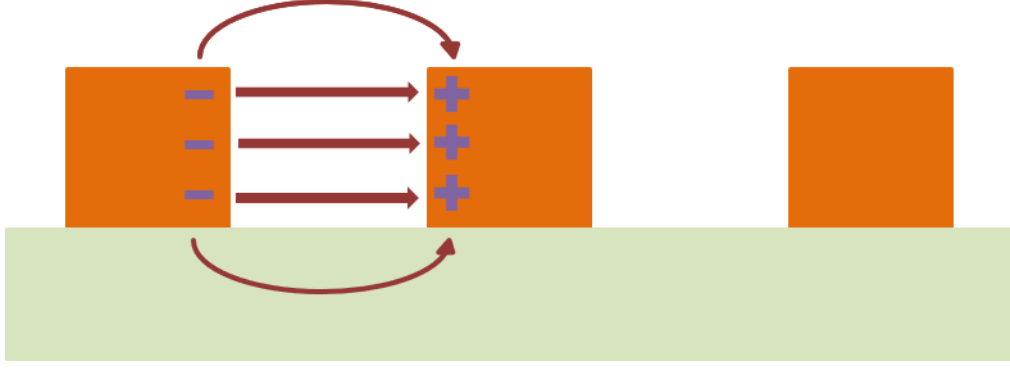


Figure 17: Intra-trace “parallel plate” capacitance contributes to unchanging parasitic capacitances that reduce sensitivity. The orange columns represent copper traces, and the gray component represents the substrate. The arrows indicate capacitive behavior.

Additionally, the trace height can increase the capacitive interactions between the traces and the surrounding dielectric layers [62]. Therefore, the effective trace height is defined as:

$$\Delta = \frac{t_0}{2\pi\epsilon_e} \left[1 + \ln \left(\frac{8\pi w}{t_0} \right) \right] \quad (13)$$

where t_0 is trace height, ϵ_e is mean permittivity of layers in contact with the traces, and w is the trace width. This term is then applied to adjust all resultant trace width and trace spaces such that

$$w = w + 2\Delta, s = s - 2\Delta \quad (14)$$

in the following capacitance approximations. After adjusting for the effects of trace height, intra-trace capacitance C_0 is determined via the expression:

$$C_0 = \varepsilon_0 \frac{K(k'_0)}{K(k_0)}, k_0 = \frac{2s}{s + 2w}, \text{ and } k'_0 = \sqrt{1 - k_0^2} \quad (15)$$

where ε_0 is permittivity of free space, $K(x)$ refers to the complete elliptic integral of the first kind, w is trace width, and s is trace spacing. The additional capacitive effect of adjacent dielectric layers can be approximated using:

$$\varepsilon_{r-eff} = 1 + \frac{1}{2} \sum_{i=1}^{n_1} (\varepsilon_{r(i)} - \varepsilon_{r(i-1)}) \frac{K(k_0)K(k'_i)}{K(k'_0)K(k_i)} + \frac{1}{2} \sum_{i=1}^{n_2} (\varepsilon_{r(i)} - \varepsilon_{r(i-1)}) \frac{K(k_0)K(k'_i)}{K(k'_0)K(k_i)}$$

$$k_i = \frac{\tanh\left(\frac{\pi s}{4t_i}\right)}{\tanh\left(\frac{\pi(s + 2w)}{4t_i}\right)}, \quad k'_i = \sqrt{1 - k_i^2} \quad (16)$$

where n_1 refers to the number of dielectric layers above the traces and n_2 refers to the number of dielectric layers below the traces, $\varepsilon_{r(i)}$ indicates the permittivity of a layer, $K(x)$ refers to the complete elliptic integral of the first kind, k_0 and k'_0 are the geometric terms for the trace layer, k_i and k'_i are the geometric terms for adjacent layers, w is trace width, s is trace spacing, and t_i is the layer thickness. ε_r is determined by subtracting the upper layer $\varepsilon_{r(i)}$ from the lower layer $\varepsilon_{r(i-1)}$ in all adjacent layer pairs above the trace, and vice versa for all adjacent layer pairs below the trace. The trace layer itself is ε_{r0} . Figure 18 shows an example system comprised of multiple layers of dielectrics around the conductive coil. In this example, the ‘‘Parylene-C’’ layer and anything surrounding the coil, such as air, are considered above the traces (n_1). The ‘‘FR4 Substrate’’ and ‘‘AlSi’’ layers are considered below the traces (n_2). The effective permittivities of adjacent layers

are then determined. The “media” permittivity, or air in this case, is subtracted from the “Parylene-C” permittivity, and a new effective permittivity for the upper layer is calculated as shown in equation 16. For the lower layer, the “AlSi” permittivity is subtracted from the “FR4 Substrate” permittivity and calculated in Equation 16. These values are summed to give the final, effective permittivity for parasitic capacitance calculations.

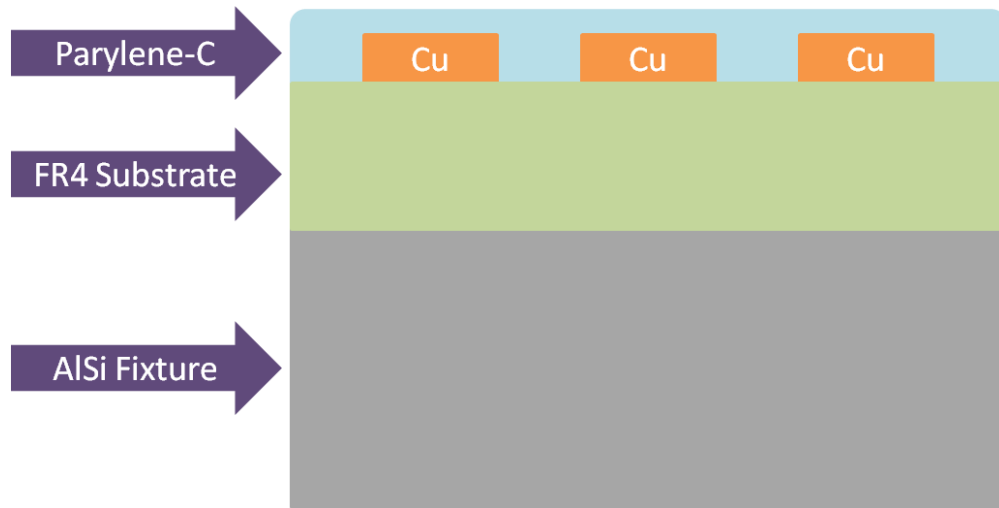


Figure 18: This is a typical stack of materials used in our sensors. The parylene layer is considered above the trace layer, and the alumina and PCB layers are considered below the trace layer.

Multiplying the resultant, free-space, intra-trace capacitance and the effect of adjacent dielectric layers provides the capacitance per unit length for an individual coil. Finally, the trace length in the coil is determined via

$$l = \frac{\pi(w + s)}{(2w + 2s)^2} (d_{out}^2 - d_{in}^2) \tag{17}$$

where w is trace width, s is trace spacing, d_{out} is the coil's outer diameter, and d_{in} is the coil's inner diameter [64].

Parasitic capacitance in sensors require a more complex approximation of the effects of adjacent materials, as the entire sensor stack is considered. Figure 18 shows a “half map” appropriate for determining parasitic capacitances of a coil, but Figure 19 shows the appropriate “full map” for accurately determining trace-layer interactions and parasitic capacitances of a multi-layered sensor.

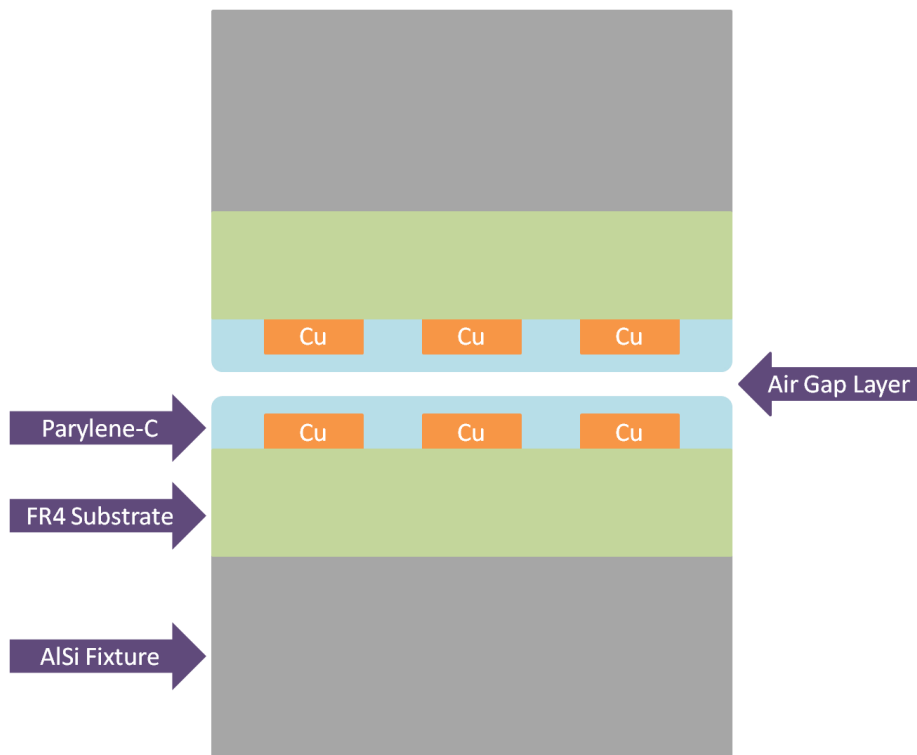


Figure 19: The “full map” of adjacent dielectric materials allows for a more accurate model of parasitic capacitance. The air gap layer accounts for voids present in the intervening layer.

The aspect ratio of the traces can introduce an additional air layer in the sensor stack, as seen in Figure 19. The thickness of the “Air Gap” layer is dependent upon the thickness of the intervening layer and the trace height. The model must account for all layers between the coils.

3.4.2 Mutual Capacitance

Mutual capacitance, or parallel plate capacitance, is derived by determining the overlapping areas of the two separate coil traces, such that

$$C_{mutual} = \frac{\epsilon_{eff_overlap} A_e}{d} \quad (18)$$

where $\epsilon_{eff_overlap}$ is the effective permittivity of the dielectric layer(s) between the coils, A_e is the overlapping trace area, and d is the distance between the coils. An accurate effective permittivity for overlapping coils considers the 3D structure of the traces as well as the fringing effects (capacitances other than orthogonal interactions between parallel coils). Effective intervening layer permittivity for overlapping capacitance is defined as:

$$\epsilon_{eff_overlap} = \frac{\epsilon_{r(int)} + 1}{2} + \frac{\epsilon_{r(int)} - 1}{2} \left(1 + \frac{12}{\frac{w}{t_{int}}} \right)^{-1/2} - \frac{\epsilon_{r(int)} - 1}{4.6} \frac{\frac{t_0}{t_{int}}}{\sqrt{\frac{w}{t_{int}}}} \quad (19)$$

where $\epsilon_{r(int)}$ is the average permittivity of the intervening layer(s) between the coils, w is the trace width, t_{int} is the thickness of the intervening layer(s), and t_0 is the trace height [65]. ϵ_{eff} is then determined by multiplying permittivity of free space ϵ_0 with the effective intervening dielectric permittivity:

$$\epsilon_{eff} = \epsilon_0 * \epsilon_{eff_overlap} \quad (20)$$

This expression, however, is dependent upon coil trace height and the intervening dielectric layer height. If the following ratio exceeds 0.2, then the effective permittivity adjustment can be ignored:

$$\rho = \frac{t_0}{d_0} \tag{21}$$

Where t_0 is trace height and d_0 is the starting intervening dielectric height. Additionally, this effective permittivity adjustment can be ignored if the trace width is significantly larger (about 20x) than the dielectric layer height [65].

When two coils are anti-aligned (mirror image) in a sensor setup, the overlapping area cannot be defined as the trace width times the trace length. Instead, the overlapping area is determined via a mask. The two mirrored coil traces are defined as polygons, and the polygons are converted to binary mask arrays where the trace is 1 and empty space is 0. A Boolean *AND* comparison is used to determine what parts of the masks overlap, and a ratio of the overlapping mask value over the original mask value is used to determine the final, electrical overlapping area, such that

$$A_e = (l * w) * ratio \tag{22}$$

where l is trace length, w is trace width, and *ratio* is the graphically defined ratio.

Several key assumptions are made to approximate the total capacitance of an anti-aligned parallel coil pair. First, the coils are assumed to be perfectly aligned for the trace overlap estimations. Second, the coils are assumed to be perfectly parallel to each other. Third, the surrounding dielectric layers are assumed to be homogenous and distinct from one another. Finally,

individual sensor coils are assumed to be equivalent, meaning $C_{par1} = C_{par2}$. The relevant geometric inputs for approximation of sensor capacitance are the number of turns on a coil, the trace width, the trace spacing, the trace height, the inside and outside diameters of the coil(s), the distance between coils in a sensor, and the thickness and dielectric constants of each adjacent dielectric layer.

3.5 Resistive Behavior and Mathematical Derivation

Resistance approximations have little impact on the prediction of the sensors' resonant behavior, except for coils with extremely low trace heights (e.g. - in a range between 0-10 μm). These coils would suffer from the skin effect if they were used in high frequency applications. If the calculated resistance is significantly less than the ratio of sensor inductance over sensor capacitance, however, then the effects of resistance on resonance can be safely ignored [66].

3.6 Mechanical Behavior and Mathematical Derivation

If a physical stimulus, such as force, modulates the capacitance or inductance of the parallel coil system, then it can be used as a force sensor. Passively resonating sensors can be designed to function as uniaxial force transducers for various loading conditions. If the mechanical properties of the intervening dielectric layer and geometric properties of each part of the sensor are known, and several design conditions are met, then an axially applied force can be correlated to a resultant shift in resonant frequency.

The sensors must have an intervening layer that has a significantly lower modulus than the substrate and trace materials. The ideal intervening layer is homogenous, and only *it* responds in kind to an axially applied load. The intervening layer material ideally responds linearly to an applied stress.

The overlapping area of the coils is calculated via:

$$A_m = \pi \left(\frac{d_{out}^2}{2} - \frac{d_{in}^2}{2} \right) \quad (23)$$

where d_{out} and d_{in} are outer and inner coil diameters, respectively. The two coils are assumed to be equal with respect to geometry. The mechanical properties of the intervening layer dictate the relation between applied force and resultant deformation:

$$\Delta d = \frac{F d_0}{A_m E_{inter}} \quad (24)$$

where F is applied force, d_0 is the thickness of the intervening layer, A_m is the area of a coil, and E_{inter} is the compressive modulus of the intervening layer. This expression is derived from the stress-strain relationship of a linearly elastic material.

In thin intervening layer cases, however, the aspect ratio of the traces can introduce non-uniform contact between coils. As such, the area where traces overlap is considered the mechanical area, rather than the total coil area. The area from Equation 22 is used in place of the area found via Equation 23. Generally, this area adjustment must be done if d_0 is smaller than the trace spacing. Additionally, the trace width and trace space must be adjusted to reflect the actual overlapping mechanical area, as defined by

$$w = w + \frac{d_0}{2}, \quad s = s - \frac{d_0}{2} \quad \text{given } d_0 < s$$

(25)

where d_0 is the unloaded intervening layer thickness, w is trace width and s is trace spacing. The total deformation of the sensor is assumed to only be the deformation of the intervening layer, so the total thickness of the dielectric layer given an applied force is

$$d = d_0 - \Delta d$$

(26)

where Δd is the strain due to applied force. Finally, all d terms in the above electrical expressions are replaced with Equation 26 to reflect the effect of an axially applied force on the sensors at any point in time.

4. SPECIFIC AIM 1: RESULTS

MATLAB was used to predict coil and sensor resonant behavior. After inputting independent variables, the code executed calculations for expected electrical and mechanical behavior of coils and sensors. Results were presented as resonant frequency in megahertz.

Coil parameters of outer diameter, inner diameter, trace width, trace spacing, trace height, substrate permittivity, and substrate thickness were inputs for the model. Then, dielectric parameters were input, including dielectric layer thickness, compressive modulus, and relative permittivity. Finally, the thickness and relative permittivity of each material adjacent to the coils were input, including the surrounding air and surrounding media (i.e. alumina silicate fixtures for testing). A total of fourteen different variables were input into the force sensor model.

Following variable setup, various parameters were run through functions to return values such as coil trace length, number of turns and expected intervening layer strains. These calculated properties and responses were then input into both the individual and mutual inductance and capacitance calculations.

Both spiral coil inductance models were calculated. Mutual inductance was calculated following coil inductance calculations. MATLAB elliptical integrations require squaring of the input term prior to integration, or the returned value was incorrect. Coil and mutual inductances were summed to give a total inductance.

Mutual interactions were calculated. Mirrored spiral trace area overlap was calculated via masking. A polygon representing the current coil design was drawn based on the input geometric parameters. The poly2mask function from MATLAB's Image Processing Toolbox then drew the coil as a binary array where 1 and 0 represented trace and space, respectively. A second mask was mirrored and overlaid, and an AND comparison of both masks' ones returned a ratio representative

of overlapping areas. Higher grid resolution increased accuracy and computation time. Coil capacitance was then calculated. Discrete calculations for each layer pair allowed for easy setup of different sensor stack configurations and layer ordering. Coil and mutual capacitances were summed to give a total capacitance.

Coil resonant frequencies were calculated given the coil inductance and capacitance. Sensor resonant frequencies were calculated given the total inductance and capacitance. If the sensor frequency exceeded the coil frequency, the code set the sensor frequency at the coil frequency instead. A large enough separation between coils resulted in only the coil frequency being read, so the code reflected this behavior.

Empirical adjustments were applied as needed following final coil and sensor frequency predictions. Based on initial results from air and solid sensor measurements, the model employed a small empirical adjustment of the final resonant frequency for solid force sensors. This correction tweaked resonant frequency predictions to increase solid sensor accuracy at small coil displacements ($< 60 \mu\text{m}$). This expression:

$$f(x) = a + \frac{b}{x} + c * \ln(x) \tag{27}$$

was representative of the behavior of the sensors, with both asymptotic and logarithmic behaviors occurring at smaller and larger intervening layer thicknesses, respectively. The measured data curves were fitted to this expression via MATLAB, and the coefficients were modified in $f(x)$ to adjust the model output to more accurately represent the behavior of the measured force sensor data. The scaling $f(x)$ was added to the final solid sensor resonant frequency predictions to more

accurately reflect the measured data. Coefficients used in the empirical adjustment expression (Equation 27) are currently set at $a = 0$, $b = 1.5e^{-4}$, and $c = 0.5$.

5. SPECIFIC AIM 2A: RATIONALE BEHIND SENSOR DESIGN

Wireless, passive resonant force sensors have the potential to revolutionize smart implants. Their small form factor allows them to be installed in modified cervical interbody implants, enabling passive, wireless measurement of forces. These wireless, passive resonant force sensors must fit within the space of an intervertebral body implant. To function as a clinically useful tool, the sensors must be developed based on physiologic constraints.

5.1 Disc Morphometry

The critical parameters for designing a modified lower cervical spine fusion interbody implant, and subsequently, smart cervical interbody implants, are endplate dimensions and disc height. As shown in Figure 20, these critical dimensions have been previously characterized.

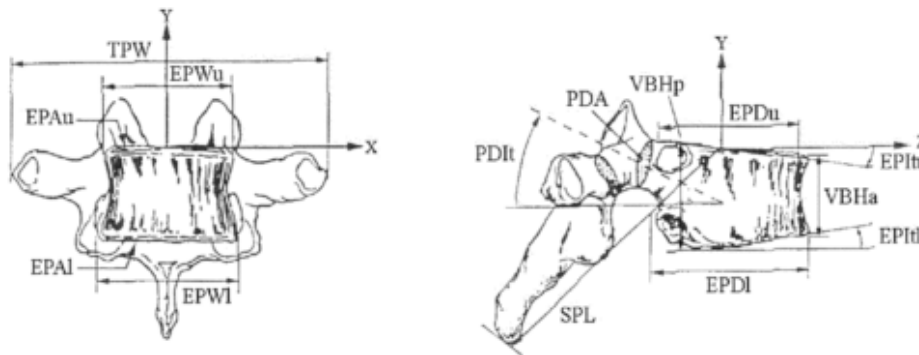


Figure 20: Cervical vertebral morphometry is key to smart implant design. Relevant parameters are upper endplate width (EPWu), lower endplate width (EPWI), upper endplate depth (EPDu), and lower endplate depth (EPDI) [67].

A morphometrical study of 150 cadaver cervical vertebrae provided anteroposterior (A-P) and transverse diameters of C3-C7 vertebral bodies. All features of interest were measured by hand. Disc morphometry was assumed to be elliptical [68].

Another morphometrical study of 38 cadaver cervical spines reported geometries of C2-T1 cervical discs. Specimens included both healthy and degenerative samples, providing some insight into the morphology of degenerated discs [69].

A morphometrical study of ten cadavers reported an in-depth analysis of whole C3-T1 vertebral morphometry. Average disc parameters were calculated using the lower dimension-upper dimension (e.g. – C3 lower C4 upper) of each vertebra pair in a functional spinal unit [67].

Another morphometrical study of twenty cadaveric cervical spines reported detailed measurements of disc heights throughout the lower cervical spine. Anterior versus posterior heights of each disc were assessed, providing more detailed on disc heights than most studies [70].

Table 1: Mean lower cervical spine interbody space morphologies.

	C3-4	C4-5	C5-6	C6-7	C7-T1
A-P diameter (mm)	14.6	14.8	14.9	15.4	15.3
Transverse diameter (mm)	14.5	15.0	15.9	19.3	22.5
Disc footprint (mm²)	193.0	214.5	248.5	268.6	322.4

The increase in disc area coincides with an increase in loading down the spine. Table 2 shows the average measured disc height in the lower cervical spine.

Table 2: Mean lower cervical spine disc heights.

	C3-4	C4-5	C5-6	C6-7	C7-T1
Posterior Height (mm)	2.78 ± 0.93	2.45 ± 0.79	2.92 ± 0.64	2.46 ± 0.59	2.93 ± 1.05
Anterior Height (mm)	4.34 ± 1.18	3.95 ± 1.37	3.55 ± 1.37	3.55 ± 0.76	3.67 ± 1.17

Focusing on the C5-6 FSU parameters described in the literature, the resultant implant and sensor combination is designed to fit within a space of 14.9 mm by 15.9 mm. The maximum height of the modified smart implant is designed to be 2.92 mm posteriorly and 3.55 mm anteriorly if no tissue resection is performed during discectomy.

5.2 Expected Loads in the Cervical Spine

While loads in the cervical spine have never been measured before, biomechanical models were assessed to determine physiological loading ranges and limits in the cervical spine. The load limit of the entire FSU can be as low as 1,150 N and as high as 3,600 N with respect to the vertebral body, the posterior elements, and the disc [71]-[73].

Typical lumbar loads during activities of daily living are 500-600 N in standing, 1100 N during flexion, and 1600 N during carrying of weights [74]. There are no examples of *in vivo* measurement of forces in a human lower cervical spine, but the cervical spine should not experience forces higher than those exhibited in the lumbar spine.

The lower cervical spine in neutral position is estimated to be likely subjected to 45-122 N axial load. This neutral load typically refers to the weight of the head plus passive forces resulting from supporting soft tissue [75]-[77]. These neutral loads are implemented as preloads in biomechanical and cadaveric models of the cervical spine. The T1 vertebrae experiences an average load equivalent to 9% body weight, which is close to the reported preloads estimated in the lower cervical spine region given average body weight [78].

Predicted loads in the disc space during normal motion vary significantly. Some studies report peak cervical loads as low as 80 N during normal flexion, while others report compressive loads as high as 1700 N in extension [73], [77]. The estimated loads that easily exceed 1000 N

conflict with reported disc load limits [74]. Studies modeling compressive load distributions across the lower cervical spine peak between 250-350 N in flexion and extension [76], [79]-[81].

Direct measurement of *in vivo* forces in the cervical spine in human and animal models has provided additional insight into the forces that might be passing through the intervertebral disc space. Peterson *et al* noted that the anterior plate in a fused cervical spine measured approximately half of an applied load. Based on estimations of load sharing through an anterior cervical plate, the estimated load passing through the interbody space might be 250 N [82]. Another similar study looked at load sharing on a cadaver spine by performing a corpectomy on the C5 vertebra and replacing it with a load cell. Results indicated that 75% of the total load passed through the vertebra regardless of whether a plate was present or not. The peak load through the implant equates to approximately 225 N, implying that a total of 300 N passes through the C5 vertebra [83].

Additionally, some models provide resultant moments of cervical vertebrae in motion. Knowing morphometry of the cervical vertebrae allows for estimation of the resultant forces present in the joint. Other studies provide measured stiffness values, allowing estimation of expected loads during normal motion. Given the data from cadaver models, estimates of compressive axial loads from approximately 400 to 800 N [75]-[77].

The axial load of the lower cervical spine during normal motion is not expected to exceed 500 N. Based on these data, a sensor that measures up to 1000 N while being able to resolve ± 1 N should be enough to characterize forces in the cervical spine.

5.3 Sensor Design to Facilitate Fusion

Fusion success is dependent upon proper load sharing of forces going through both the cervical implants and the vertebrae itself. Many commercial interbody implants have a cage design

to allow for insertion of bone grafts. The fabricated sensors should have a center hole with a minimum inner diameter of 3 mm to support bone grafts and other bone growth promoters.

5.4 Considerations for Fabrication

The sensor's mechanical properties determine how quickly and sensitively the sensor responds to an axial compressive load. The sensor's electrical properties determine sensor resonance, signal quality, and sensitivity to variations in the measurand. Additionally, sensor materials were selected from those which were conducive to quick and inexpensive fabrication.

The wire (or conductive trace depending on the fabrication technique used) is a conductive material that serves as the functional, resonant component of the wireless, passive sensor. For prototyping, copper is typically used due to its universally excellent electrical properties. Copper can be shaped at the micron level through etching, easily allowing for production of planar, Archimedean spiral geometries small enough to fit within a cervical interbody implant. These spiral coils, however, need to be supported by a substrate layer. The ideal substrate for a passive resonator force sensor affixes and supports the spiral coil to prevent failure against applied forces, and the substrate should withstand applied forces with minimal deformation. The substrate's modulus should also have a higher modulus than the intervening layer to ensure predictable sensor deformation. Finally, the intervening layer separating the coils in the sensor dictates what the sensor measures. In the case of a force sensor, the intervening layer should deform predictably in response to an applied load, which produces a predictable change in the electrical behavior between the two coils in the sensor. It is this deformation that results in a change in resonant frequency, allowing correlation of an applied load to a measured resonant frequency. Therefore, the selected intervening layer should deform predictably in the selected loading range. The intervening layer should be uniform after application so that the sensor can deform consistently

and predictably under an applied load. Finally, the intervening layer acts as a dielectric to ensure only mutual inductance and capacitance interactions respond to an external input. Ideally, the dielectric constant, or the relative permittivity of the intervening solid layer, is as high as possible (at least greater than three), as lower dielectric values reduce return-loss signal strength and resultant sensor readability.

5.4.1 Examples of Manufactured Coils/Sensors

The first coils manufactured for wireless, passive resonant sensors were handmade 34, 38, or 40 gage copper magnet wire wound around a mandrel. The wire was wound through an epoxy, which provided support for the coil. Preliminary force sensors made using these coils were separated by a hand cut layer of polydimethylsiloxane (PDMS) [54]. These passive resonant force sensors were functional but highly variable in performance per geometry, and their fabrication was time intensive and technical.

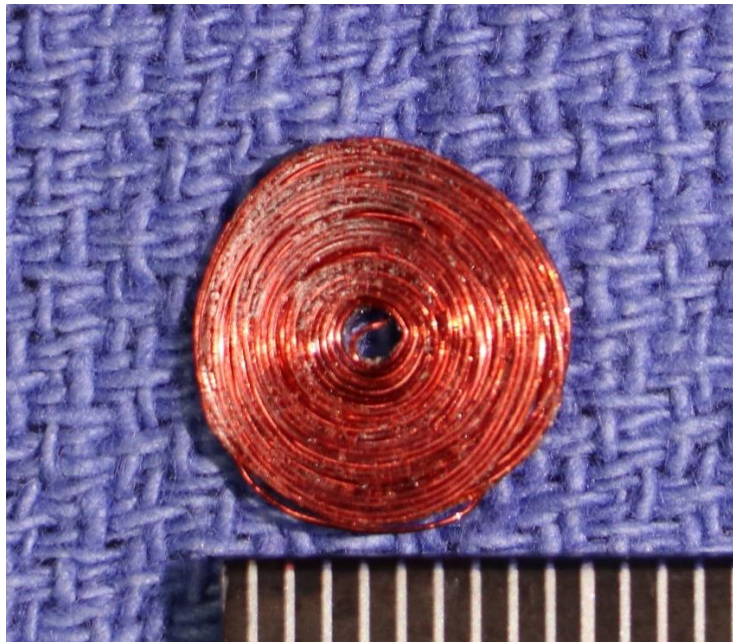


Figure 21: Example of a handmade sensor comprised of two epoxy-set, handwound coils separated by PDMS.

Microfabrication enables precision manufacture of coils, creating coils with consistent geometries. Consistent coil geometries between batches result in consistent electrical behavior. This fabrication method can yield micron scale coils. One-millimeter thick Borofloat glass wafers were coated in nickel. This thin nickel layer was coated in photoresist and pattern UV cured. The wafer was then etched, revealing a patterned nickel layer for copper electrodeposition. This copper layer was typically 10-15 μm thick. The Borofloat wafer acted as the substrate in this case, though microfabrication enables use of a wide variety of substrates [56].

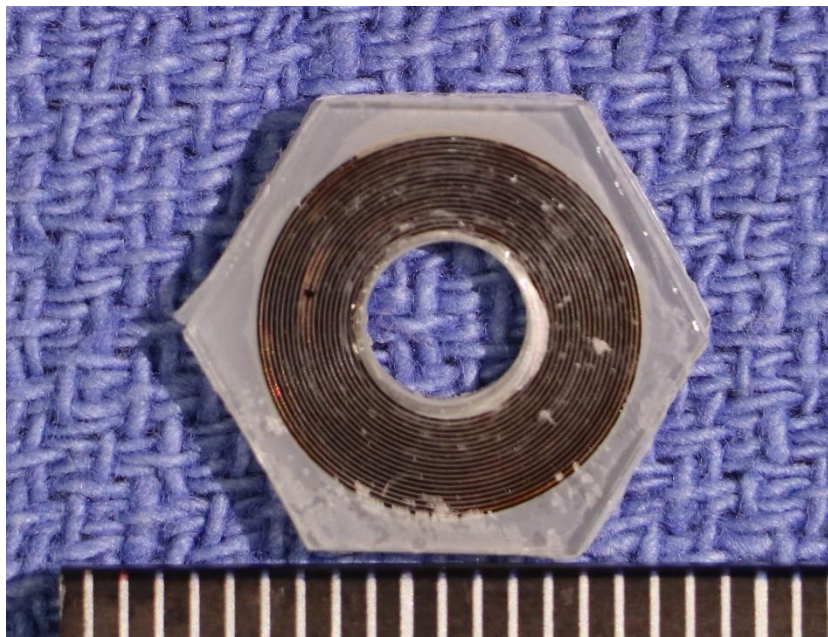


Figure 22: Example of a microfabricated force sensor comprised of two Borofloat coils with etched copper traces, separated by parylene C polymer.

Microfabricated force sensors are highly adaptable to a wide array of applications, but cost, specialized equipment, technique, and turnaround time hinder this fabrication method for rapid

prototyping during sensor testing and development. These limitations are especially apparent when rapid prototyping of an array of passive resonant sensors is needed.

Printed circuit board (PCB) fabrication uses well established materials and methodologies to inexpensively batch build circuitry for a wide array of electrical applications. This fabrication technique provides a method to quickly and inexpensively produce functional and consistent passive resonant force sensors.

5.4.2 PCB as a Candidate Fabrication Method

A single copper layer is etched, like microfabrication techniques, to produce a planar spiral coil structure. The substrate layer is composed of a glass fiber reinforced epoxy laminate, which serves as an excellent electrical insulator. The common industry designation for this substrate material is FR4, though formulations may vary slightly between manufacturers. FR4 is a NEMA (National Electrical Manufacturers Association) class of material designed to serve as both an electrical insulator and flame retardant in electrical applications [84]. This material is commonly used in high frequency antenna applications. Additionally, the PCB substrate material has excellent mechanical properties and is resistant to cracking and delamination, making it a good candidate for high load force sensors. FR4 limitations to consider include small changes in dielectric properties due to moisture uptake, orientation dependent mechanical properties, and relatively low thermal limits [85], [86].

5.4.3 PCB Manufacture and Material Properties

PCB manufacturers have certain limitations to consider for PCB coil design and manufacture. Manufacturers have minimum copper feature size and minimum space between copper features that they can produce. These values are typically 4 mil, or approximately 102 μm , though some can go as low as 3 mil, or approximately 76 μm . Smaller feature sizes can only be

produced via microfabrication. There is also a minimum copper “weight”, or volume, used in manufacture, which dictates a copper layer’s thickness. The resultant thickness is dependent upon the design and volume used, but typical minimum weights are 1 oz of finished copper. The minimum distance between copper feature and board features such as cuts, holes, and score lines is dependent upon a manufacturer’s tooling capabilities. Typical minimum distances are 5 mil, or 127 μm . There is a minimum substrate thickness required for standard PCB fabrication. However, a thick capping layer is important for reducing parasitic capacitances, so the specified minimum substrate thickness for FR4 is 0.5 mm [58]. A wide array of options is available for PCB substrates, but primarily, the substrate ideally has a high dielectric constant exceeding three, a modulus high enough to withstand the peak 1000 N compressive load with minimal deformation, and a high glass transition temperature to withstand the sensor manufacture process. These limitations are all considered in designing a wireless, passive resonant force sensor for lower cervical spine interbody implants. The listed FR4 substrates in Table 3 have the necessary mechanical and electrical properties to serve as a good basis for a passive resonator force sensor.

Table 3: Relevant material properties of FR4 substrates used in force sensor development, manufacture, and testing [87]-[90].

<i>FR4 Class Mat'l</i>	<i>Young's Modulus</i>	<i>Permittivity</i>	<i>Loss Tangent</i>	<i>T_g (°C)</i>	<i>Moisture Absorption (%)</i>
GA-170-LL	14-22 GPa	4.5 @ 1GHz	0.035 @ 1GHz	175	0.35
185HR	14-22 GPa	4.13 @ 100MHz	0.0158 @ 100MHz	180	0.15

T_g is the glass transition temperature of the substrate material. High glass transition temperature ensure that the coils can be used with intervening dielectrics that require high temperatures for placement. The material properties of the candidate FR4 substrates are suitable for force sensors, as they withstand the designated 1000 N peak load with minimal deformation. Their high relative permittivity also ensures stronger mutual capacitive interactions within sensors, improving overall sensitivity. The low moisture absorption limits physical changes in the sensor structure and therefore, PCB sensors are not susceptible to long term damage.

5.5 Final Design Constraints

Given these morphometrical and fabrication constraints, the sensors follow the engineering constraints in Table 4.

Table 4: Engineering constraints derived from physiological constraints and manufacturing constraints.

Engineering Constraints	Values
Maximum outer diameter (OD)	15 mm
Maximum Sensor Height	2.92 mm
Minimum Copper Trace Width (Tw)	76.2 μm
Minimum Space between Traces (Ts)	76.2 μm
Minimum Trace Height (Th)	5 μm
Target Sensor Resonance Range	20-150 MHz

The minimum trace height is included due to the skin effect. The skin effect occurs when a conductor is exposed to high frequency alternating current, resulting in a denser current profile near the surface of the conductor. This leads to a significant increase in resistance in those regions, and if the conductor is too thin, the overall resistance of the conductor increases. Additionally, the

optimal sensor has a starting target resonant frequency of 68 MHz. This frequency addresses two problems for *in vivo* and potential clinical use. First, this frequency is unlikely to interfere with any currently existing equipment operating in regulated frequency bands [91]. Secondly, this frequency sufficiently penetrates soft tissue without too much loss in range or power, and higher frequencies may cause localized heating causing issues with potential *in vivo* applications [92]. The ideal functional and measurable sensor resonates in a frequency band of 20 to 150MHz.

5.6 EAGLE Designs

5.6.1 First Generation Coil Designs

All coils were designed using CAD (Autodesk EAGLE, San Rafael, CA, USA). First generation coils are designed for prototyping initial force sensor designs and development of the passive resonant force sensor model. All subsequent designs were adapted for custom interbody implants built for a human C5-C6 interbody space. Initial designs introduced variation in geometry, but no true parametric study was employed with more focus placed on validation of coil behavior, manufacturing process, and force sensor behavior. The selected PCB manufacturer limited the feature size minimum to 4 mil. To simplify force sensor model validation, the trace width and trace space of all coil designs were equivalent. PCB solder masks and silk screens were also removed, leaving the copper traces bare for later intervening layer manufacture.

Table 5: First-generation coil design parameters.

	D2	D3	D7	D8
OD (mm)	10	8	8	8
ID (mm)	5	4	4	4
TW/TS (µm)	152	152	203	102

The selected substrate was FR4 class GA-170-L. The FR4 thickness is 0.787mm, and 1oz of copper volume was used. The resultant designs are shown in figure 23.

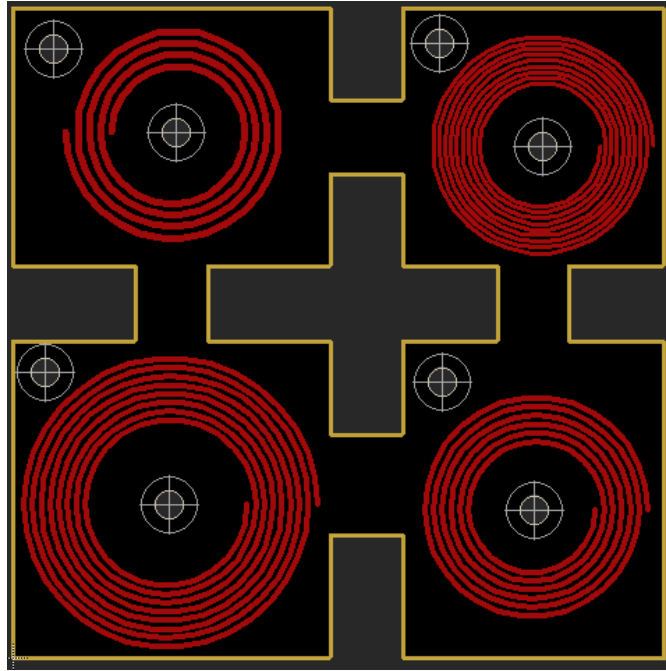


Figure 23: Four first-generation coils were designed and laid out in EAGLE to fit within custom cervical interbody implants. Center and corner drill-holes were included as alignment features.

Additional specified features included 1mm diameter drill holes in the center of the coils and at a corner of each coil tab. These holes served as alignment features for sensor manufacture.

5.6.2 Second Generation Coil Designs

Second generation coils were designed via a parametric study. The parametric study looked at the predicted coil resonant frequencies based on minimum and maximum geometry values. Constraints were developed to provide designs that can feasibly fit within the prescribed physiological/implant space while maintaining minimal sensor function. The newly selected

manufacturer achieved the desired three mil minimum copper feature sizes. Geometric parameters including the predefined design constraints are listed in table 6.

Table 6: Minimum and maximum geometric parameter constraints for second-generation coil parametric study.

Geometric coil parameter	Min	Max
Outer diameter	8mm	12mm
Inner diameter	3mm	6mm
Trace space/width	76.2 μ m	300 μ m

Minitab (Minitab, State College, PA, USA) was employed to determine effects of each geometric parameter on resonant frequency. A main effects analysis compared the strength of each independent variable on the resultant dependent variable. Horizontal slopes indicate no effect on the dependent variable, while steep slopes indicate a significant effect on the dependent variable. This study determined that the outer diameter of a coil is most impactful factor in determining resonant frequency. Doubling the outer diameter reduced the resonant frequency to a ¼ of the original value. Surprisingly, the inner diameter had less of an effect on resonant frequency. This trend was likely a result of the OD having the greatest effect on the number of turns within the coil. Trace width and trace spacing also had some impact on resonant frequency with similar trends. The input trace heights ranging from 15 to 50 microns had an insignificant effect on the resultant resonant frequency.

Results from this analysis showed that the lowest resonance force sensor will have a maximal outer diameter, a minimal inner diameter, and minimal trace width and spacing, which increases the overall copper area. This trend coincides with an increased coil capacitance and

inductance resulting in a reduced resonant frequency. Understanding the effect of each geometric parameter informs the most impactful design variations for a parametric study. The ideal force sensor design maximizes force sensitivity and resonant signal quality via coil geometry irrespective of intervening material behavior.

Given the behavior of the independent geometric variables, sixteen coil designs were developed to explore possible candidates for the second-generation designs. Various combinations of minimal and maximal geometric parameters were included to provide an idea of coil and sensor resonant frequencies. Having a wide variety of designs ideally tests the model to ensure that it encompasses a spectrum of force sensor designs with little error.

Six out of sixteen coil designs were selected for manufacture. The first design (D1) replicated a successful design from the first generation, and it also provided a point of comparison for coil manufacturing quality. The third design (D3) targeted a final sensor resonant frequency of 68 MHz, given an approximate 100 μm layer of some intervening layer with a relative permittivity of 3. The seventh design (D7) provided the lowest possible resonant frequency given the design constraints. The ninth design (D9) was a disc design with a target frequency of 68 MHz. This “disc” design with no inner diameter was included for comparison to previous disc designs. The fifteenth design (D15) was a coil built around all minimal constraints. The sixteenth design (D16) was a coil built around all maximum constraints. Table 7 shows the geometric parameters for each coil.

Table 7: Geometric parameters of the selected second-generation designs.

	D1	D3	D7	D9	D15	D16
OD (mm)	10	11	12	11	8	12
ID (mm)	5	4	3	0	3	6
TW/TS (μm)	150	100	76	100	76	300

The selected substrate was FR4 class 185HR. FR4 thickness is 0.77mm, and 1oz of copper is used.

Figure 24 shows the CAD layout of this generation.

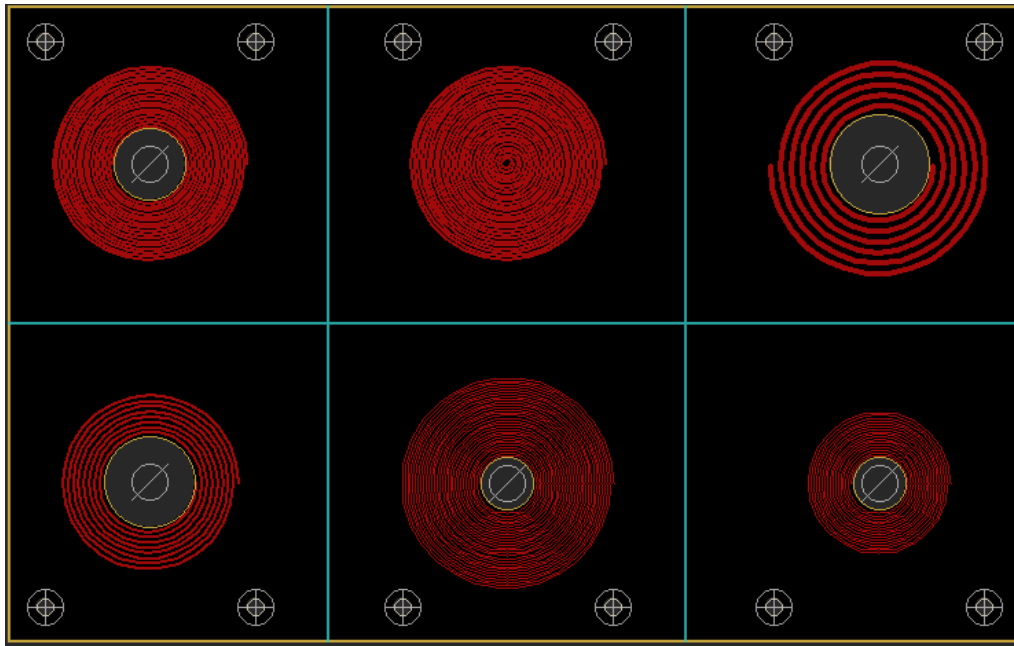


Figure 24: Six second-generation coils designs were selected and laid out in EAGLE. A second corner drill-hole was added for more consistent alignment in air testing and solid sensor fabrication.

Additional features included modified drill holes on one edge of a coil tab. These holes provide an easier means to align coils during sensor manufacture. The inner diameters were also pre-drilled by the manufacturer.

5.6.3 Third Generation Coil Designs

Third generation coils were built from the D15 design, or the coil built around all minimal constraints. No design changes were made to the coils, and the board was a simple rearrangement and repeat of the D15 coil design. This design was selected for its ability to produce solid sensor designs within the desired 20-120 MHz range, regardless of parylene C layer thickness.

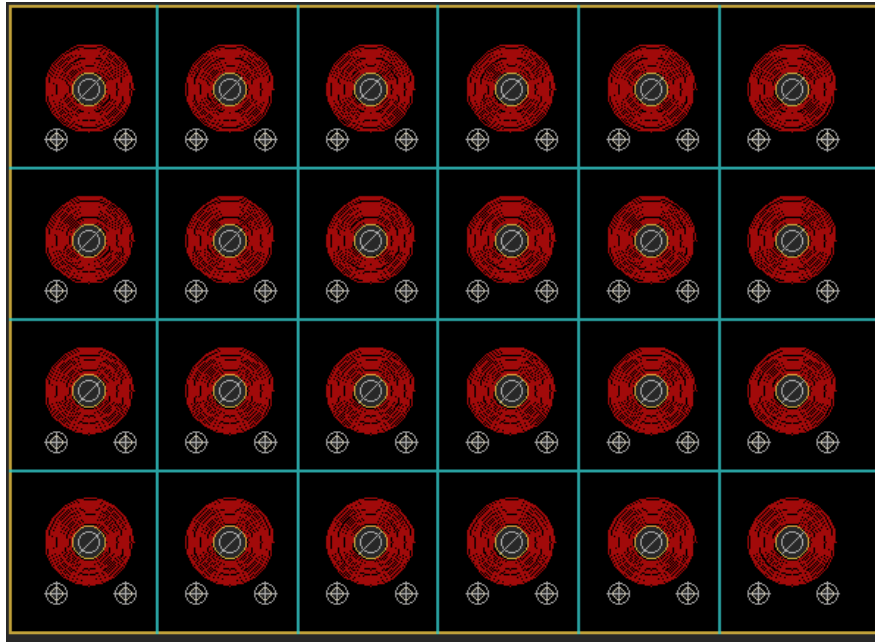


Figure 25: Design G2D15 was laid out in EAGLE as the candidate for a third generation run of coils. This design was selected for fabrication of a set of sensors with varying intervening layer thicknesses as part of model validation.

This generation was developed for variable intervening layer height testing and validation. Because of limitations in the CAD program, manufactured coil geometries deviated slightly from their designed values.

5.7 Intervening Layer Selection

Finally, the intervening dielectric layer provides the wireless passive resonant sensor its functionality. Material selected for force sensing strains predictably in response to an applied force, changing the distance between the coils that comprise the sensor and the resultant, measurable electrical behavior. Mechanical parameters considered for a force sensor's intervening layer include Young's modulus, creep, and failure limits. Candidates for an intervening layer for a passively resonant force sensor ideally respond predictably and linearly to a physiologically relevant axial loading range of 0-500 N with a peak of 1000 N. Additionally, the target sensitivity for these force sensors is in ± 1 N increments. Creep and stress relaxation are ideally minimized to limit sensor drift over long loading periods. Moisture uptake is ideally limited to reduce sensor drift over the sensor's lifetime. The dielectric constant is the primary electrical property to consider in intervening layer selection. The ideal dielectric constant of the material is greater than three, with sensor performance and readability improving as permittivity increases. Material thickness is ideally controllable from the micron scale to the millimeter scale, and a uniform deposition profile would ensure even, parallel alignment between the two coils comprising the sensor. Finally, transitioning to clinical studies necessitates use of ISO 10993 or USP Class VI certified biocompatible materials [93].

5.7.1 Candidate Materials for the Intervening Layer

Given the size constraints and the expected loading range, the ideal material's compressive modulus is in the range of 0.5 to 3 GPa. This mechanical constraint coupled with the high required permittivity restricted available materials to polymers and ceramics. Table 8 shows a subset of selected materials close to or meeting these initial requirements [93].

Table 8: Selection of polymers and ceramic composites that are close to or fit within the defined intervening layer mechanical and electrical constraints.

Material	E (GPa)	Permittivity	Manufacture
Polypropylene	1.93	2.7	Thermoplastic
LDPE	0.232	2.33	Thermoplastic
Anhydride Epoxy	2.58	3.36	Thermoset
Mineral Filled Epoxy	0.98	5.04	Thermoset
Urethane	0.167	3.33	Thermoset
Cyanite Resin	2.8	2.73	Thermoset
Parylene C	2.4-3.2	2.95	CVD
Parylene N	2.4	2.65	CVD
Parylene D	2.8	2.8	CVD

Thermoplastics are a class of plastics that are soft and malleable in high temperatures and harden in cool temperatures. These materials exhibit excellent material properties for the defined constraints, but they can be exceptionally difficult to manipulate for precise manufacturing. Their high melting points pose issues with substrate compatibility. Controlling the thickness of the material is difficult and creating thin layers as low as 100 μm requires specialized molds and tooling. Thermoplastic bond strength to substrates is variable and, in some cases, requires use of an adhesive to facilitate bonding [94].

Thermosets are a class of materials that are initially soft and harden through exposure to a curing agent. This class of materials typically includes resins and composite ceramic epoxies. Material properties are highly variable, but candidates like anhydride epoxies and cyanite resins provide mechanical and electrical properties that fit the defined intervening layer constraints. Thermosets are easier to manipulate in manufacture, as they bond more readily to a given substrate.

They also produce uniform profiles when used with a mold. Their manufacture is also significantly more compatible with a PCB's FR4 substrate thanks to their lower temperature requirements for setting and curing. The primary issue with using thermosets is heterogeneity due to composition, material distribution, and air bubbles in vacuum free curing. These factors can make sensor electrical behavior unpredictable. Many thermosets are also not biocompatible [94].

Chemical vapor deposition (CVD) involves deposition of a material under high heat and vacuum. Material is sublimated, chemically modified via heat, and cooled down to deposit in a uniform, homogenous pattern. Deposition layers can be micron thin and can be as thick as 100 μ m in a single deposition. Their manufacture requires specialized equipment, but CVD material deposits uniformly, providing excellent sensor manufacture consistency. Layer thickness is also controllable down to the micron [94]. Parylene polymers are a class of biocompatible CVD materials that satisfy the intervening layer requirements for force sensors.

5.7.2 Suitability of Parylene C for Force Sensors

Developed in 1947 and refined in 1966, parylene polymers provide the additional advantages of homogenous deposition, as the vapor deposition process is incredibly efficient [95]. Parylene can also bond to itself when supplied with high temperatures and pressures, and the annealing temperatures do not exceed the glass transition temperature of the selected FR4s [96]. In addition to the other benefits of CVD parylenes, parylene is pinhole free, meaning that little moisture will be absorbed. Three types of parylene are commonly used in coating and deposition. Parylene N is the conventional parylene, with D and C being derivatives. Parylene D serves as an excellent coating and barrier against external elements, but it does not coat uniformly compared to the other parylenes. Parylene C is the standard poly(p-xylylene) monomer with a chlorine group attached to it. Parylene C also has the lowest temperature requirements of the three for polymeric

deposition at 90°C, making it more compatible with FR4. Material properties of parylene C are listed in Table 9.

Table 9: Relevant material properties of parylene C for force sensors [97]-[100].

	Young's Modulus	Poisson's Ratio	Dielectric Constant	Water Absorbance	Creep
Parylene C	1.5-3 GPa	0.4	2.95 @ 1 MHz	> 0.1 % @ 24 hrs	0.06% below T _g

Where T_g is the glass transition temperature. Given the dimensions of the sensors and the compressive modulus of parylene C, parylene C is expected to have a measurable, linear deformation in response to a 500 N load. Additionally, it is stiff enough that the coils do not come into contact at a 1000 N applied axial load. Creep is minimal, meaning that sensor drift is limited over long loading durations. Parylene C is an inert material, and moisture uptake is also low, which protects the conductive traces and allows the sensors to function for long periods of time in a harsh environment. Parylene C is the ideal intervening material for PCB based force sensors due to its ability to uniformly coat the PCB coils. The batch manufacture process allows for high throughput of force sensor prototypes. It also exhibits the highest relative permittivity of the parylene polymers, making it a strong candidate for fabricating sensors with high quality resonant signals.

The cervical interbody space and existing commercial interbody implants were assessed to establish design constraints for a wireless, passive resonant force sensor that fits within a modified cervical interbody implant. PCB-based coil manufacture is selected due to the ability to rapidly and inexpensively prototype force sensors. PCB manufacture has apparent limitations in clinical

force sensing applications due to issues with biocompatibility and minimal feature sizes, but PCB sensors are the best choice for creating an array of sensors for validation of an analytical model. Parylene C as a material meets the design requirements for building force sensors that are designed for use in smart cervical interbody implants. Physiologically relevant parameters and manufacturing constraints are considered in the design of these sensors, and these factors are also considered in selection of substrate material and intervening material.

6. SPECIFIC AIM 2A: METHODS

The quality of manufacturing methods is critical for sensor performance and repeatability. Because of the scale of the sensors and their sensitivity to minute changes in geometric parameters and surroundings, consistent fabrication techniques are critical to building reliable, functional force sensors. Additionally, passive resonator force sensor model validation is dependent upon sensors with known geometries that are consistently measurable.

6.1 Coil Design and Manufacture

Sensors are comprised of a pair of coils (mounted on a substrate) which are then assembled parallel and anti-aligned with an intervening dielectric layer. All coils used for model validation were fabricated using printed circuit board (PCB) fabrication techniques by commercial manufacturers. Designs were drafted in EAGLE (Autodesk, San Rafael, CA, USA). Coil traces were built on a single layer. Alignment holes were also included in the board design. The center of the halo coils was marked for drilling as well. The copper was uncoated, and standard silkscreen enamels on the substrate was masked, as it added complexity to predicting the electrical and mechanical behavior of the sensors.

The CAD was sent to the manufacturer, the substrate material was specified as high temperature FR4. The copper volume was also specified. The first generation of coils was produced by Sunstone Circuits (Mulino, OR, USA), but further iterations were produced by PCB Solutions (Reno, NV, USA) because of quality issues with Sunstone.

6.2 Preparing Coils for Parylene Deposition

Coils were wiped down using Technicloth (Texwipe, Kernersville, NC, USA) and isopropyl to remove large particulates originating from handling and manufacturing. The coils

were then placed in an ozone cleaning system (PSD Pro Series, Novascan Technologies, Ames, IA, USA). Coils were exposed to ultraviolet light and ozone (UV/O₃) for 1 minute, which cleaned the coil surface of potential organic contaminants that could interfere with the steps that followed. Ozone cleaning had the added benefit of improving polymer bonding to treated surfaces [101].

Parylene C tends to have poor adhesion to most surfaces due to its inertness and stability. Proper adhesion is paramount for force sensors to prevent sensor breakdown via delamination and slippage under load. To assist in adhesion of parylene C to the coil surface, an adhesion promoter was used. An adhesion promoter ensures that the normally inert parylene C bonds to the coil substrate. A-174 Silane (*3-(Trimethoxysilyl)propyl methacrylate*) (Sigma Aldrich, St. Louis, MO, USA) is a popular adhesion promoter for parylene C. The silane acts as an intermediary by covalently bonding with both the substrate and the parylene [102].

Coils were pretreated with a monolayer of silane following the ozone cleaning. The silane was placed using vapor deposition [102], [103]. The coils were placed inside an airtight container along with 15 μL of Silane. The coils were incubated in an oven for 60 minutes at 60° C. The coils were immediately removed from the container following incubation.

6.3 Parylene Layer Deposition

Parylene C, or *2-chloro-p-xylene*, is a form of *poly-p-xylene*, which can be formed into a conformal, micro-scale film. The polymer film is created via pyrolytic polymerization, as shown in Figure 26. The resultant film is composed of linked, linear polymers. This process creates no byproducts and unreacted parylenes, so the resulting parylene polymer film is homogenous [95].

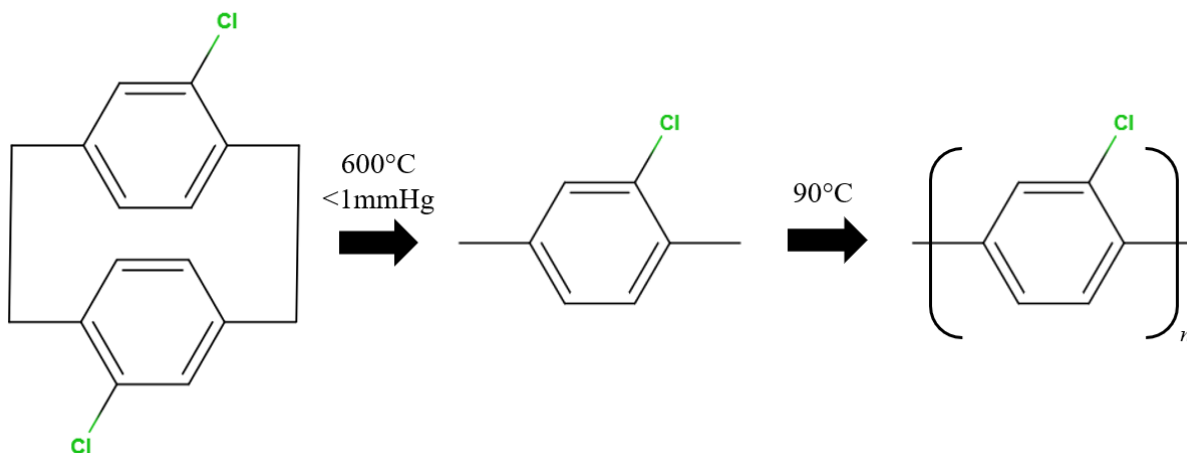


Figure 26: Parylene C dimer is pyrolyzed into its monomer form, then it as it cools down, it polymerizes into a uniform, conformal layer on a downstream surface.

The parylene C deposition process was done using a Union Carbide Model 1050 Parylene Deposition System (Houston, TX, USA). Coils were placed in the process chamber after tool setup. Coils were arranged around the loading chamber at the same radius to ensure same deposition thicknesses between coils in a single batch. The cMDIS parylene C dimer to polymer thickness ratio was 3.7 g of parylene C dimer to 1.9 μm of parylene C polymer, or an approximate 2:1 ratio. The dimer was brought up to 180°C and evaporated. When the parylene C dimer heats up to 600°C in a vacuum less than 1 mmHg, it becomes a monomer. The parylene C monomer then deposits into polymer form upon cooling down to 90°C under system pressures of 0.5 mmHg [104]. Sublimation, pyrolysis, and deposition, however, realize increased efficiency at even lower pressures, with polymerization typically occurring at 0.1 mmHg [105]. Although typical, this protocol was insufficient for the PCB force sensors because they required single layers as thick as 60 μm . Creating thicker layers requires additional process runs. Homogenous, uniform parylene C layers require a single process run, and secondary deposits of parylene C can introduce and/or amplify irregularities in the parylene C.

Parylene C dimer typically starts to sublime at 80-100°C. If the vaporizer was brought up to 180° C immediately, a bulk of the resulting parylene C monomer flowed by the sample, resulting in a less efficient deposition. Limiting the evaporation rate reduced the total volumetric flow of Parylene C, making for more efficient depositions. Therefore, we implemented a parylene C deposition process for this tool that could scale mass to layer thickness at a roughly 1:1 ratio. Instead of a single step to 180° C, the vaporizer was brought up to 100° C and held for ten minutes. Afterwards, the vaporizer was stepped to 110° C and held for ten minutes. This process was repeated until the final temperature of 180° C was held for ten minutes, resulting in a total of nine steps over an hour and a half. Parylene C layer thickness growth rate was noted to increase with sublimation temperature, implying that increased volumetric flow of parylene C monomer did indeed occur at 180° C versus 100° C [105]. As a result of these changes, process pressures required careful monitoring. Finally, the tool was cooled down between each run, as the dimer vaporization rate and the resultant mass-thickness ratio was dependent upon starting temperatures. Following deposition, silane adhesion efficacy was tested via a simple, qualitative sharp insertion test. A flat edge was inserted between the parylene C and substrate, and the blade was manipulated to qualitatively determine bond strength.

6.4 Coil Bonding

Parylene coated coils were bonded together using a wafer die bonder (Finetech USA, Manchester, NH). Coils were aligned using the existing alignment features in the substrate. Both coils were heated to 170° C and pressed together with 100 N of force. The coils were bonded together for 1 hour.

6.5 SEM Measurement of Deposition Thickness

The thickness of the parylene layer was verified following bonding for model validation purposes. Selected sensors were encased in a transparent resin and bisected using a dicing saw, revealing the coils sandwiching the parylene C. The samples were then hand-polished using fine sandpaper and a cloth buffer, then they were carbon coated with a Denton Vacuum BTT-IV System (Moorstown, NJ, USA) for imaging. Imaging was done using an electron microscope and wave diffraction spectroscopy tool (Cameca SX100 Electron Probe, Cameca, Madison, WI, USA) over scales of 100 to 1000 μm . Images of the parylene C layer were taken across the entire diameter of the sensor. Image J (NIH, Bethesda, MD, USA) was used in conjunction with the image reference scale to determine parylene layer thickness. The image was opened in ImageJ software. A scale was defined using the image's scale bar, and a line was drawn point-to-point between items of interest, such as traces. The drawn line was measured, and measures were taken in triplicate for each feature of interest.

6.6 SEM Imaging of Parylene Deposition Quality

Imaging was also used to assess parylene deposition quality. Parylene C deposition quality was assessed using a Zeiss 1540 EsB Scanning Electron Microscope (Zeiss, Oberkochen, Germany). Images of both a coated PCB coil from a 30 μm deposition batch and flat FR4 blank from a 50 μm deposition batch were taken over scales of 10 to 100 μm . These images were analyzed in ImageJ to quantitatively measure defects and provide insight into quality issues.

In summary, prototype coil and sensor manufacture consisted of PCB design and production, pretreatment, parylene coating, and bonding. Parylene C thickness and manufacturing quality was assessed via SEM imaging and ImageJ. Resultant measures provided intervening layer thicknesses for use in model validation, and imaging provided context for possible sources of sensor behavior prediction error due to manufacturing. Use of PCB design and manufacturing tools provided a flexible platform for passive resonator force sensor fabrication.

7. SPECIFIC AIM 2A: RESULTS

Multiple iterations of coils and sensors were manufactured for continual improvement and optimization of fabrication techniques. New approaches to coil and solid sensor manufacture were developed as a result of this iteration process. These techniques can be employed for rapid iteration and prototyping of force sensors. Quality of fabrication, however, still had a significant effect on coil and sensor behavior, introducing some challenges in accurate prediction of resonant frequencies.

7.1 Coil Manufacture and Characterization

7.1.1 First Generation Coils

The first generation of coils was produced by Sunstone Circuits (Sunstone Circuits, Mulino, OR, USA). Copper coils were fabricated on FR4 substrate. A batch of twelve boards with four designs on each was fabricated. The four designs selected for initial fabrication and validation are shown in Figure 27.

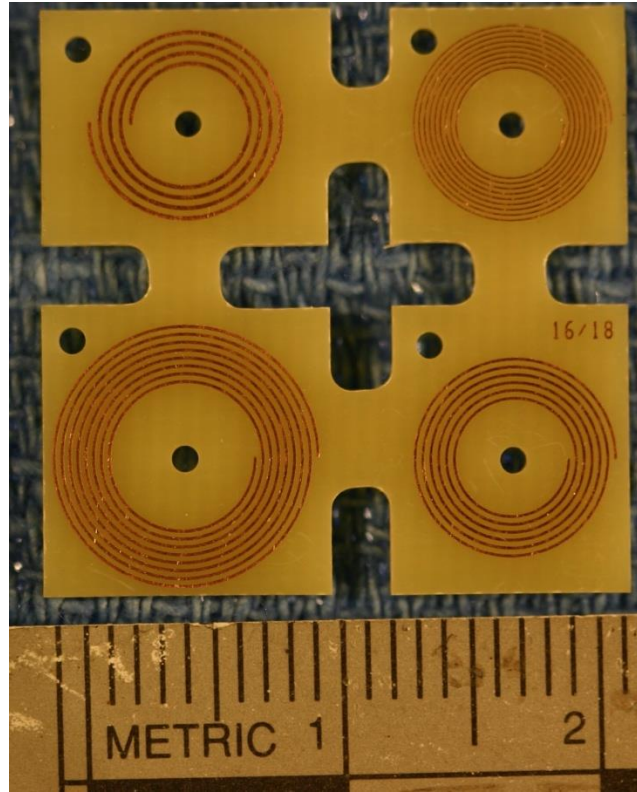


Figure 27: First generation coil designs are designated as G1D2, G1D3, G1D7, G1D8 from left to right ascending.

Upon inspection, copper defects such as scratches and indentations were visible to the naked eye. Etch quality was inspected under optical microscopy, and it was noted that some copper features failed to etch fully, altering the resultant trace width and spacing. These issues resulted in a coil failure rate of 30%. Separating individual coils from each other proved challenging due to board design, and separation potentially exacerbated feature contamination and damage. Alignment features were functional but proved challenging to utilize because they were limited to two alignment features per coil. Distances between the center hole and the “corner” hole were also different between each design.

7.1.2 Second Generation Coils

The second generation was produced by PCB Solutions (PCB Solutions, Reno, NV, USA). A batch of six boards with six designs on each was fabricated. The six designs for testing are shown in Figure 28.

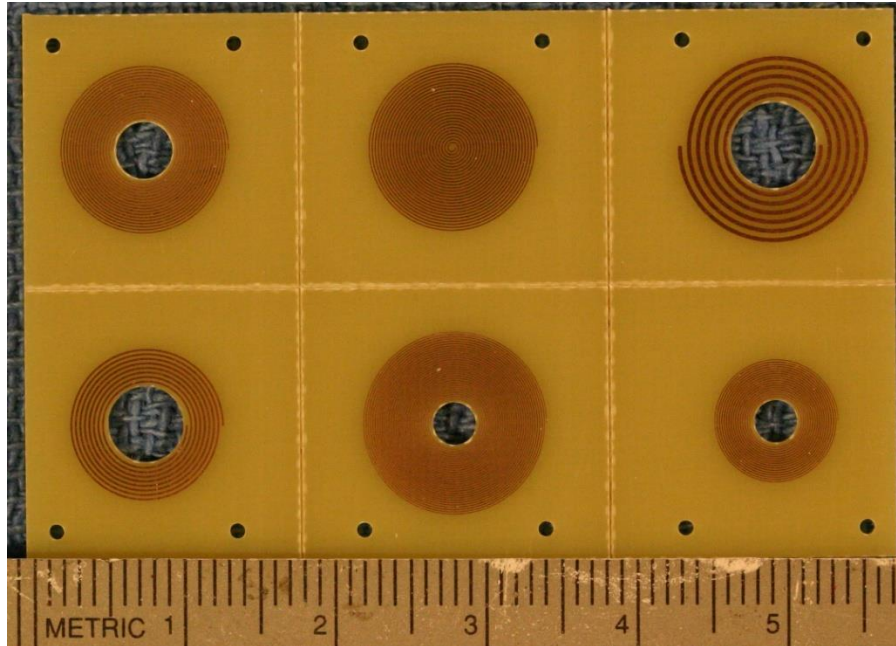


Figure 28: Going from top left to right, then bottom left to right, second-generation coils are designated as G2D3, G2D9, G2D16, G2D1, G2D7 G2D15.

Coil quality was improved, and there was no evidence of damage or incomplete etches. All coils in this batch functioned properly. Pre-drilled center holes allowed for easier adaptation to subsequent testing. Use of score lines instead of thin bridges reduced subsequent copper feature damage. Redesigned alignment holes were implemented to improve coil alignment for testing. Copper volume was reduced to lower trace height and the resultant aspect ratio of copper features.

7.1.3 Third Generation Coils

The third generation was a rerun of a single second-generation coil design for the purpose of further model validation. A batch of two boards with twenty-four coils each of one specific design was fabricated, as seen in Figure 29.

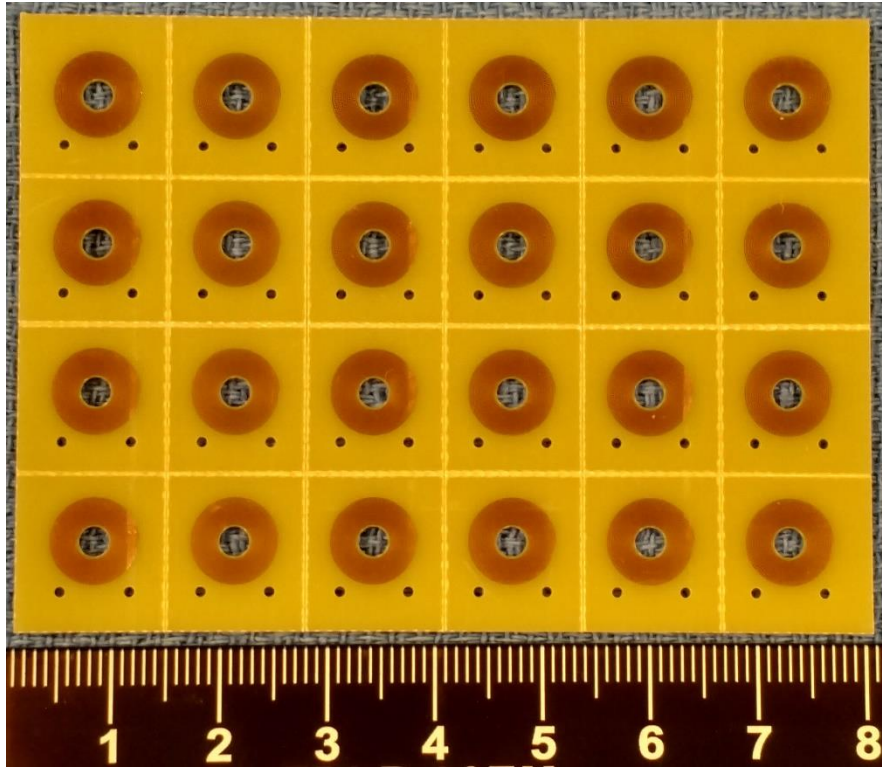


Figure 29: Third-generation coils are a singular design.

Coil substrate thickness did not vary much between the first and subsequent generations (0.77 mm vs 0.74 mm), but copper trace height did vary (32 μm vs. 18 μm). The first generation's FR4 substrate had a reported higher dielectric constant than the second and third generations at 4.4 versus 4.13 (GA vs. Isola substrates).

The second and third generation of PCB coils improved on the first for manufacturing of predrilled holes, more alignment marks, improved scoring/cuts, more consistent copper volume, improved etch, improved trace width/spacing precision, and less variation in feature geometry.

The first-generation PCB fabricated coils had issues with copper feature etching where the trace would sometimes be thicker at the base than the top, as shown in Figures 30 and 31.

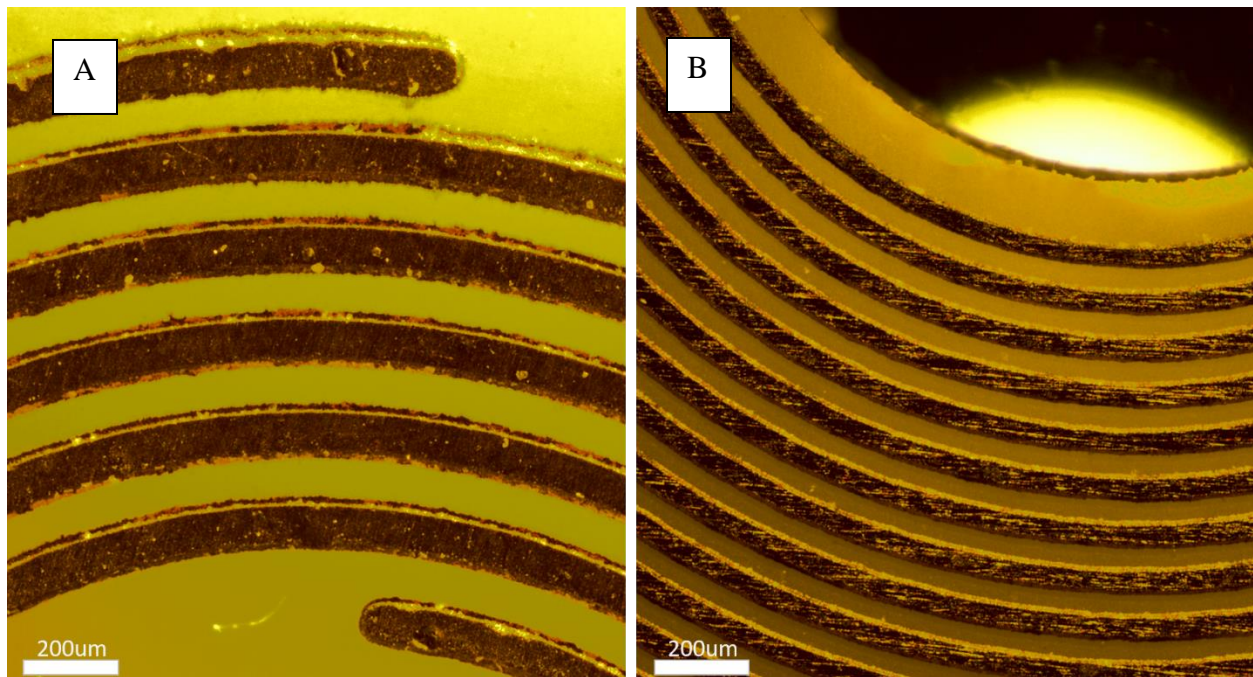


Figure 30: Image 30A shows a first-generation coil with incomplete etching on the trace base. Image 30B shows a third-generation coil with more complete etches. Both images were taken using an optical microscope.



Figure 31: Traces with orthogonal walls provide more predictable electrical behavior than traces with incomplete etch profiles.

The ideal trace has flat sides orthogonal to the substrate to allow for accurate modeling of coil and sensor electrical behavior. It is likely that the larger copper volume that was used by the manufacturer in the first generation led to more uneven etch profiles.

The second and third generation score lines improved utility over the first-generation tab designs, but board breakdown still caused issues. Breaking the coils apart via score lines caused minor delamination and uplift near the substrate edges, potentially making the affected coil susceptible to non-parallelism in sensor fabrication.

7.2 Coil Preparation for Parylene Deposition

Coils treated with silane exhibited no visible difference from uncoated coils before deposition of parylene C. There was no change in parylene C deposition quality or thickness. A qualitative sharp insertion test was done to evaluate the bond strength of untreated versus A-174 treated surfaces. Parylene C easily delaminated from untreated surfaces while there was little to no success in delaminating A-174 treated surfaces via sharp edge test. Figure 32 shows parylene C delamination on an untreated FR4 substrate.



Figure 32: Untreated substrates coated with parylene C easily delaminates when a sharp edge is inserted between the substrate and parylene C. The lighter colors near the corners indicate delaminated parylene C.

Bonding the parylene C to the FR4 substrate via silane ensured stress-induced delamination did not occur. The intervening material laterally strained under axial compression. Using Hooke's law and known poisson's ratio, compressive modulus, and stresses, calculations showed that under a 500 N axial load, 0.18% lateral strains occur in third generation sensors, which would result in sub-micron strains that would not be large enough to disrupt the bonds between the parylene and FR4 substrate. A potential mode of failure is any potential off-axis load-induced strains that could cause the sensor to fail via delamination. Implementing the silane adhesion promoter reduces the likelihood of any load related failure, as well as increase sensor robustness during handling and transport.

7.3 Parylene Deposition

Parylene C coated coils had a white, uniform, translucent film, as shown in Figure 33, with the opacity dependent upon layer thickness.

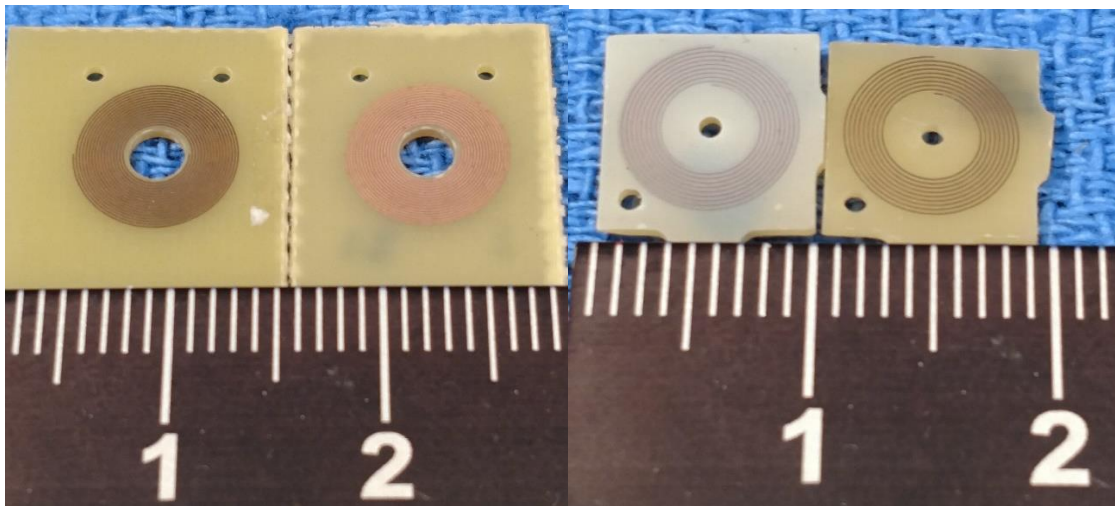


Figure 33: Coated coils had noticeably lighter coloration, and the copper traces lost their luster. Thicker layers were more opaque and lighter in coloration.

Using the standard deposition protocol for the Union Carbide 1050 parylene deposition system with high starting dimer masses occasionally led to variation in deposition thickness, as seen in Figure 34.

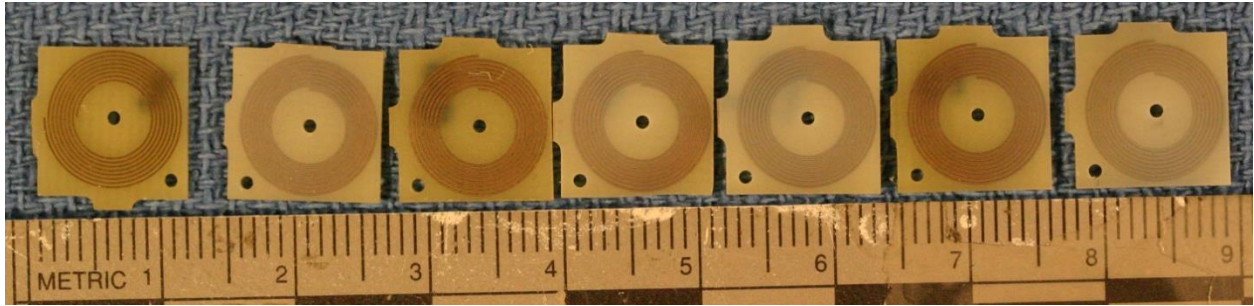


Figure 34: These coils were all done in the same parylene deposition run, yet they clearly exhibit different parylene layer thicknesses. Uneven depositions were apparent within coils.

Profilometry was used to further verify that initial deposition attempts resulted in uneven surfaces. A Dektak 6M Stylus Profiler (Veeco, Plainview, NY, USA) was used to measure surface profiles of the coated coils. Figure 35 shows an example of a coil's non-parallel deposition surface.

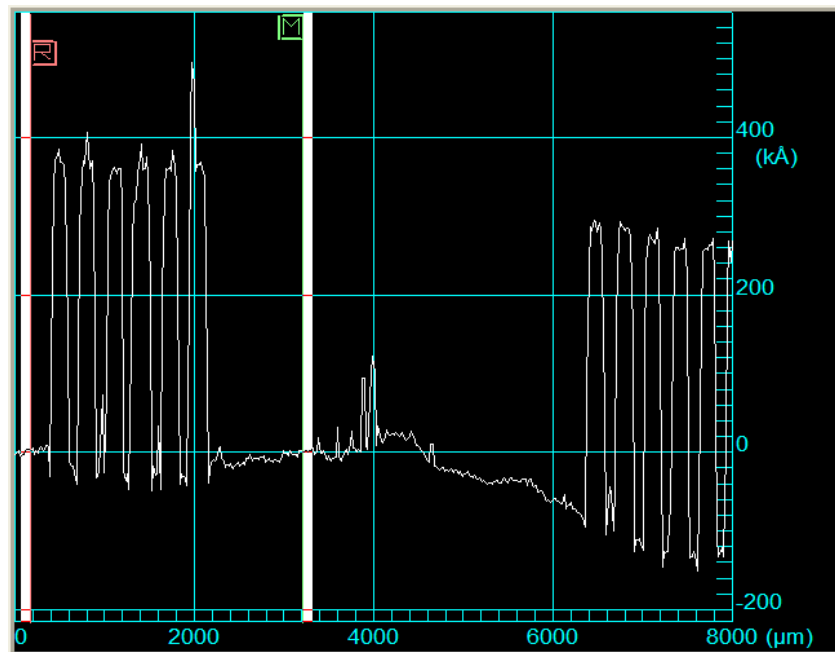


Figure 35: Profilometry scans of a coated coil showed uneven Parylene C deposition. Note the decrease in average trace height as well as general drop off towards the right side of the coil diameter.

An average of 2-5 μm variation occurred from one side to the other.

The deposition protocol was then changed to achieve thicker, uniform parylene depositions. In order to limit defects resulting from higher starting masses, it was critical to ensure the tool's chamber seal was clear of deposited polymer, whose buildup can be shown in Figure 36.

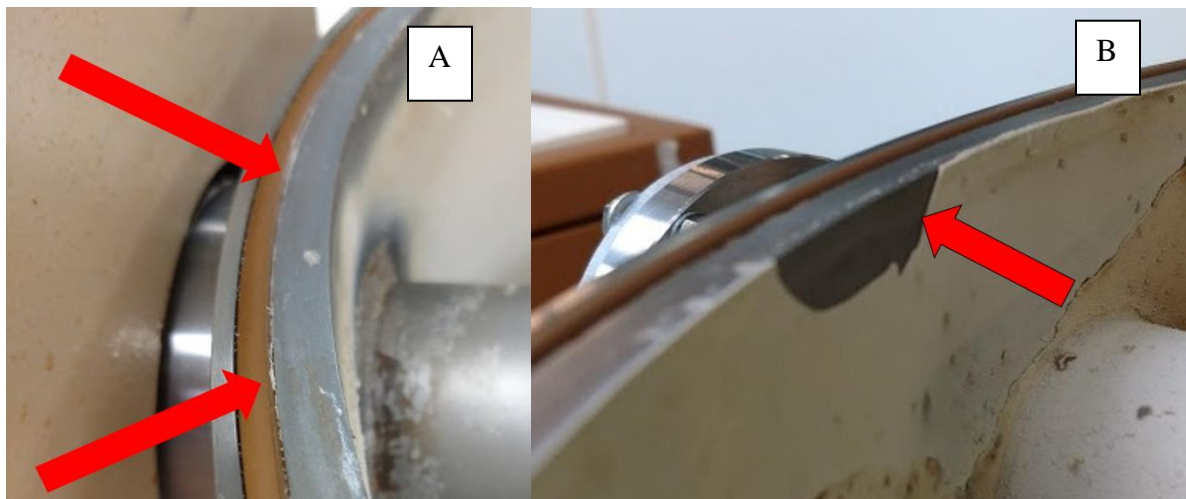


Figure 36: The red arrows in 36A indicate encroaching parylene on the chamber seal itself. The red arrow in 36B indicates the solid polymer buildup along the chamber wall.

The deposited polymer compromised the tool's efficacy by building up on the chamber seal over time. Keeping this seal and the nitrogen trap on the tool clear ensured that the process pressure stayed below the required 180 mTorr threshold, even with a large starting dimer mass. Additionally, coils were set up in roughly the same radial distance from the center of the chamber stage, as seen in Figure 37, to limit the effects of deposition variation within batches.



Figure 37: Coils were placed roughly at the same radius from the center of the platform for consistent deposition for each batch.

Barrel micrometers and profilometry were used to confirm desired layer thicknesses and uniformity, with final, accurate layer thickness validation done later via SEM. Non-parallelism in thick parylene C films was reduced following changes to the tool's deposition protocol.

The non-parallel deposition using the in-house protocol was likely due to the speed of parylene dimer vaporization and deposition in conjunction with the large dimer mass. Even deposition across each coil in each batch was important for consistency, as consistent sensors were key for model validation. Ideally, multiple depositions are done for each sensor batch, but each deposition is time and resource intensive, which is not conducive to rapid prototyping of PCB force sensors.

7.4 Sensor Bonding

Coil alignment was done using the tool's built-in microscope with video feed. The coil itself was moved via a high precision three-axis tray. Center holes were first aligned, then the tray was rotated and shifted until the 1mm corner alignment holes overlapped.

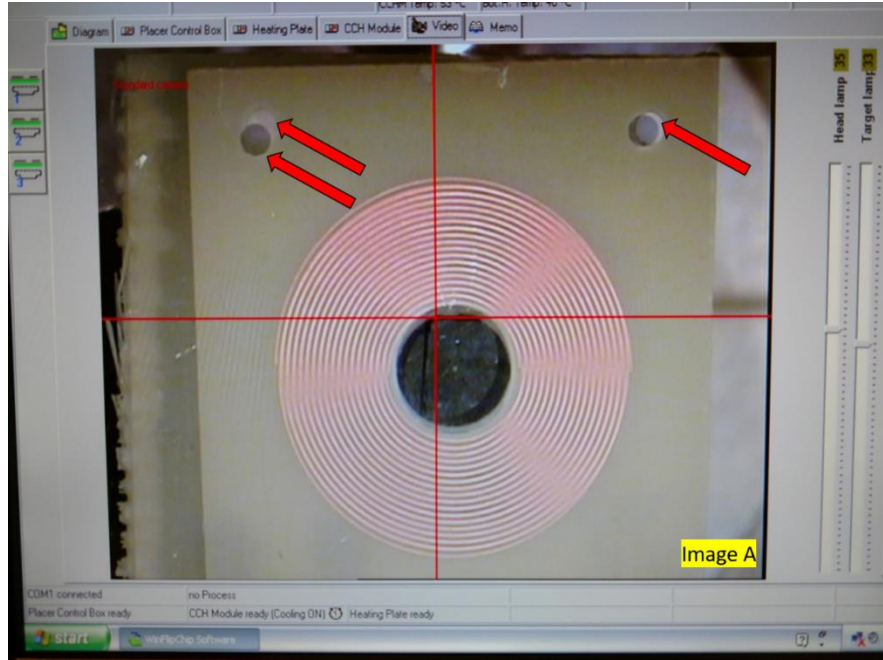


Figure 38: Camera-assisted alignment was used in the die bonder for accurate alignment of coils. The screen shows a coil close to alignment, as indicated by the red arrows. A perfect overlap would show no overlap in alignment holes.

Figure 39 shows a completed, bonded PCB sensor.

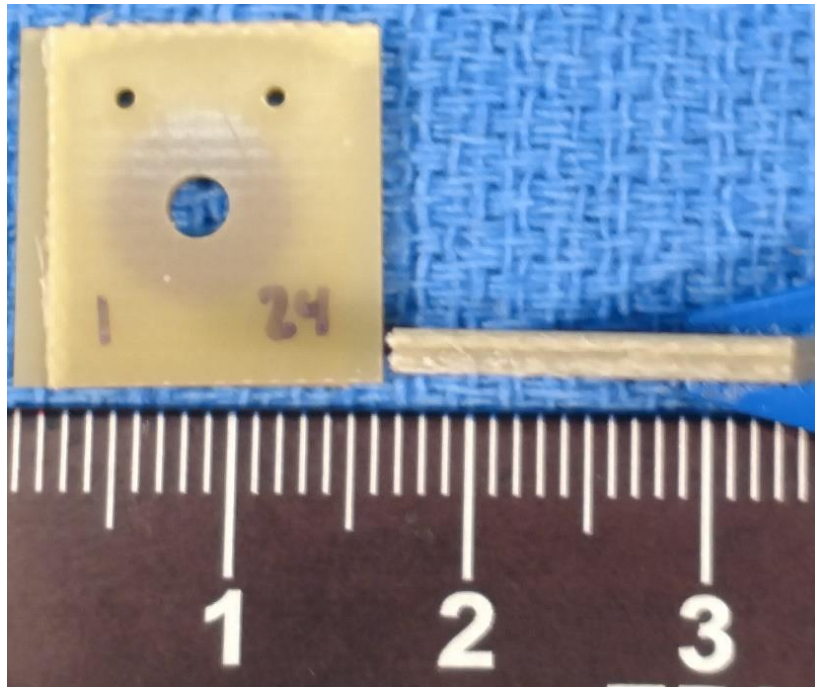


Figure 39: This axial and transverse view of a completed PCB sensor shows successful bonding.

Mis-aligned coils were the largest source of erroneous sensor behavior. The alignment tools and features, however, proved effective, as there was little variation in sensor resonance between sensors with identical geometries. Process temperatures of 170°C were used so that the parylene could sufficiently bond between the FR4 substrate. Without damaging the FR4, parylene C polymer's glass transition temperature of 110°C could be achieved, which is conducive to entanglement between two separate parylene films [96]. The substrate's response to bonding was also observed, and the 170°C process temperature was determined to be suitable based on the first-generation substrate's lower glass transition temperature of 175°C . Additionally, exceeding 170°C causes parylene to oxidatively degrade, causing unpredictable heating throughout the film [106].

7.5 Thickness Measurement

Initially, parylene deposition thickness was measured via the profilometer. To serve as references, several blank FR4 sections were included with each coil batch. After deposition, a section of the parylene was cut away from the surface of the blanks. The profilometer was then used to measure the height difference between the uncoated FR4 surface and the deposited parylene C polymer, as seen in Figure 40.

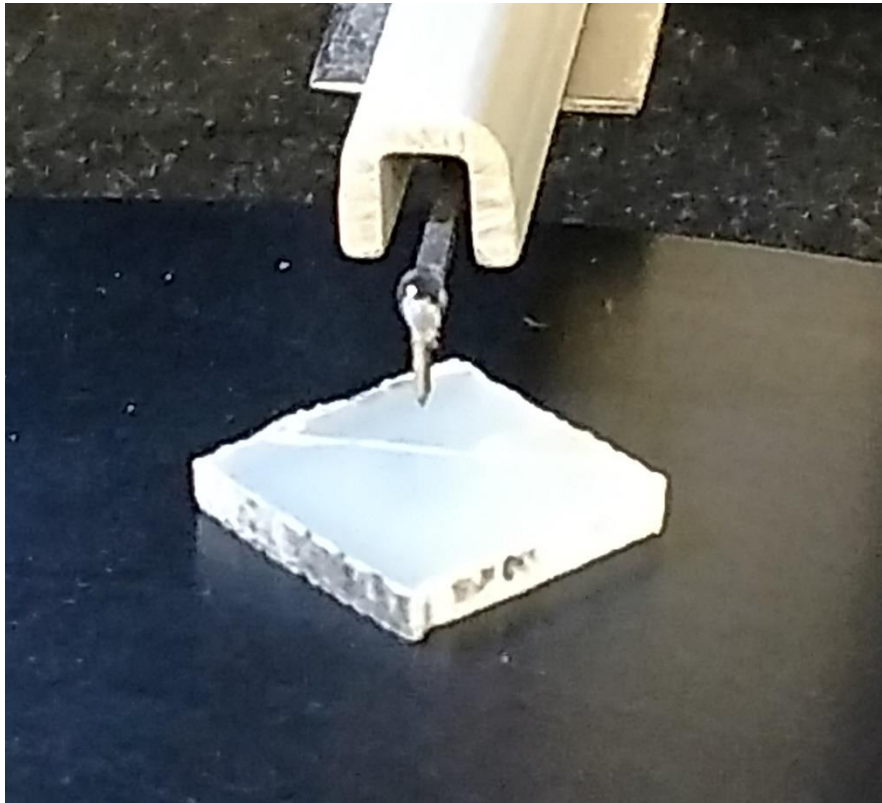


Figure 40: FR4 blanks were coated alongside coils. Films were partially cut, and a profilometer measured parylene C thickness by measuring the height difference between the parylene C and the underlying substrate.

This method was found to be inconsistent by comparing data with measurements from a barrel micrometer and from scanning electron microscope (SEM) imaging. Additionally, this method was challenging due to the difficulty of separating the parylene C from the substrate after silane

adhesion. Results were likely skewed due to layer delamination and gouges in the original substrate.

Using SEM, initial images and measurements of bisected sensors revealed successful bonding of the two coils with evidence of parylene C reflow. Figure 41 shows the array of sensors sacrificed and cast for parylene layer cross section imaging.

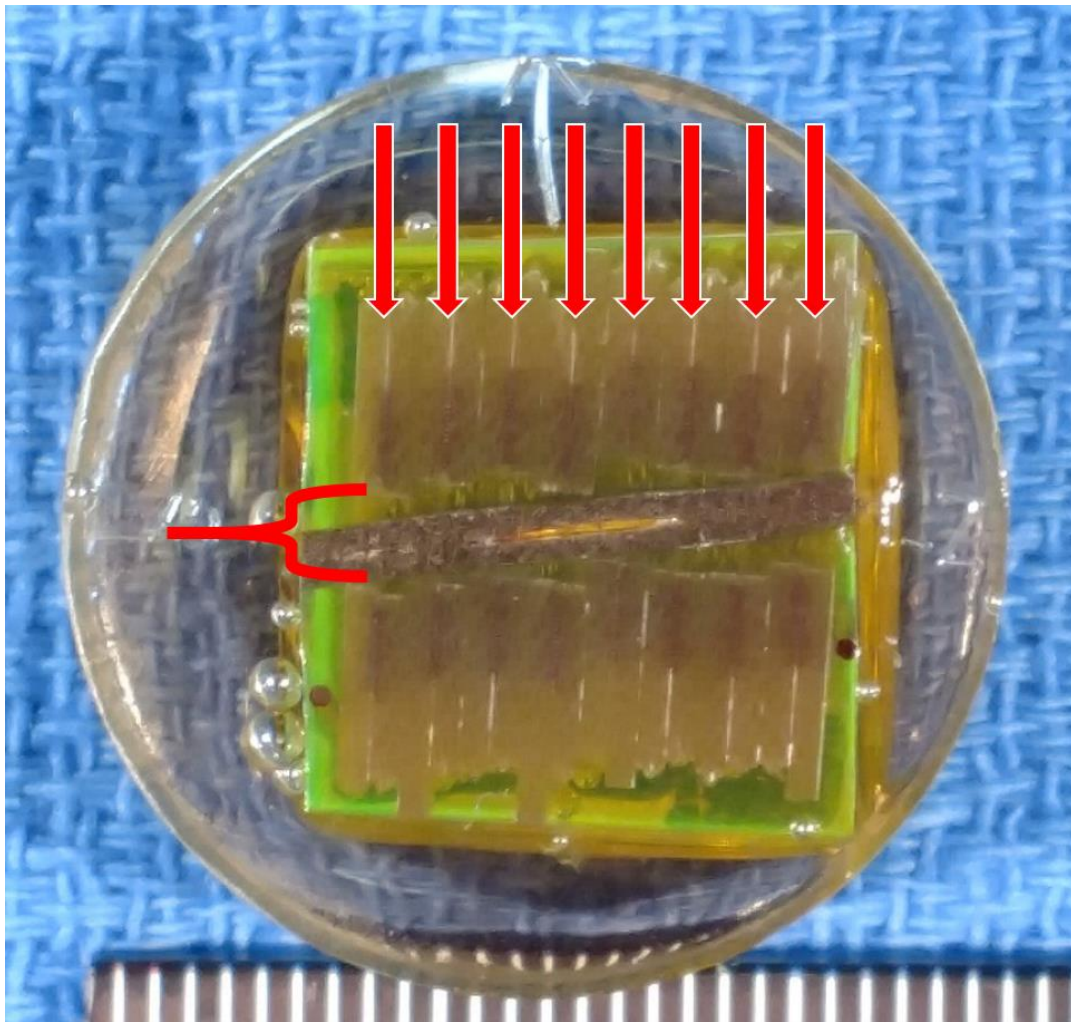


Figure 41: A stack of sensors was cast in resin and bisected for SEM imaging and variable thickness model validation. The red arrows indicate each of the eight sacrificed, bisected sensors in this resin cast. The red bracket indicates the inner diameter of the coils secured by a metal post.

Figure 42 shows a cross-sectional view of a solid force sensor using SEM.

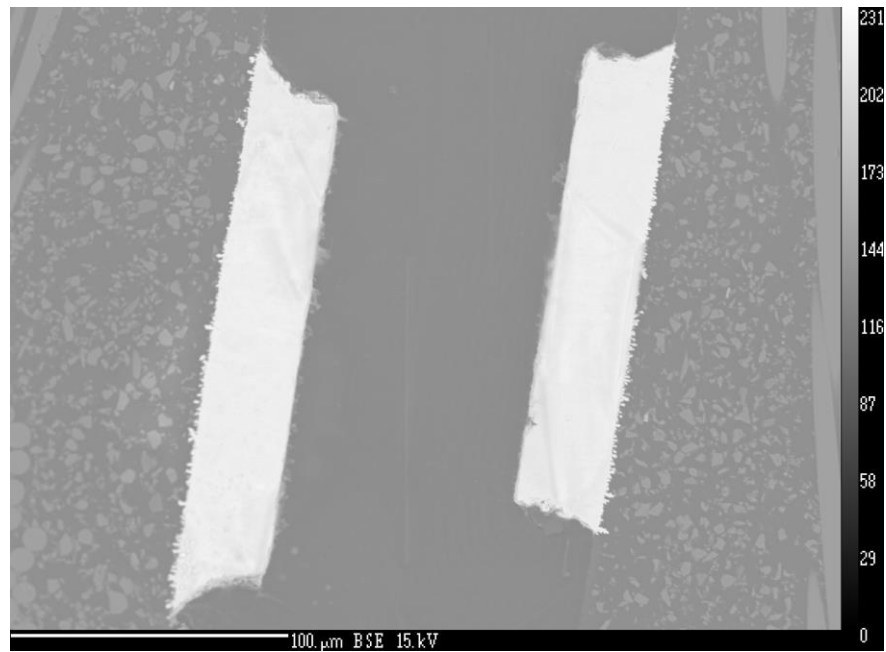


Figure 42: Bisected solid sensors were SEM imaged to assess intervening layer thickness and deposition quality. This SEM image shows a bisected parylene C force sensor's overlapping traces.

These images were taken for each sensor and measured using ImageJ. The following table shows the array of bisected sensors that were measured via SEM along with their starting dimer mass.

Table 10: SEM measured thicknesses and their respective input dimer masses. *Indicates sensor is product of two deposition runs.

Sensor	Measured Thickness (um)	Input Dimer Mass (g)
G3_3	169.13	29.9+25.63*
G3_1_2	166.84	51.26
G3_20	150.16	46.99
G2_3_6	105.75	38.45
G3_15	98.26	34.18
G3_4	91.97	34.18
G2_4_5	75.84	34.18
G3_17	74.29	29.90
G3_12	49.78	25.63
G3_7_8	23.62	12.82

Due to the aspect ratio of the coil trace, deposition is not perfectly uniform. Figure 43 shows the deposition profile on a first-generation sensor that shows the deposited parylene C “wrapping” around the copper traces.

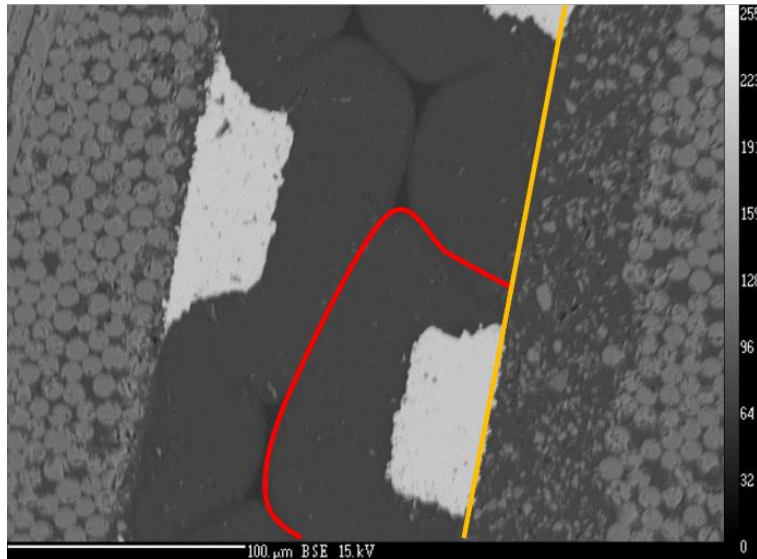


Figure 43: Another SEM image of a bisected solid sensor's traces shows the non-uniform profile of the annealed parylene C layers as indicated by the red line. Trace aspect ratio reduces deposition uniformity. Uneven trace etches are also exemplified in this image.

ImageJ measurements of bisected sensors showed that the single layer parylene thicknesses ranged from 20 to 57 μm for all sensors, confirming that thick parylene C deposition thicknesses were controllable via starting dimer mass and the modified deposition protocol. Parylene height between spaces are larger than heights between traces due to reflow. Parylene annealing in the die bonder induced height loss due to reflow. Height loss ranged from 1 to 24.34 μm with the highest height loss due to reflow occurring in a set of sensors baked for a longer two-hour duration. Generally, annealing results in a height loss of 0.5-12 μm per hour, depending on geometry, substrate thickness, substrate thermal properties, parylene thickness, and annealing time. This contraction is typical [105]. Coils with larger substrate areas have more heat dissipation, resulting in less reflow and height loss. Two different coil designs from the same batch, G1D7 and G2D9, were examined. The smaller G1D7 coil had a smaller area and exhibited more height loss compared to the larger

G2D9 coil. Bond uniformity is a common problem in annealing parylene C layers together. Increased reflow reduces these non-uniformities [96].

7.6 Parylene C Deposition Quality

The coated coils were imaged also to assess the quality of parylene deposition. Thick coil depositions greater than 50 μm led to unexpected sensor behavior. Deposition quality concerns arose when process pressures rose above a 180 mTorr threshold. Complete parylene C polymerization fails to occur above this pressure. The tool was loaded with 47 g of parylene C dimer, and the tool pumped down to standard pre-operating pressures of ~ 120 mTorr. After starting the process, the pressure rose above 180 mTorr several times, which hindered uniform parylene C polymer formation [107]. The FR4 blank sample was part of the thick parylene deposition batch exceeding 50 μm , and the coil sample was part of a thinner parylene deposition batch of ~ 20 μm .

Initial analyses of the SEM images showed that both the coil and FR4 blank samples exhibited defects in the form of “boulders” and non-uniformities. These defects could have been the result of two things: Pre-existing contaminants resulting from manufacturing, processing, handling, or imperfect process techniques. Insufficient pressures or temperatures could result in deposition of unreacted parylene, leading to non-uniformities.

These defects likely were a result from the latter imperfect process techniques, as there was a significant difference between the thin parylene coated sample and the thick parylene coated sample. These two samples were produced in two different deposition batches with different intended deposition thicknesses. Both samples were imaged at 300x magnification, and the blank from the 50 μm deposition batch has a much less uniform profile than the coil from the thinner 21 μm batch, as seen in Figure 44.

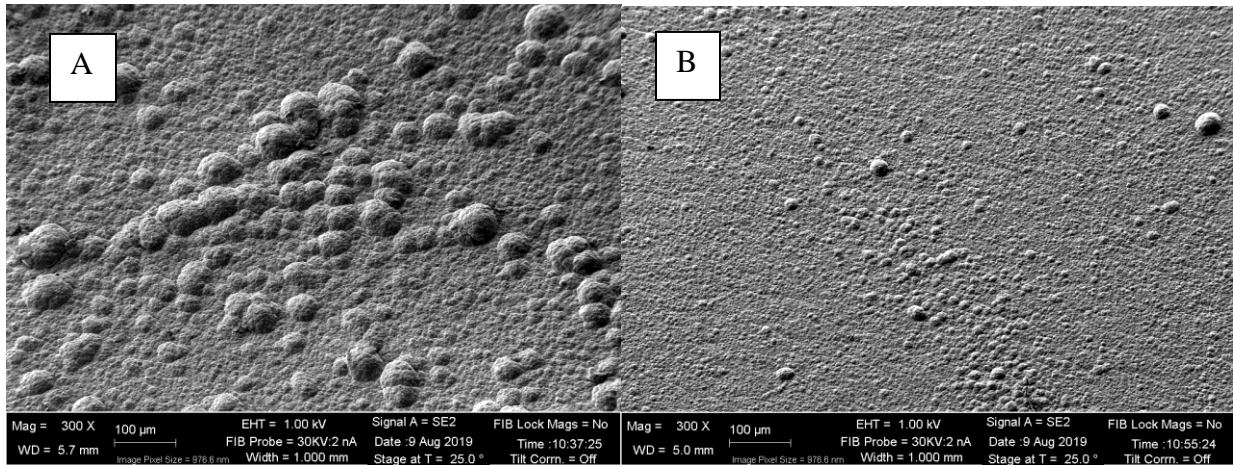


Figure 44: The thick parylene sample in image 44A has large defects compared to the thin parylene sample in image 44B. Both were taken at the same magnification.

Additionally, the height of the non-uniform features varied more in the 50 μm batch than the 21 μm batch. Some of the boulders were as tall as 30 μm , which was a significant portion of the parylene thickness, as seen in Figure 45.

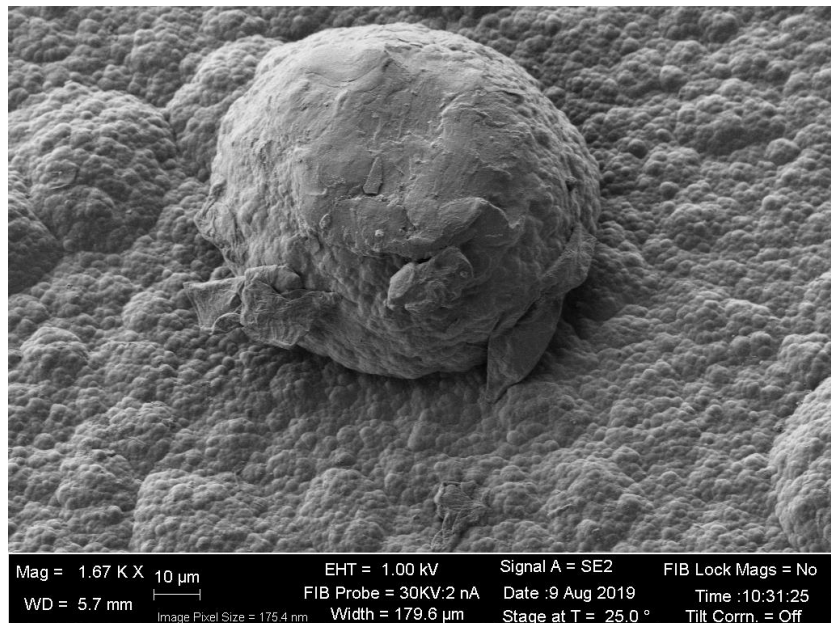


Figure 45: This SEM image shows a “boulder” defect on the surface of the thick parylene sample.

The defects in the 50 μm batch were also not as “integrated” in the parylene polymer layer as the defects in the 21 μm batch, as seen in the comparison between samples in Figure 45.

These defects likely contributed to the thicker sensors’ inconsistent resonant behavior. The non-uniformities may have increased final sensor resonant frequency by further separating the coils from each other. Air gaps, like those found in Figure 46, also formed during bonding due to the non-uniformities, which can be significant enough to alter the relative dielectric constant of the sensor stack and the resultant electrical behavior of the sensor.

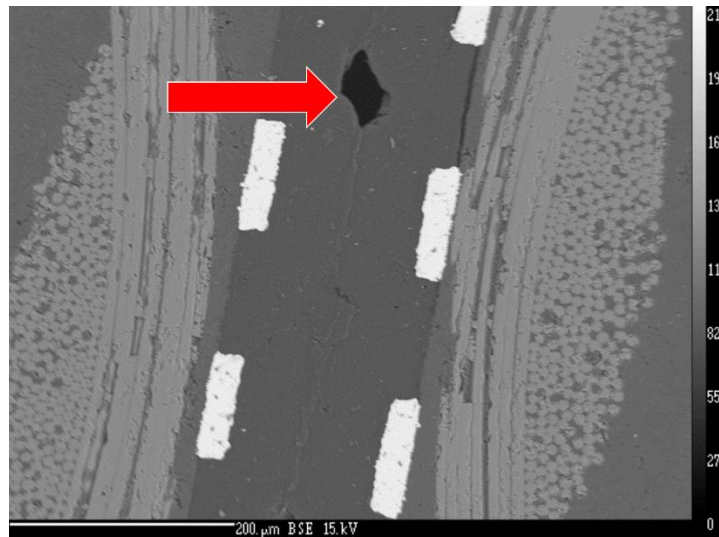


Figure 46: The arrow indicates an example of voids, or “air gaps”, that formed during sensor bonding due to copper trace aspect ratio and layer non-uniformities.

Additionally, imaging of the coil traces from this perspective validated the assumption that the trace and space areas increased and decreased, respectively, after deposition. See figure 47 for examples of this change.

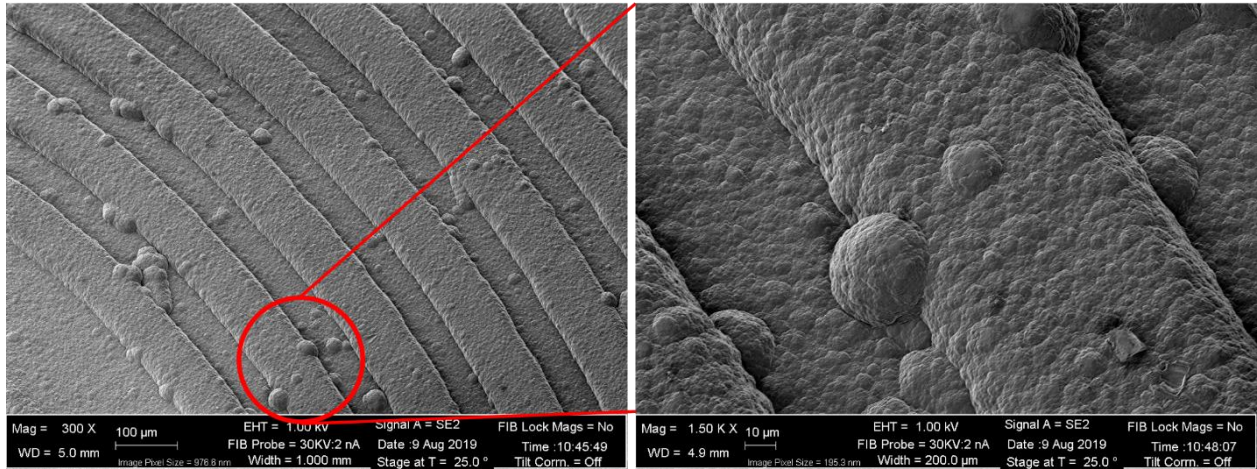


Figure 47: The pictured coil's original copper trace width and space underneath the parylene are each $\sim 75 \mu\text{m}$.

Higher deposition pressures can also lead to a lower Young's modulus for parylene C, further confounding force sensor behavior predictions [98].

7.7 Challenges in Sensor Manufacturing Quality

Thickness measurements showed variations in thickness from one side of a sensor to the other, revealing that coils were non-parallel with some cases being more severe than others. Table 11 shows SEM thickness measures taken at three points across the cross section of each sensor. Two measurements were taken at the edges, and the third was taken in the center.

Table 11: SEM measured parylene C thicknesses across their entire diameter.

Sensor	Bot (μm)	Mid (μm)	Top (μm)	Mean (μm)	Std Dev (μm)
G3D15_3	169.70	169.21	168.48	169.13	0.61
G3D15_1_2	167.22	165.77	167.53	166.84	0.94
G3D15_20	149.66	149.86	150.97	150.16	0.71
G2D15_3_6	116.83	106.87	93.54	105.75	11.69
G3D15_15	96.85	95.63	102.3	98.26	3.55
G3D15_4	88.26	92.42	95.25	91.97	3.52
G2D15_4_5	95.36	69.21	62.96	75.84	17.19
G3D15_17	64.59	71.82	86.45	74.29	11.14
G3D15_12	48.38	48.81	52.16	49.78	2.07
G3D15_7_8	28.59	20.9	21.36	23.62	4.31

Sensor G2D15_4_5 represented an extreme example of non-parallelism with a 17.2 μm standard deviation, which was significant compared to the average thickness of 75.84 μm . The average thickness was still representative of the batch deposition thickness, but non-parallel coils could lead to measured sensor resonances that were significantly different from modeled predictions. It is unclear how much non-parallelism can affect expected resonant behavior, but the analytical model assumes coils are always parallel to each other, thus introducing a potential source of error.

The most likely cause of this non-parallelism was the die bonder tool and coil design. As part of alignment, a vacuum holds one coil on a vertical heating element. The coil's predrilled holes limit where the coil could be positioned on the heating element, so the top heating element was challenging to center. Additionally, the top heating element was typically slightly smaller in area than the coils being bonded. The resulting 100 N load was slightly off-center when the coils

were brought together. Substrate uniformity plays a large role in parylene C bonding quality. Even with featureless silicon wafers, surface non-uniformities can lead to imperfect parylene-parylene interfaces.

The aspect ratio of the copper traces introduced some challenges to modeling the behavior of these PCB parylene C sensors. Aspect ratio refers to the ratio of copper trace height to copper trace width. Parylene C vapor deposition is conformal, meaning that it evenly covers all surfaces on a coil. Issues with aspect ratio arose during bonding and mechanical loading. A smaller aspect ratio reduced the formation of air gaps that can form due to bonding. Conversely, a larger aspect ratio decreased deposition uniformity, introducing defects. Parylene C reflow during annealing was also greater due to increased heights, further changing the actual thickness from the expected thickness. Furthermore, SEM imaging revealed that increasingly thinner parylene C depositions reduced the formation of air gaps, while decreasingly thicker depositions increase the volume of these air gaps. These changing deposition thicknesses and resultant air gap volumes introduced further electrical effects that confounded analytical modeling.

Unfortunately, the aspect ratio problem was unavoidable with fast, inexpensive PCB coil prototyping. Manufacturers typically dictate feature height via the volume of copper used in a board. Minimum volumes in conjunction with smart board design may reduce total copper feature height, but it is incomparable to microfabricated coils, whose heights are controllable and resultant aspect ratios are negligible for electrical and mechanical considerations. The problems resulting from PCB aspect ratios could be minimized using improved bonding protocols. Bonding under vacuum would eliminate the electrical impact of air gaps on sensor resonance, making their behavior more predictable. Additionally, longer bonding protocols would increase the amount of

reflow, further reducing the size and impact of air gaps. However, longer bonding protocols may deform the FR4 substrates.

Manufacturing methods were iterated to improve the capability of rapid prototyping of force sensors. The methods for prototyping PCB based coils can also be applied to other wireless, passive resonant sensor applications for rapid production, testing, and validation. The parylene C deposition protocol was modified to allow for thick depositions of parylene C greater than the 7-8 μm coatings typically found in electrical and biomedical applications. These changes allowed for rapid production of multiple force sensor designs for smart cervical spine implants.

8. SPECIFIC AIM 2B: EXPERIMENTAL PROTOCOL

8.1 Coil Characterization

Coil characterization was a critical first step in validating the force sensor model. In order to confirm that the coils were intact and functioning properly prior to force sensor fabrication, the following techniques were employed: The boards were inspected for damage from manufacturing and handling. An optical microscope was used to assess each coil in a board for shorts between traces, discontinuity in traces, etch quality, and contamination. Coils were measured with calipers to roughly verify trace width (Tw), trace spacing (Ts), outer diameter (OD), and inner diameter (ID). These dimensions were also measured with a Dektak 6M Stylus Profiler (Veeco, Plainview, NY, USA). A coil was placed under the profiler's stylus, and the stylus was moved across the coil, tracing the coil's features. This profile could be used to determine OD, ID, Tw, Ts, and trace height (Th). Substrate thickness was verified using a barrel micrometer. These processes were repeated three times for each coil. These measured parameters were used in the model for coil and sensor behavior validation. The coils on each board were labelled to indicate their position and board they originate from. The coils were then separated. For first generation coils, a dremel was used to separate the coils. Subsequent generations had perforations in the board to enable coils separation by hand.

8.1.1 Measuring Resonant Frequency

Each coil was placed above a custom, 18 gauge solid-core wire loop antenna connected to an E5062A network analyzer (Agilent Technologies, Santa Clara, CA, USA), as seen in Figure 48.

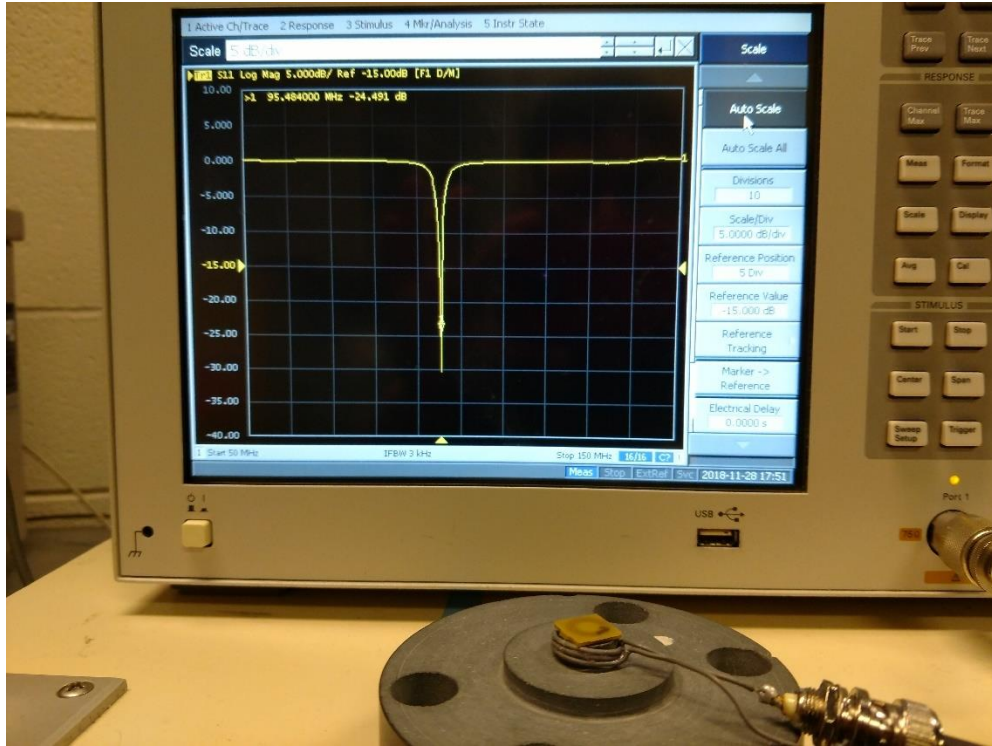


Figure 48: Arrangement of antenna and NA for coil resonance characterization.

The bandwidth on the network analyzer was set to ± 50 MHz of the expected resonant frequency. Polling rate was set at 501 samples per second. Minimum peaks were continually tracked. Once the resonant peak was located, the bandwidth was set to ± 5 MHz, and the resonant frequency and absorption (-dB) was recorded. This process was repeated three times for each coil, and the average was recorded. The average measured resonant frequency was compared to the modeled resonant frequency after the respective measured geometric parameters were input. The entire measured spectrum was captured and saved into a .csv at preset intervals. Following the test, resonant peaks were extracted from multiple .csv files via MATLAB (Mathworks, Natick, MA, USA) to generate plots of time-based resonant behavior.

8.1.2 Measuring Coil L and C

Measurements of coil electrical properties were critical for model validation, as direct correlations between geometric properties and the coil L and C could be drawn. There were efforts to measure the inductance and capacitance directly. Generally, LCR meters can measure inductance and capacitance of a system, but in the case of the coils, the inductance and capacitance readings either fluctuated significantly or read a short. The U1732C (Agilent Technologies, Santa Clara, CA USA) is purported to read inductances as low as 0.001 μH in a 20 μH range, which falls well within the expected range of the coils' inductances. However, LCR meters measure component impedance and calculate resultant inductances and capacitances. If the impedance, or the resistance plus reactance

$$Z = R + jX \tag{28}$$

of the device is too low, the device simply reports it as a short. It is possible to determine L and C from low impedances, but the measuring device was not able to measure impedances at a high frequency. Reactance is frequency dependent. An increase in circuit frequency increases reactance, which subsequently increases the total measurable impedance. The device was limited at 10 kHz, and in order to measure the low resistance coils, it needed to be able to measure in the megahertz range.

The suggested approach for measuring coil inductance and capacitance was to use a dedicated, high frequency impedance analyzer. Ultimately, it was decided that it would be simpler to extract the inductance and capacitance via measured resonant frequencies.

8.2 Test Setup

The experimental protocol was established to ensure that mechanical measurements of sensor behavior were accurate and repeatable. Air sensors required consistent alignment for each pair, as well as consistent displacement steps. Solid sensors required accurate measurement of deformations and applied loads.

8.2.1 Coil and Antenna Setup

Alumina silicate, a compound consisting of variable amounts of alumina and silicon dioxide, is machinable and has a high dielectric constant of >5.8 , which reduces unwanted resonant peak shifts when polling a coil or sensor with an antenna. This material has a high modulus of 110-170 GPa depending on composition, so it withstands high loads with little to no deformation [108]. Alumina silicate fixtures were used to support coil and sensor measurement in testing. Fixtures were necessary to facilitate continuous frequency measurement during displacement and loading. The fixture was machined such that the antenna rested below the coil or sensor during testing, as seen in Figure 49.



Figure 49: The machined AlSi fixture allows for continuous monitoring of coils and sensors during testing.

The fixture was also machined to custom fit our mechanical test system via four polyethylene screws, as adjacent metal interferes with resonant readings.

Alignment features were tooled into the fixtures, allowing for accurate alignment of two separate coils. Figure 50 shows the central and “corner” alignment holes with posts temporarily installed to ensure that the inferior and superior coils were aligned to each other via the fixtures.

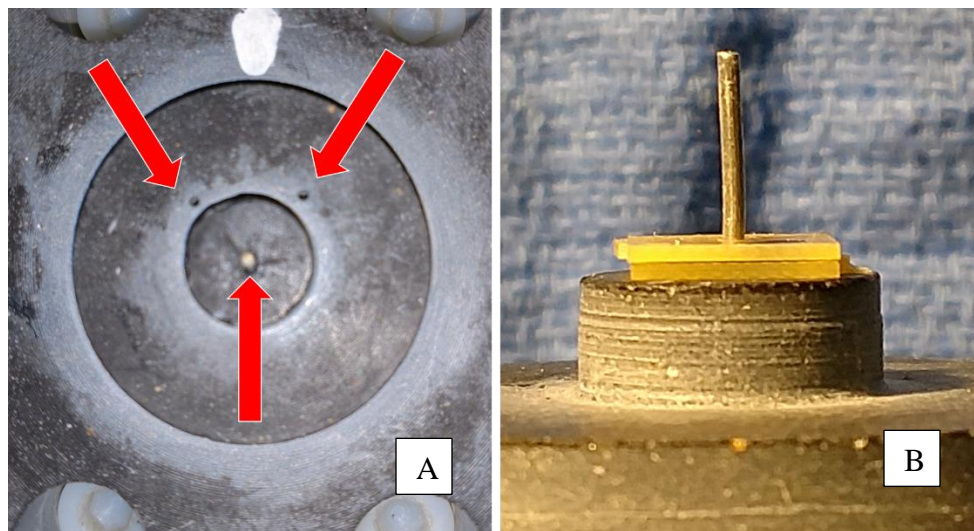


Figure 50: Figure 50A shows drilled alignment holes for posts to rest in. Figure 50B shows an example of aligned coils for air testing. Superior fixture not shown for clarity.

Fixtures also featured scoring to prevent extensometer slippage during actuation.

8.2.2 MTS and Extensometer Setup

The mechanical testing system, MTS 2/G (MTS, Eden Prairie, MN, USA), was programmed to perform a series of tasks through a graphical programming interface.

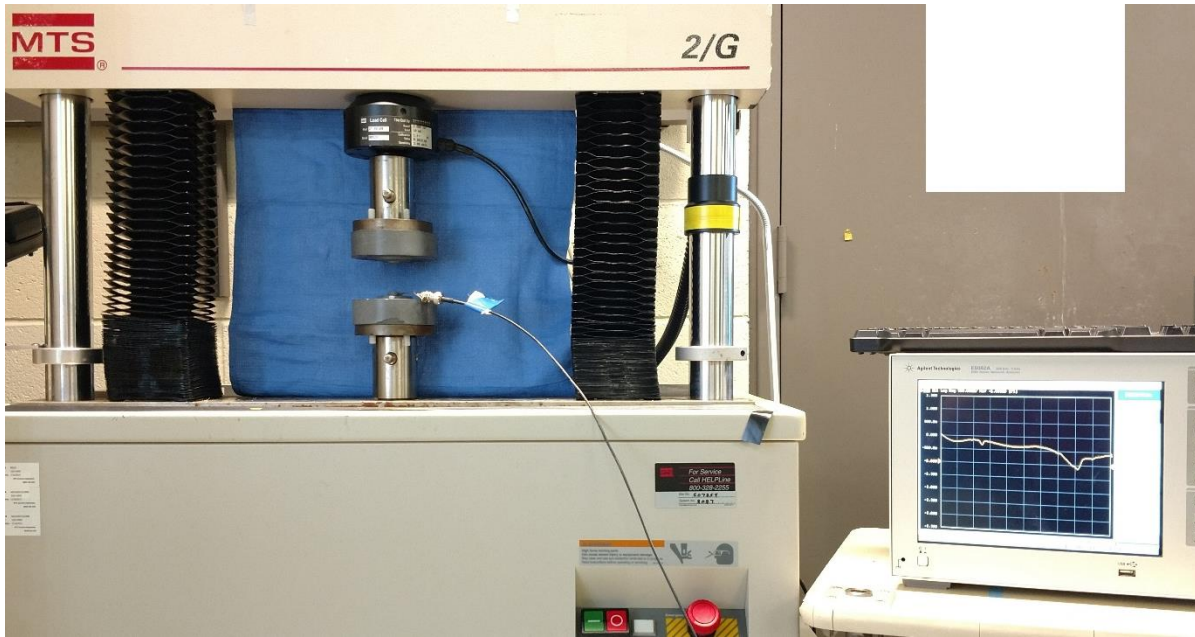


Figure 51: An MTS 2/G configured for sensor compression testing has custom fixtures, an antenna, and a network analyzer for sensor measurement.

The MTS measured force and total crosshead displacement, providing the means to consistently test sensors for validation of the force sensor model. The transducer is rated to 10 kN with a resolution of a hundredth of a Newton, dependent upon calibration. The displacement resolution of the MTS 2/G is 0.6 μm . Data was acquired at a programmed rate and output into a .csv file.

The MTS extensometer (MTS, Eden Prairie, MN, USA), required extra set up to use with the MTS, but it provided a significantly more accurate, external means of measuring displacement. The extensometer was used to check against the reported crosshead displacement in small displacement situations as a safeguard against inertia based or crosshead “free-play” based inaccuracies present in the MTS.

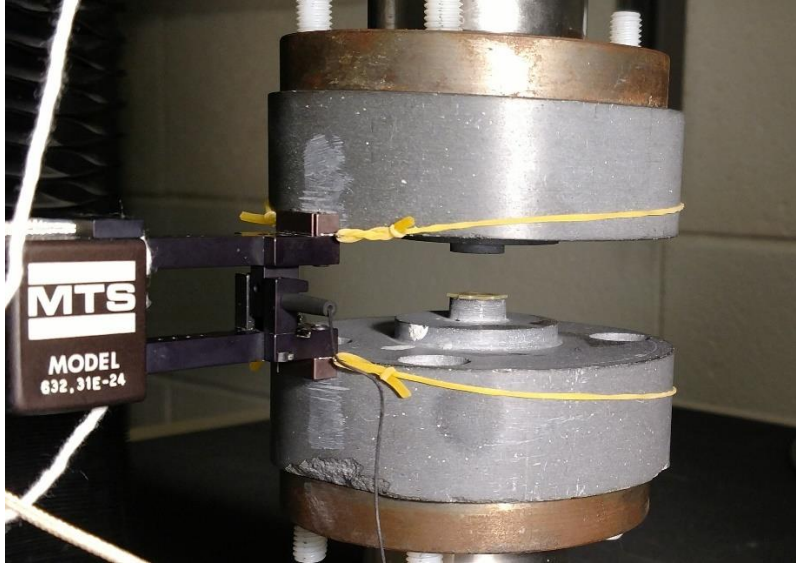


Figure 52: An MTS extensometer was attached to the fixtures via knife-blades and secured with rubber bands for improved displacement readings.

The extensometer has a 5 mm tensile displacement range and 2.5 mm compressive displacement range for a total of 7.5 mm, limiting it to small displacement situations unless otherwise modified. This permits the extensometer to maintain a high sensitivity and resolution required for the micron and submicron level strains present in the parylene C force sensors. Additionally, the extensometer can be calibrated to be more accurate within a specific displacement range.

Extensometer setup involved moving the crosshead until the coils or fixtures were within 50 μm of each other. The extensometer was then attached to the fixtures via rubber bands, and the knife edges on the extensometer plus the scored fixtures ensured that the extensometer did not slip during displacement measurement. The data was output to the program where it was then read and saved normally.

8.3 Air Gap Displacement Protocol

“Air gap” sensors (sensors with air as the intervening dielectric layer) were used to validate parts of the model prior to permanently applying a solid dielectric layer to the PCB coils for force sensors. The air between two close coils acts as a dielectric, and the two coils interact as a sensor would with mutual inductance and capacitance present. Air gap testing involved displacement of the two coils rather than loading, since an air intervening layer did not make a force sensor. Typical set up involved:

1. Defining the displacement protocol.
2. Setting up the network analyzer + antenna, coils, and extensometer.
3. Running the protocol.
4. Extracting and processing the data.

The MTS program was set up with test variables that dictate run time, step times, coil preload, displacement rate, displacement values, and number of total displacement cycles. Load limits were set low to 5 N. The extensometer was required for these tests, as it provided a more accurate measure of the small displacements necessary for air sensor testing. Displacement was extensometer controlled rather than crosshead controlled.

After defining the test protocol, the network analyzer and antenna were set up for continuous monitoring. A script was used to set up recording of the entire measured spectra at a defined rate and duration. The characterization protocol was used to determine the expected range and magnitude of the air sensor’s resonant frequency. The frequency measurement range was setup so that the network analyzer could capture the entire resonant peak shifts in magnitude and frequency due to changes in displacement. The coils were then aligned and secured to the fixtures via double

sided tape. After securing the coils, the crosshead coil was brought close ($<50\ \mu\text{m}$) to the lower coil, and the extensometer was attached to the fixtures. Final air sensor setup is exemplified in Figure 53.

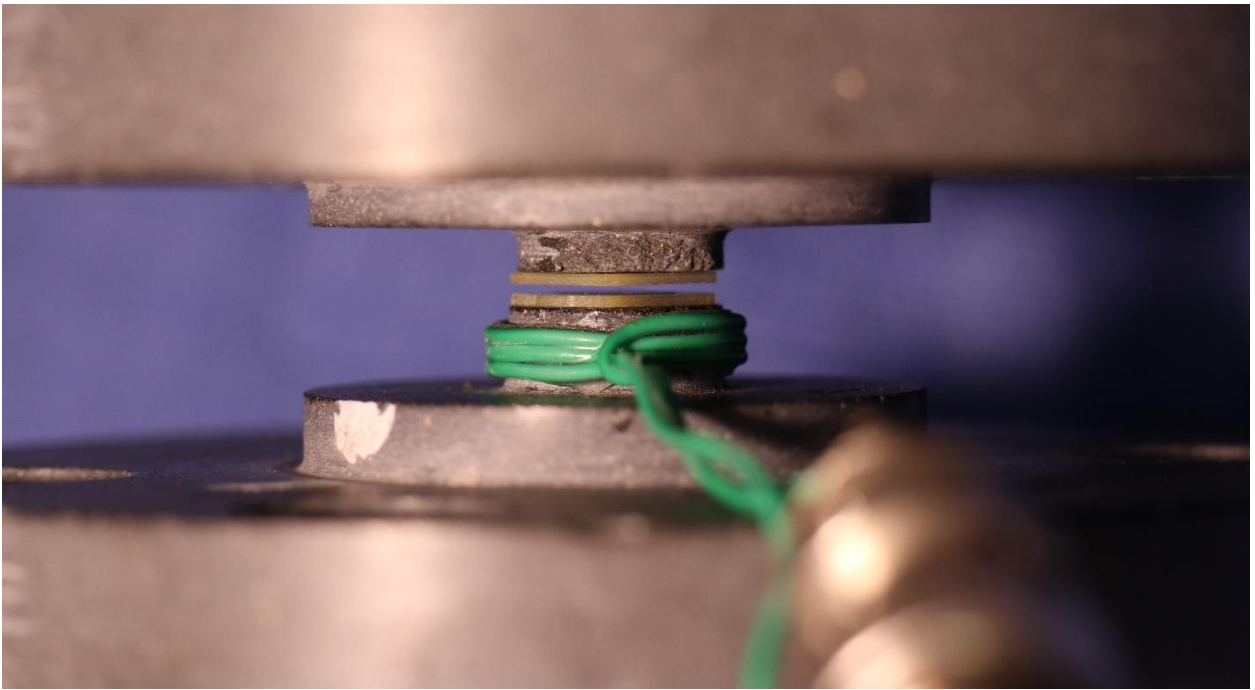


Figure 53: A pair of coils are aligned and secured to the superior and inferior fixtures for air gap displacement testing.

The standard air sensor MTS protocol brought the coils into contact and preloaded them to 2 N. The displacement parameters reported by the MTS and extensometer were zeroed. After starting, the superior crosshead coil was displaced $50\ \mu\text{m}$ as measured by the extensometer. Following a brief thirty second rest, the superior coil was displaced to $100\ \mu\text{m}$. The process repeated with steps to 150, 200, 400, 600, 800, and $1000\ \mu\text{m}$. After reaching $1000\ \mu\text{m}$ and resting, the program checked to see if additional cycles were required. If so, the crosshead coil was brought back into contact with the inferior coil, and the process was repeated. The protocol was done in triplicate with each air sensor combination.

The same protocol was used with smaller displacement values to determine lower displacement air sensor resonant behavior at a higher fidelity. This test was done to elucidate the asymptotic behavior at lower displacements. The tested displacement steps were 20, 30, 40, 50, 60, 70, 80, and 90 μm .

Following the test, each air sensor's data was pulled from both the network analyzer and the MTS program. The resonant peaks were extracted and averaged from the network analyzer data, providing a single plot of resonant frequency over time. Displacement over time was extracted from the MTS data. Combining these two data plots provided the resultant resonant frequency over displacement. These data were then compared to the model's prediction of resonant frequency over displacement. The relevant model inputs for air sensors were geometric parameters of the coils, the relative permittivity of air, and the displacement between coils.

8.4 Solid Sensor Compression Protocol

Parylene C force sensors, or "solid" sensors, were used to validate the force sensor model. Unlike the air sensors, the MTS was used to load and compress the solid sensors and induce a shift in resonant frequency. Typical set up involved:

1. Defining the compression protocol.
2. Setting up the network analyzer + antenna, sensor, and extensometer.
3. Running the protocol.
4. Extracting and processing the data.

The MTS program was set up with test variables that dictate run time, step times, coil preload, extension rate, loading rate, load values, and number of cycles. Load and break limits were set at

1000 N and 5% the current load, respectively. The extensometer was equipped for this test to measure solid sensor strains

Setup was similar to the air sensor protocol. The network analyzer and antenna were set up to continuously capture resonant frequency across the sensor's entire response range. The sensor was centered on the inferior fixture. Double sided tape was not used to secure the coil, as it deforms under the designated load range, skewing measured sensor strains. The superior, crosshead fixture was brought close to the sensor ($<50 \mu\text{m}$), and the extensometer was attached to the fixtures. Final solid sensor setup is shown in Figure 54.

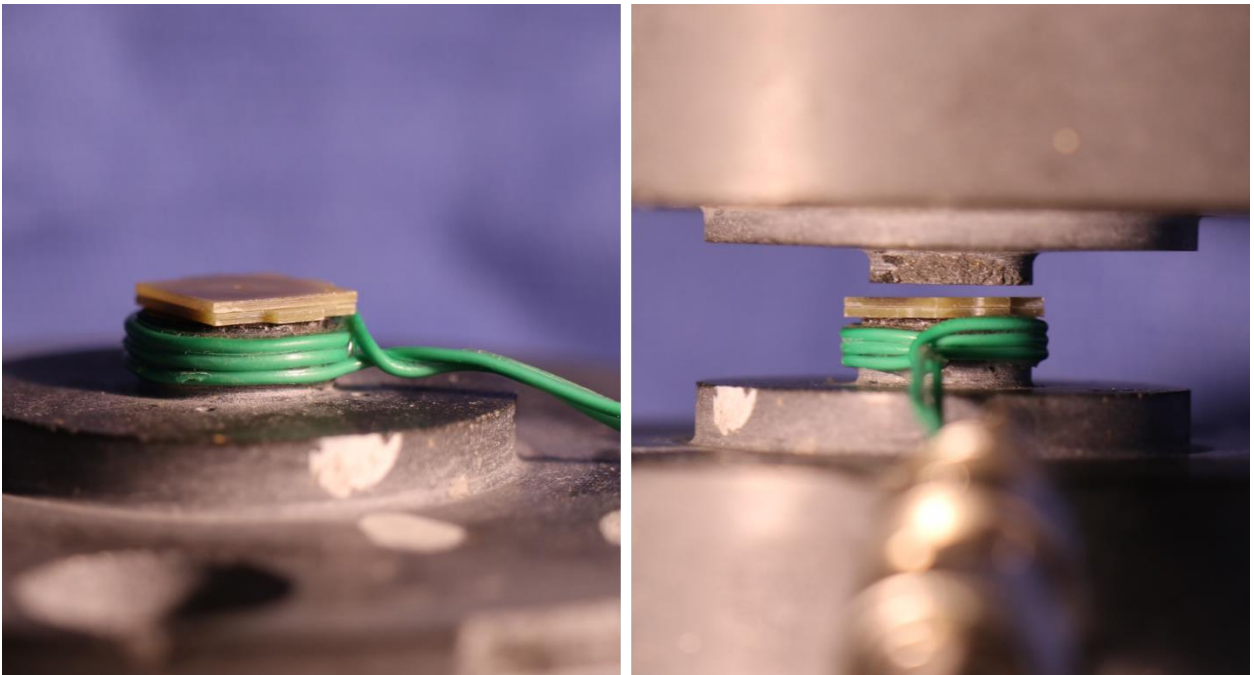


Figure 54: Solid sensors are centered on the inferior fixture, then the superior fixture is brought into contact with the sensor for compression testing.

The standard MTS compression protocol brought the superior fixture into contact with the sensor, preloading it to 5 N. The load and displacements were zeroed. After starting, the MTS compressed the sensor to 25 N and held this load for one minute. The MTS then unloaded to the

zeroed displacement and held for one minute. The process repeated with steps to 50, 75, 100, 200, 300, 400, and 500 N. The program then checked if additional cycles were required and repeated the entire process as necessary. Tests were done in triplicate for each solid sensor.

Like the air sensors, each solid sensor's data was pulled from both the network analyzer and the MTS program. Measured shifts in resonant frequency were synced to the measured loads and resultant strains. These data were combined to determine the resultant sensor's sensitivity, measured in N/mm. These data were then compared to the model's prediction of the sensor's load vs. displacement behavior and sensitivity. The relevant model inputs for solid parylene C sensors were geometric parameters of the coils, the relative permittivity and compressive modulus of the parylene C, and the thickness of the parylene layer.

8.5 Fabrication and Characterization of Solid Sensors with Varying Thicknesses

A batch of solid sensors with identical coil geometries were manufactured with varying intervening layer thicknesses. These sensors were unloaded, and the variable thicknesses simulated a single solid sensor under different strains. Accurately controlling the thickness posed challenges, but an array of sensors with parylene C layers from 30 to 120 μm thick were manufactured. These sensors were tested using the coil characterization protocol, and the resultant measures were compared to a sensor of the same geometric design undergoing equivalent strains.

9. SPECIFIC AIM 2B: RESULTS

9.1 Results of Coil Characterization

9.1.1 Designed Coil Characterization

Coils were first visually inspected for obvious defects before geometric parameters were measured. A total of 48 first generation coils were measured in triplicate. OD, ID, Tw, Ts, and Th are outer diameter, inner diameter, trace width, trace spacing, and trace height, respectively. Table 12 shows measured first generation coil parameters.

Table 12: Measured geometric parameter means in first generation designs.

Gen 1	D2	D3	D7	D8
OD (mm)	10.44	7.94	7.65	7.80
ID (mm)	5.64	4.42	4.60	4.20
Tw (μm)	162.6	161.9	199.7	112.7
Ts (μm)	151.8	154	199.6	94.7
Th (μm)	32.0			

Second generation coil parameters are listed in Table 13. A total of 36 second generation coils were measured in triplicate.

Table 13: Measured geometric parameter means in second generation designs.

Gen 2	D1	D3	D7	D9	D15	D16
OD (mm)	10.09	11.19	12.17	11.2	8.18	12.44
ID (mm)	5.52	4.17	3.16	0.65	3.14	6.25
Tw (μm)	136.4	95.0	79.7	99.1	78.4	288.7
Ts (μm)	160.2	101.3	69.2	96.5	72.2	302.1
Th (μm)	16.6					

Third generation iterations of D15 are different from the previous generation, as seen in Table 14.

A total of 48 third generation coils were measured in triplicate.

Table 14: Measured geometric parameter means in third generation designs.

Gen 3	D15
OD (mm)	8.24
ID (mm)	3.24
Tw (μm)	71.9
Ts (μm)	72.6
Th (μm)	18.0

Coil designs were designated by their generation number (G#) and design number (D#). Resonant frequency characterization followed coil parameter measurements. Average measured resonant frequency for each coil design is listed in table 15. Coils were measured with a loop antenna on a single alumina silicate fixture.

Table 15: Mean measured coil resonant frequencies in MHz.

	Design	Measured	Eq 7	Eq 6
1st Gen	G1D2	300.9	295.7	294.6
	G1D3	513.8	523.3	513.6
	G1D7	770	758.3	777.3
	G1D8	350	341.1	342.3
2nd Gen	G2D1	303	310.8	311.2
	G2D3	147.8	147.4	149.7
	G2D7	92.3	89.5	91.7
	G2D9	140.5	150	152.8
	G2D15	208.7	205	206.8
	G2D16	391.4	387.4	430.6
3rd Gen	G3D15	207.6	196.3	204.4

The two sets of predictions for the coil values represent different approaches to predicting a coil's inductance behavior. Equation 7 is Mohan *et al*'s experimentally derived coil inductance modeling technique, while Equation 6 is Zierhofer and Hochmair's concentric circles approach to coil inductance.

Coils were considered viable, or fit for sensor manufacture, if resonant frequencies were 30 MHz within the expected resonant frequency and if coil return losses exceeded -1 dB. To simplify, coils that did not return a measurable or feasible resonant frequency were considered non-functional. Table 16 shows the average viability of each generation's coils.

Table 16: Coil viability in each generation.

	Gen 1	Gen 2	Gen 3
Average coil viability	81.25%	100%	100%

Coil viability was dependent upon manufacture quality. Issues with improper etches caused shorts and discontinuities in the smaller design geometries. Gen 2 and gen 3 viability was 100% due to

improved manufacturer capabilities. Improved manufacturing tolerances led to cleaner copper etches, reducing possible bridging between traces. Improved copper metal quality also reduced damage in copper features.

9.1.2 Other Coil Characterization

Additional PCB and microfabricated coils previously fabricated were compared against the model. These larger PCB coils had significantly larger geometries not suitable for applications in smart cervical implants. The microfabricated coils had a Borofloat glass substrate and 2 mil copper features that current PCB manufacture methods cannot achieve. Table 17 shows the measured geometries for these additional coil designs.

Table 17: Additional coil geometries measured for model validation.

	OD (mm)	ID (mm)	Tw (μm)	Ts (μm)	Th (μm)
μHalo	11.0	5.3	100.0	50.0	30.0
μDisc	12.0	0.1	160.0	50.0	7.0
MG11	21.8	7.2	380.0	290.0	38.0
MG12	23.4	13.2	365.0	360.0	
MG13	21.9	11.6	245.0	275.0	
MG21	24.8	8.8	460.0	350.0	
MG22	24.8	10.4	485.0	410.0	
MG23	23.4	11.6	260.0	335.0	
MG31	21.7	6.9	455.0	215.0	
MG32	21.8	11.5	410.0	260.0	
MG33	21.8	11.5	320.0	200.0	

Borofloat glass substrate thickness and relative permittivity were 1 mm and 4.6, respectively. The large PCB coils' substrate thickness and relative permittivity were 1.6 mm and 4.4, respectively.

Table 18 shows mean resonant frequency measures for each of the extra coils.

Table 18: Mean measured frequencies (in MHz) of large PCB coils and microfabricated coils for further model validation.

Design	Measured Coil F0 (MHz)	Predicted Coil F0 Eq 7 (MHz)	Predicted Coil F0 Eq 6 (MHz)
μHalo	107.2	108.9	112.5
μDisc	130.0	125.3	126.8
M11	132.1	126.7	131.0
M12	142.9	141.3	148.5
M13	111.6	113.6	117.1
M21	125.1	119.4	123.5
M22	141.8	137.0	144.7
M23	112.0	115.6	118.2
M31	127.4	119.6	125.5
M32	148.8	134.6	135.8
M33	113.6	104.4	107.8

9.1.3 Parylene C Coated Coil Characterization

Parylene C coated coils were measured and tested against the model as well. Table 19 shows a subset of third generation PCB coils with varying amounts of parylene C. Two coils for each thickness were measured in triplicate.

Table 19: Comparison of measured and predicted resonant frequencies for third generation coils with 0, 36, and 54μm thick layers of parylene C.

Parylene t (μm)	Measured F0 (MHz)	Predicted F0 (MHz)
0	210.3	206.2
36	204.7	200.5
54	201.3	193.6

The zero thickness indicates an uncoated coil that was used for comparison to the coated coils. Average measured return loss had no significant change compared to uncoated coils.

9.2 Analysis of Coil Characterization

Coil characterization provided an initial overview of how subsequent sensors behaved. Additionally, coil data was used for force sensor model validation. Intracoil inductance and capacitance comprises a significant portion of sensor behavior.

Actual coil geometries differed from their designed parameters. On average, first generation coils varied by 0.26 mm, 0.47 mm, 8.63 μm , and 3.23 μm between their designed and actual OD, ID, Tw, and Ts geometries, respectively. On average, second generation coils varied by 0.21 mm, 0.32 mm, 1.69 μm , and 2.36 μm between their designed and actual OD, ID, Tw, and Ts geometries, respectively. Third generation coils varied by 0.24 mm, 4.26 μm , and 3.58 μm between their designed and actual OD and ID, Tw, and Ts, respectively. Slight changes in etch time, board layout, and copper volume between batches resulted in these geometric variations. These geometric measurements were used in the model to produce more accurate resonant frequency predictions that reflect their actual resonant behavior.

The measured coil resonant frequencies and predicted coil resonant frequencies were compared to assess model accuracy. Table 20 shows error (%) between the predicted and the average measured resonant frequencies for all coil designs.

Table 20: Percent errors of predicted coil behavior. Red and orange shading indicate error less than 5% and 10%, respectively.

	Design	% Error Eq 7	% Error Eq 6
1st Generation	G1D2	1.76	2.15
	G1D3	1.82	0.04
	G1D7	1.54	0.94
	G1D8	2.61	2.25
2nd Generation	G2D1	2.52	2.63
	G2D3	0.26	1.27
	G2D7	3.05	0.64
	G2D9	6.37	8.10
	G2D15	1.80	0.92
	G2D16	1.03	9.11
3rd Generation	G3D15	5.71	1.55
< 5% Error			
< 10% Error			

All predicted coil resonant frequencies fell well within 5% error for both inductance modeling techniques, except for G2D9, G2D16, and G3D15. G2D16's large design caused issues with inductance approximations, resulting in an increased error with the coil inductance modeling techniques. As for G3D15, it is unclear why the error exceeded 5% with the first modeling technique. The coil model indicated small changes in coil inductance and capacitance between these two similar geometries. G2D15 had a predicted coil capacitance of 3.460×10^{-13} F and a predicted coil inductance of 1.712×10^{-6} H. G3D15, the same design with slightly different measured geometric parameters, had a predicted coil capacitance of 3.443×10^{-13} F and a predicted coil inductance of 1.761×10^{-6} H. The measured resonant frequencies of these coils differed by less than 1 MHz, but the predicted resonance differed by 8.7 MHz, indicating some unexplained sensitivity in the model. Regardless, all coil predictions fell within 10% error of the measured values. The large PCB and microfabricated coils were also compared against the model, as seen in Table 21.

Table 21: Percent errors of predicted frequency behavior for additional PCB and microfabricated coils. Green and red shading indicate error less than 5% and 10%, respectively. Gray indicates errors outside of 10%.

Design	% Error Eq 7	% Error Eq 6
μ Halo	1.58	4.74
μ Disc	3.73	2.51
MG11	4.28	0.85
MG12	1.14	3.73
MG13	1.78	4.71
MG21	4.77	1.33
MG22	3.46	2.00
MG23	3.10	5.22
MG31	6.49	1.46
MG32	10.54	9.57
MG33	8.74	5.37
< 5% Error		
< 10% Error		

Microfabricated coil predictions fell within 5% error of the measured. The model addressed changes in substrate material properties, and it handled coil features as small as 50 μm . The model could theoretically handle smaller coil features. The accuracy of large PCB coil resonant frequency predictions decreased as the size of the coil increases. Like G2D16, the larger geometries caused issues with inductance approximations. Mohan *et al*'s inductance calculation method (Equation 7) tended to lose accuracy as the copper feature sizes increased, likely due to the experimentally derived formula's basis on a set range of coil sizes. The derived inductance expression was based on samples with a maximal outer diameter of 700 μm and width/spacing of 90 μm [61].

Zierhofer and Hochmair's method (Equation 6) approximates spiral traces as concentric circles and calculates mutual inductance between each of these concentric circles, as seen in Figure 55.

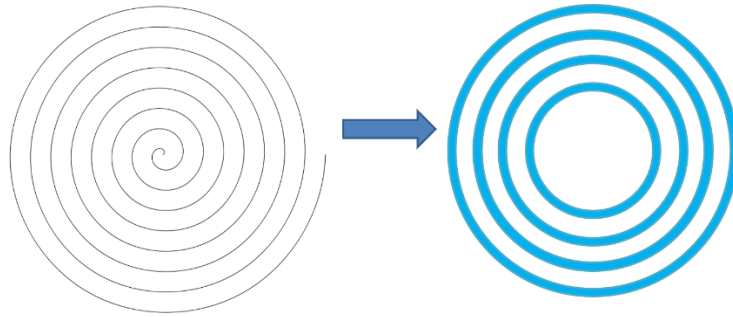


Figure 55: Concentric circles approximation can break down in coils with less turns.

As the number of turns decreases, the inaccuracies of this method increase [60]. Concentric circles approximate the spiral arc, introducing improperly scaled inductive interactions between adjacent traces. Fewer circles imply larger errors in predicting coil inductance. Larger trace width and spaces as well as smaller outer diameters and larger inner diameters reduce the number of turns in a coil, making them harder to predict accurately with the concentric circles method. For example, MG32's predicted resonant frequency had the highest error due to the lowest number of turns in the group. Larger coils (>2 cm) for applications outside of smart cervical implants will require either some scaling factor or an alternative approach to modeling inductance. Both coil inductance expressions were used throughout the entire validation process to determine the best method of resonant frequency estimation.

Parylene coated coils were also considered in model validation. These were modeled as coils with an additional layer above the copper traces, altering the overall permittivity of the system. This led to a change in coil capacitance dependent upon layer thickness and relative permittivity. Table 22 shows the error between measured and predicted resonant frequencies of third generation, parylene C coated coils.

Table 22: Percent errors of predicted resonant frequencies for parylene coated coils.

Parylene t (μm)	% Error
0	4.01
36	2.09
54	4.01

In this subset of G3D15 coils, the error remained within 5% even as the parylene layer thickness approached the maximum single deposition thickness in manufacture.

Results demonstrated that coil behavior was accurately predicted with the current iteration of the force sensor model. Coil behavior describes parasitic, intrinsic inductive and capacitive properties within a sensor, and understanding these properties allow us to minimize them and design sensors with maximal mutual inductive and capacitive properties for optimal sensitivity and readability. Accurate coil predictions provide a strong basis to develop and test air and solid sensor predictive models.

9.3 Results of Air Sensor Testing

First generation coils were tested in the air sensor configuration using the same MTS protocol described in Section 8.3. Six pairs for each design were tested in triplicate. Figure 56 charts the average resonant frequency versus displacement for first generation air sensors.

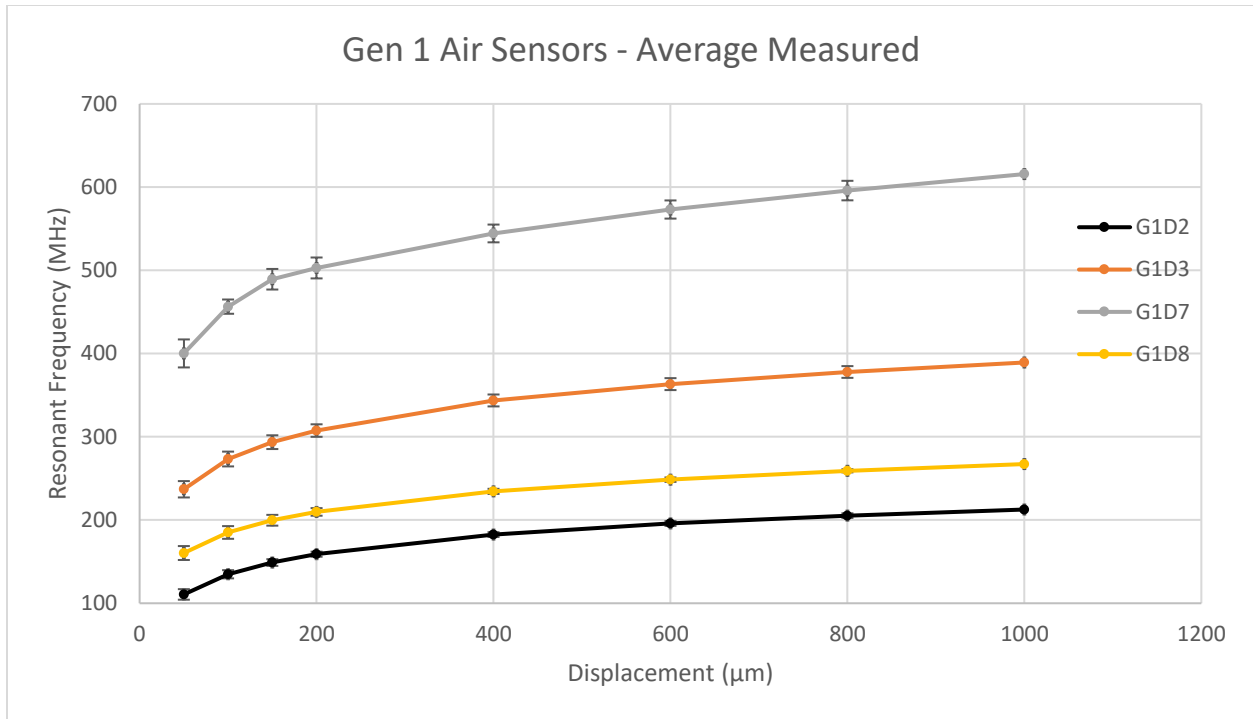


Figure 56: Four first generation air sensors were tested mechanically with an air gap to determine the displacement-frequency relationship. Error bars show one standard deviation based on three measurements.

Of the first-generation air sensors, five out of six G1D8 coil pairs were non-functional. Additionally, G1D7 coil pairs exhibited high variances compared to other designs.

Second generation coils were tested in the air sensor configuration using the standard MTS protocol described in Section 8.3. Three pairs for each design were tested in triplicate. Figure 57 shows the average resonant frequency versus displacement for second generation air sensors.

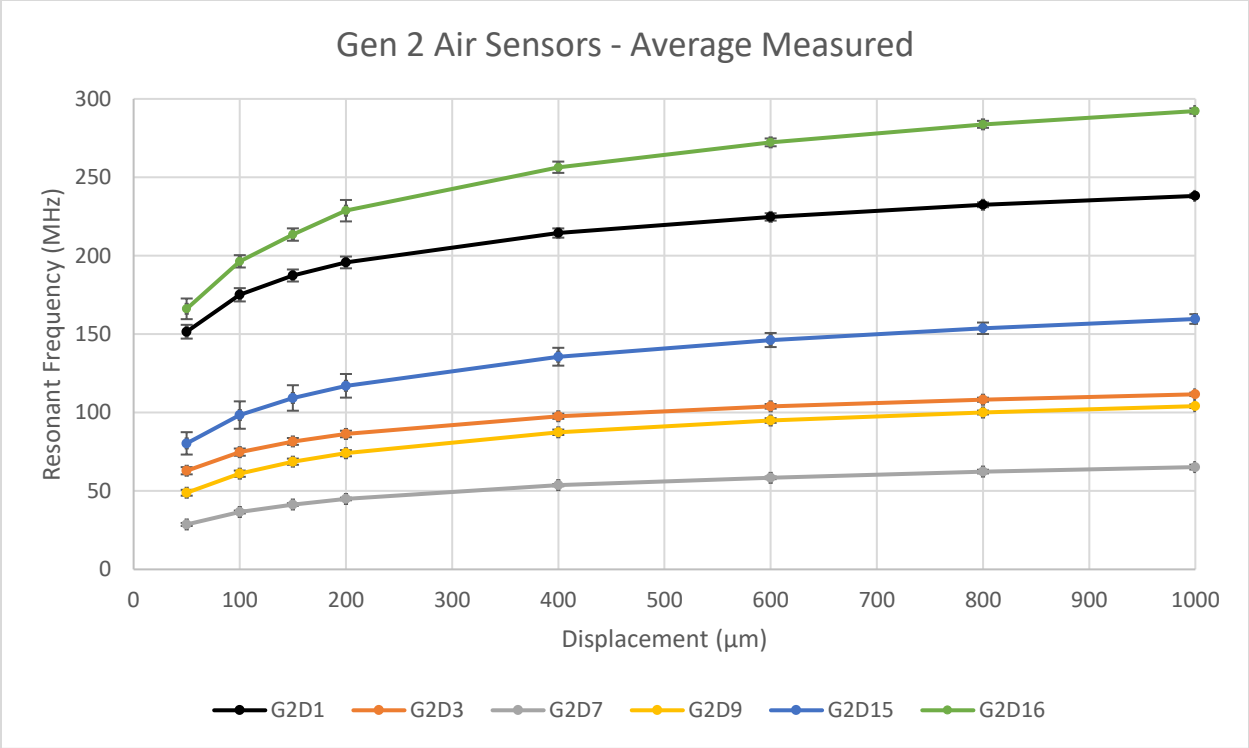


Figure 57: Six second generation air sensors were tested mechanically to determine their mean frequency-displacement behavior. Error bars show one standard deviation based on three measurements.

All coil pairs were viable, though the G2D15 design exhibited high variance in its resonance-displacement behavior between pairs, even after retesting. Higher frequency coil pairs tended to exhibit more variance than lower frequency coil pairs.

Third generation coils were tested in the air sensor configuration using the standard MTS protocol described in Section 8.3. Four pairs were tested in triplicate for this design. Figure 58 shows the average resonant frequency versus displacement for third generation air sensors.

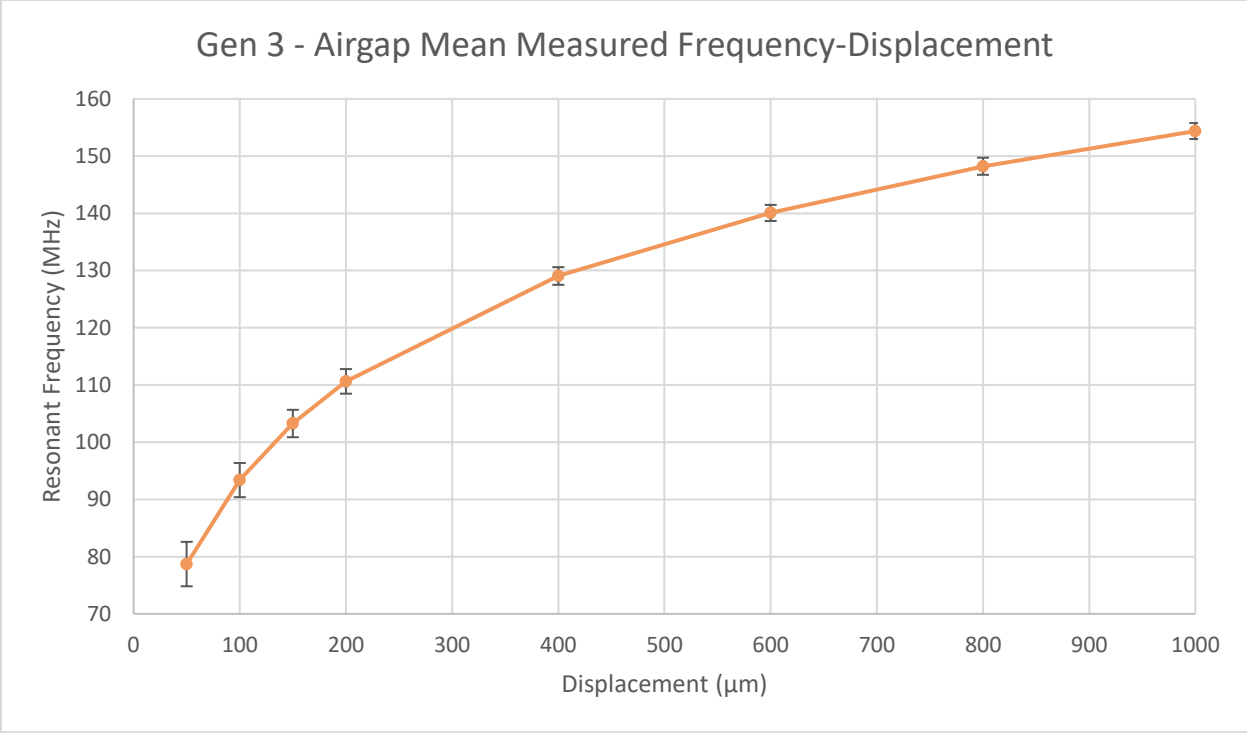


Figure 58: Third generation air sensors were mechanically tested to determine their mean frequency-displacement behavior. A plot showing the resonant frequency vs. displacement behavior of third generation air coils as tested on an MTS. Error bars show one standard deviation based on three measurements.

All coil pairs were viable. To address uncertainty at the lower load ranges, a second round of air sensor testing was done with the same coil pairs over a range of 20 to 90 μm on the MTS. Figure 59 shows the average frequency-displacement curve of this small displacement range.

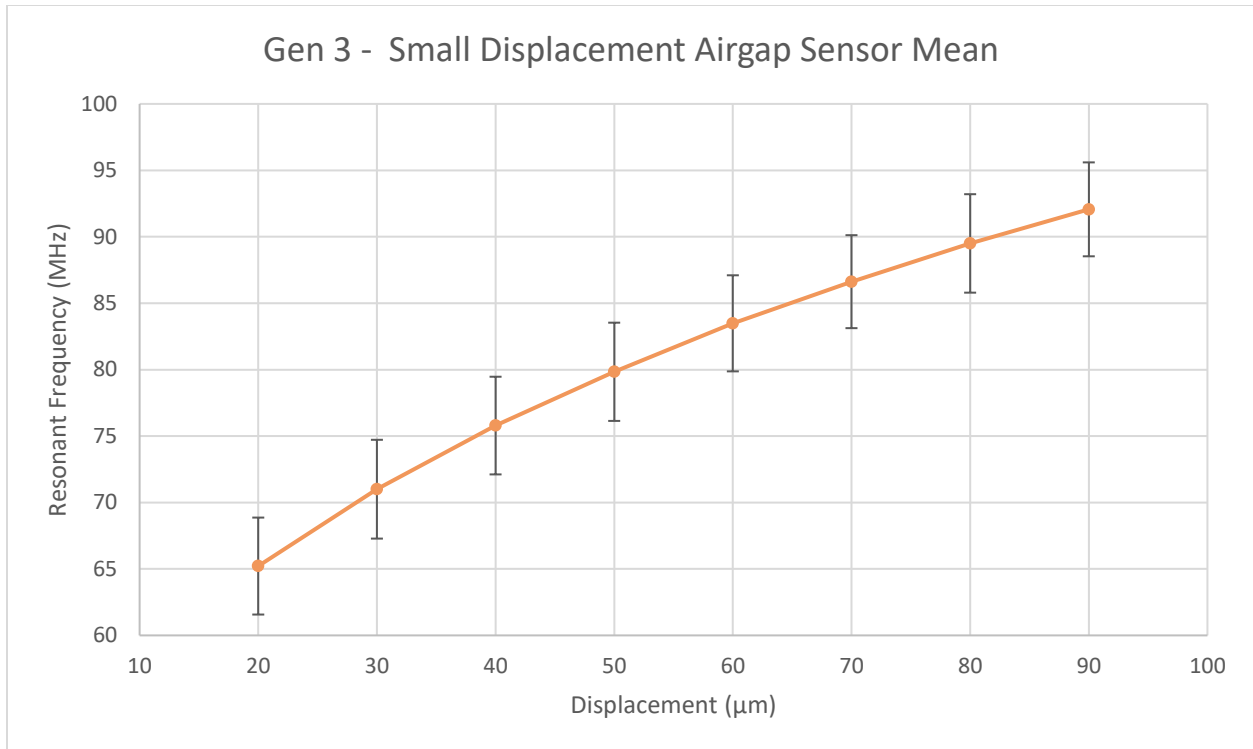


Figure 59: Third generation air sensors were mechanically tested over a small displacement range of 20 to 90 μm to determine mean frequency-displacement behavior. Error bars show one standard deviation based on three measurements.

Despite access to extensometer-controlled displacement, lower displacement air sensors exhibited notable variance across the entire displacement range.

9.4 Analysis of Air Sensor Testing

9.4.1 Model Accuracy for Air Sensors

Model accuracy was qualified with coefficient of determination (R^2) as well as error at each displacement step. All air sensor behavior followed a combined asymptotic-logarithmic trend.

Figure 60 shows a measured versus predicted curve for design G1D2.

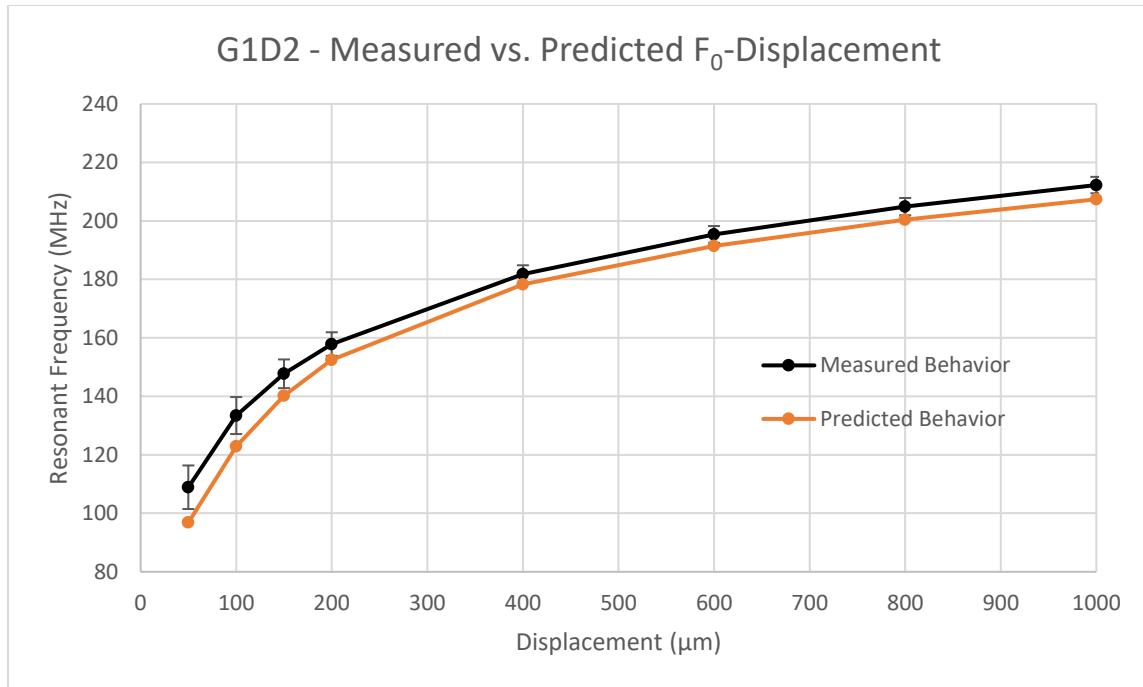


Figure 60: Measured and predicted frequency-displacement behavior for the G1D2 design is compared. Error bars show one standard deviation based on three measurements.

Appendix 1-4 shows all first generation, measured versus predicted, air sensor curves. Table 23 shows the percent error between the measured and predicted at each displacement step for all first-generation designs.

Table 23: Percent errors of predictions for first generation air sensors over a 50-1000µm range.

Gen 1		Displacement (µm)								
Design	Method	0	50	100	150	200	400	600	800	1000
G1D2	% Error Eq 4	-	12.47	8.54	5.36	3.58	1.98	2.06	2.23	2.34
G1D3	% Error Eq 4	-	21.76	14.03	8.89	5.93	2.93	2.11	1.76	1.44
G1D7	% Error Eq 3	-	29.49	23.40	20.39	14.86	7.59	6.59	6.21	6.37
G1D8	% Error Eq 3	-	30.35	18.38	13.65	11.26	8.93	8.13	7.87	7.52

High errors occurred at the low displacement ranges of 50 to 100 μm . Average errors for G1D2, G1D3, G1D7, and G1D8 were 2.34%, 1.44%, 6.37%, and 7.52%, respectively. Theoretically, coils with zero displacement short and do not exhibit resonant behavior. In reality, sensor resonance could sometimes occur while coils were in contact. This behavior is due to the coil pair's ability to resonate despite having random, physical, electrical connections between traces

Figure 61 shows a measured versus predicted curve for design G2D15.

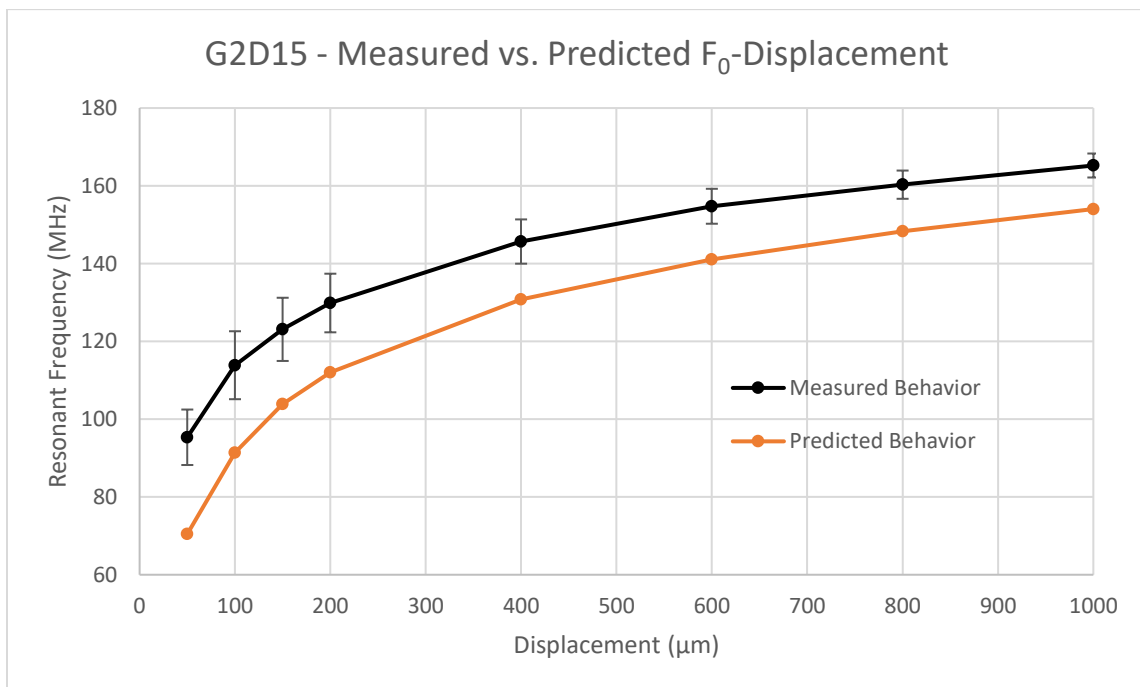


Figure 61: Measured and predicted frequency-displacement behavior of the G2D15 design is compared Error bars show one standard deviation based on three measurements.

Appendix 5-10 shows measured versus predicted frequency-displacement behavior for all second-generation air sensor curves. Table 24 shows the percent error between the measured and predicted at each displacement step for all designs.

Table 24: Percent errors of predictions for second generation air sensors over a 50-1000 μ m range.

Gen 1		Displacement (μ m)								
Design	Method	0	50	100	150	200	400	600	800	1000
G2D1	% Error Eq 4	-	36.74	26.23	19.11	14.75	7.92	5.56	4.45	3.49
G2D3	% Error Eq 3	-	36.65	23.99	17.49	14.18	8.89	6.97	5.74	5.02
G2D7	% Error Eq 3	-	16.49	11.16	8.06	6.89	5.13	3.91	4.54	4.61
G2D9	% Error Eq 3	-	25.86	16.88	12.22	9.58	4.97	2.95	1.63	0.83
G2D15	% Error Eq 3		35.29	24.58	18.50	15.93	11.40	9.72	8.10	7.27
G2D16	% Error Eq 3		26.40	17.45	12.82	10.87	2.28	0.76	1.99	2.85

Average errors for G2D1, G2D3, G2D7, G2D9, G2D15, and G2D16 were 14.8%, 14.87%, 7.60%, 9.37%, 16.35%, and 9.43%, respectively. The 50 and 100 μ m displacement steps were again the largest contributors to discrepancies between the measured and predicted resonant behavior of second-generation air sensors. G2D7 and G2D9 had significantly lower base frequencies, so sensitivity to compounding model errors was reduced.

Figure 62 shows the measured versus predicted frequency-displacement curve for third generation air sensors.

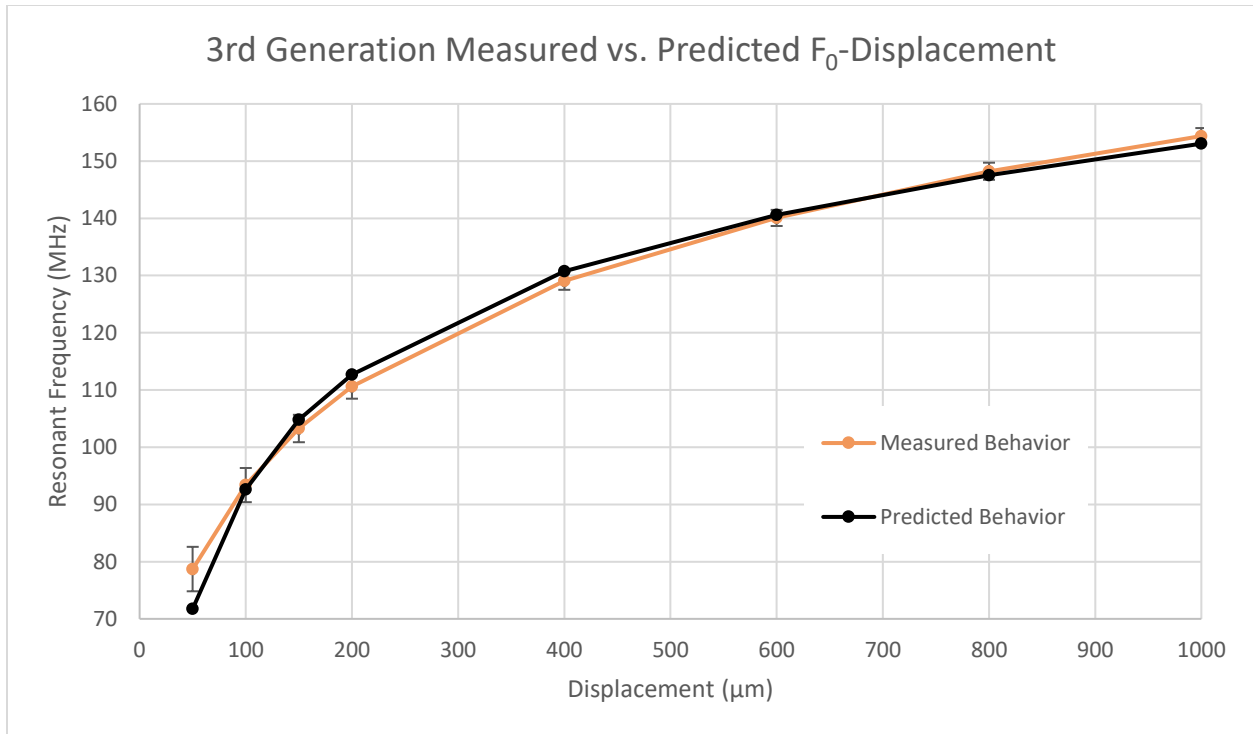


Figure 62: Measured and predicted frequency-displacement behavior of the G3D15 design is compared Error bars show one standard deviation based on three measurements.

Figure 63 shows the measured versus predicted frequency-displacement curves for the same third generation sensors over a small displacement range of 20 to 90 μm .

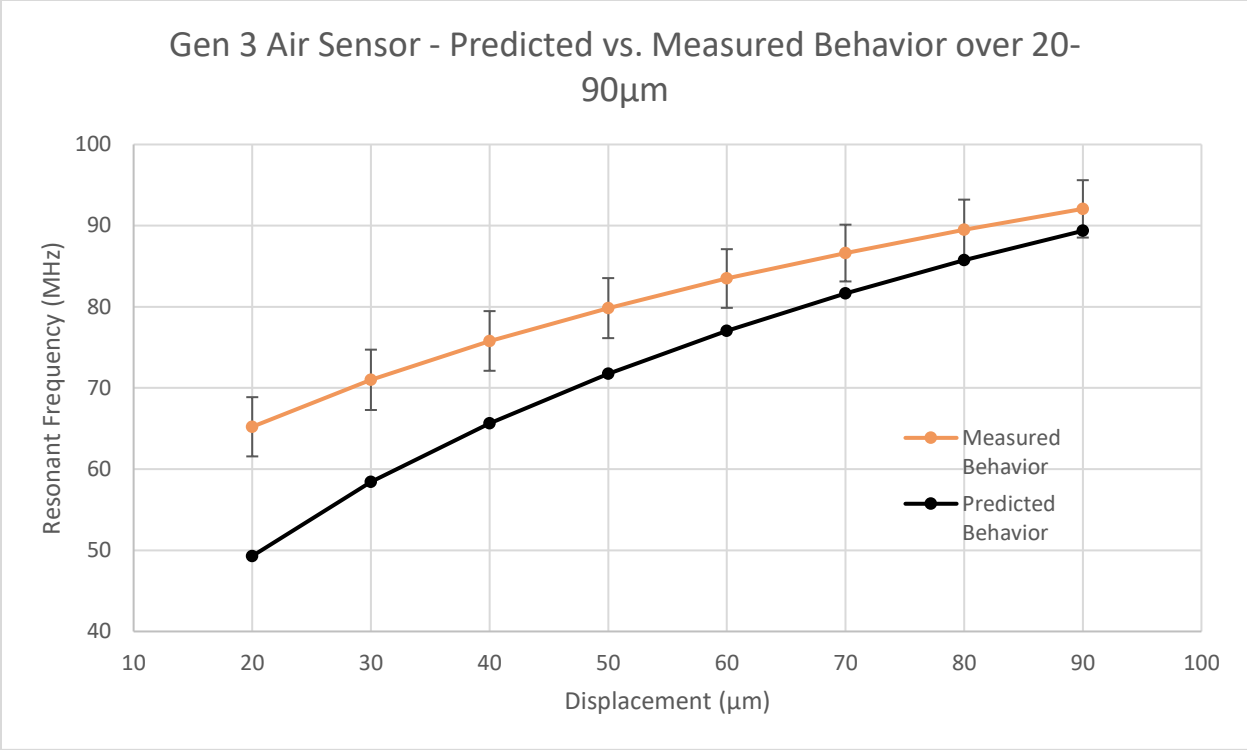


Figure 63: Measured and predicted frequency-displacement behavior of the G3D15 design is compared over a smaller 20-90 µm range. Error bars show one standard deviation based on three measurements.

Table 25 shows the percent error between the measured and predicted at each displacement step for all designs. Third generation air sensor protocol differed slightly by placing the coils aligned and in contact with each other on the inferior fixture. The normal method involved placing the superior coil on the superior fixture first, then bringing the coils into contact with each other.

Table 25: Percent errors for third generation air sensors over a 20-1000 μm range.

Gen 3		Displacement (μm)								
Design	Method	0	50	100	150	200	400	600	800	1000
G3D15	% Error Eq 3	-	9.67	0.85	1.49	1.83	1.29	0.36	0.47	0.87
Gen 3		Small displacement (μm)								
Design	Method	0	20	30	40	50	60	70	80	90
G3D15	% Error Eq 3	-	32.32	21.55	15.43	11.25	8.36	6.07	4.39	3.03

Average errors for this design at the standard displacement and small displacement ranges were 2.10% and 12.80%, respectively. The small displacement range was difficult to predict, and there are still likely some aspects of experimental design that can be improved. Still, an average 13% error across this range was acceptable and provided useful predictions of air sensor behavior. R^2 values are listed for all designs in Table 26.

Table 26: Mean R^2 value between measured and predicted air sensor frequency-displacement curves.

Design	R^2
G1D2	0.956
G1D3	0.82
G1D7	0.306
G1D8	0.537
G2D1	0.217
G2D3	0.557
G2D7	0.937
G2D9	0.889
G2D15	0.412
G2D16	0.767
G3D15	0.999

The goodness of fit of the predicted data is highly variable between each design. The average R^2 for all air-sensor predictions combined was 0.672. Despite poor fits present in some designs, most prediction errors can be attributed to poor predictability of lower displacements ($< 100 \mu\text{m}$). Figure 63 best exemplifies this trend.

9.4.2 Challenges in Air Sensor Measurement

Air sensors required meticulous setup to produce consistent data. Issues with alignment between coils, crosshead placement, and inherent mechanical test system inaccuracies in measuring displacement posed challenges to produce meaningful air sensor data.

The sensor model operates on the key assumption that coils are perfectly, axially aligned to each other. Slight off-axis alignment can cause significant shifts in resonant frequency [59]. Installation and removal of air sensors in the test setup can introduce variance into the average measured resonant frequency via slight misalignments. The alignment features in the alumina silicate fixtures provided a means to ensure axial alignment, but these features did not align at a micron level like a wafer die bonder can.

Coils were brought into contact to ensure they start at zero displacement. Preload settings dictated when the crosshead stops moving after initiating coil-to-coil contact. The preload value also dictated the time taken to separate the superior coil from the inferior coil after protocol start. Lighter preloads of 1 N resulted in more accurate zero positions, but load cell noise and signal spikes may have tripped false preload limits, subsequently creating incorrect zero displacement positions and no coil contact. Increased preloads of 5 N ensured that the coils were in contact, but due to inherent “slop” in the mechanical testing machine and adhesive deformation, displacement steps were inaccurate by the amount of displacement required to break coil contact. Figure 64 shows a visualization of this phenomenon.

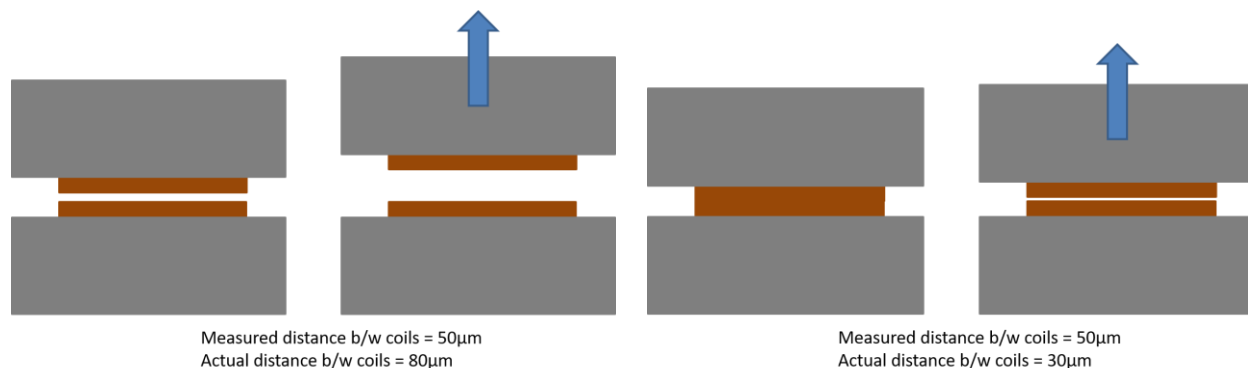


Figure 64: Effects of underloading versus overloading an air sensor in preload. The gray components indicate the fixture, and the brown components indicate the coils.

A preload of 2 N with careful zeroing of the load cell produced the most accurate zero position while limiting displacement error.

Initially, crosshead “back off” was introduced to address preload overload issues. After positioning the coils in contact with each other via preload, displacement was zeroed. The crosshead was then raised 10 µm, and displacement was zeroed again. This technique eliminated some variance in smaller magnitude displacements, but variance between measures was still significant. After refining preload settings and introducing extensometer-controlled displacement, however, the crosshead “back off” was eliminated.

All mechanical test systems have some degree of deformation, or “slop”, in response to a compressive load. Additionally, inertia in the moving parts of the system can preclude accurate displacement measures, especially if displacement sensors monitor these components rather than changes in the sample itself. This discrepancy is especially apparent when a sample is compressed then decompressed. A sample may show no change in loading, but the sensor will report active displacement. Once a desired load is achieved, the measured displacement may not accurately reflect the actual displacement that occurred within a sample.

This issue was circumvented through use of an external extensometer. The extensometer was connected to a sample or in the case of the sensors, to the fixtures. As a result, sample displacements and strain measurements were more accurate. Figure 65 shows the effects of extensometer-controlled displacement.

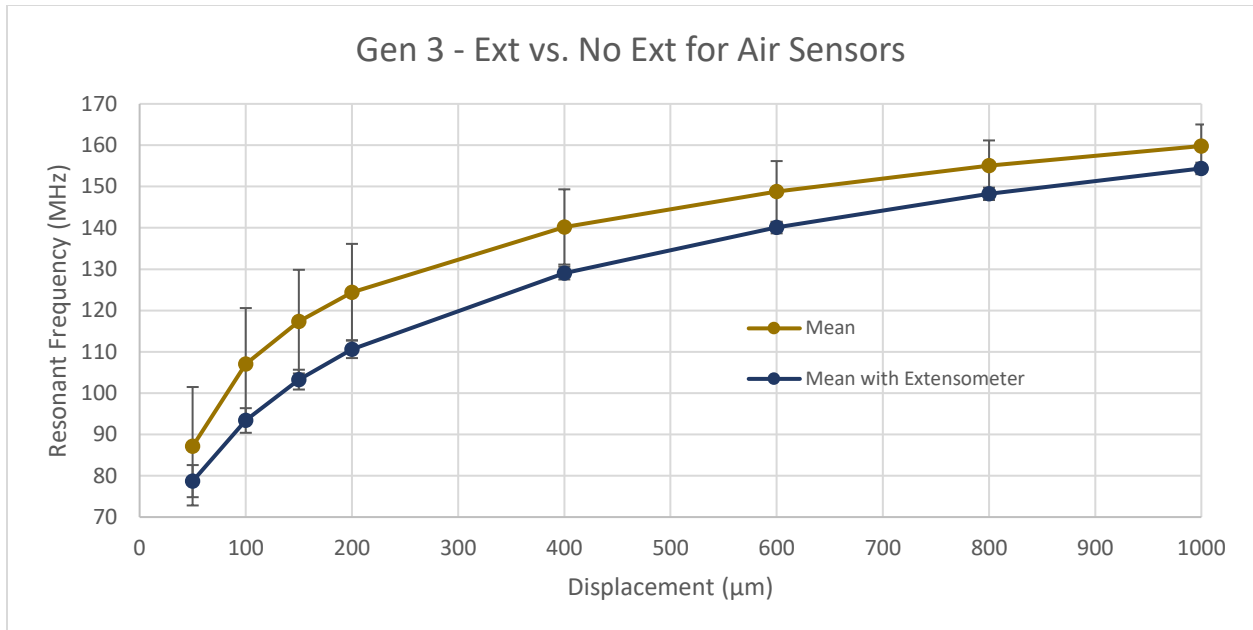


Figure 65: Extensometer-controlled displacement reduces the variance between measurements in air sensors. Error bars show one standard deviation based on three measurements.

The sensors in the displacement protocol without an extensometer exhibited high variance throughout the entire displacement range, while air sensors measured with an extensometer-controlled displacement protocol exhibited significantly less variance. The maximum standard deviation for the extensometer-based air sensors was 4 MHz, as opposed to the standard protocol's peak standard deviation of 14 MHz. The extensometer was especially useful for measuring force sensor strains, as it was also not affected by the MTS inherent displacement in compression.

Despite challenges in testing and validating air sensors, they provided a useful platform for continually adjusting and improving the force sensor model.

9.5 Results of Frequency-Force Behavior

The force sensor model was validated through manufacture and testing of PCB force sensors. Measuring resonant frequencies of loaded sensors and simulating strain through varying intervening geometries provided valuable data for confirming whether the model was accurate enough and useful for future development of force sensors.

A total of three G1D2, one G1D7, and one G1D8 sensors were fabricated and tested under the standard 500 N compression protocol. The protocol provided resonant frequency versus force data, as seen in Figure 66.

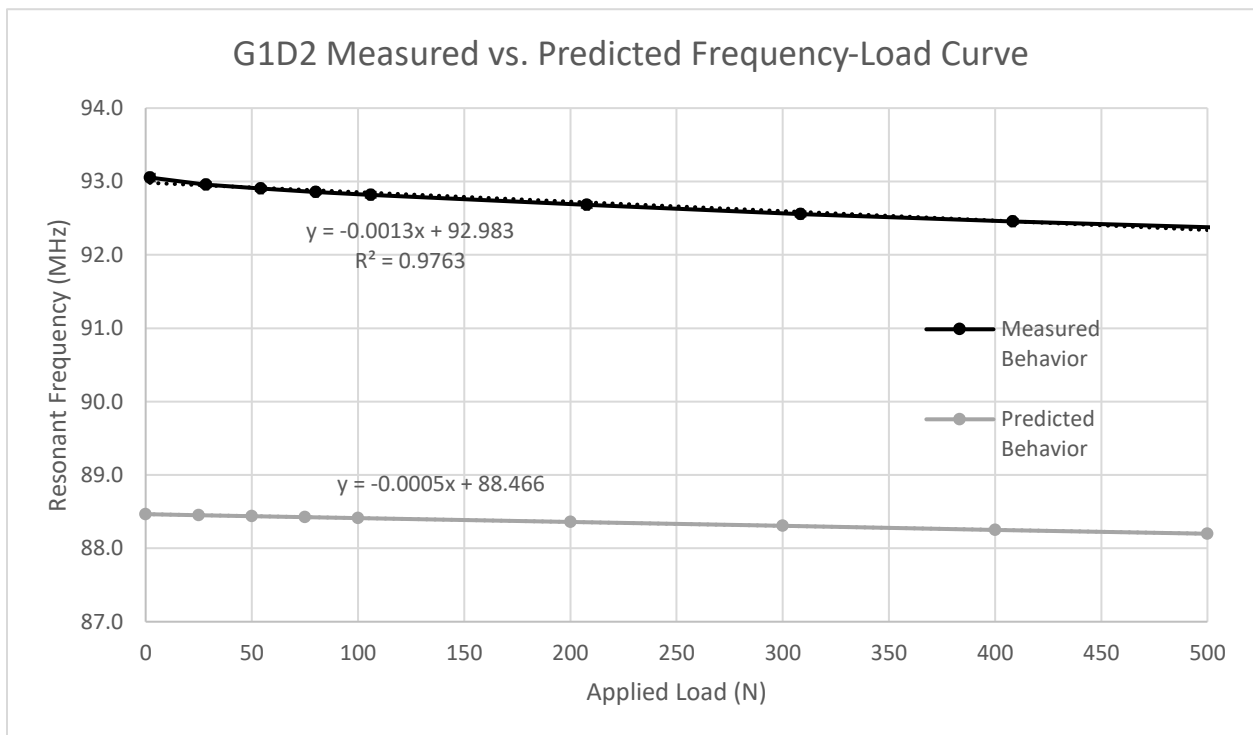


Figure 66: Mean measured versus predicted frequency-load behavior of a solid G1D2 sensor is compared. Error bars show one standard deviation based on three measurements.

All first-generation frequency-load behavior is shown in Appendix 12-16. No first-generation coils were sacrificed for thickness measures due to their variability of parylene C thickness. This group was not indicative of all coils due to variability of deposition on first generation coils prior to deposition protocol changes. Results from the barrel micrometer and profilometry indicated that the thickness could range between 80 and 120 μm with a significant bias towards 120 μm . All first-generation solid force sensors were presumed to be 120 μm thick. G1D3 solid sensors were not functional due to prior deposition issues.

One of G2D1, G2D9, and G2D16 sensors each were fabricated and tested under the standard 500N compression protocol. Three G2D15 sensors were fabricated and tested as well for a total of six second generation solid sensors.

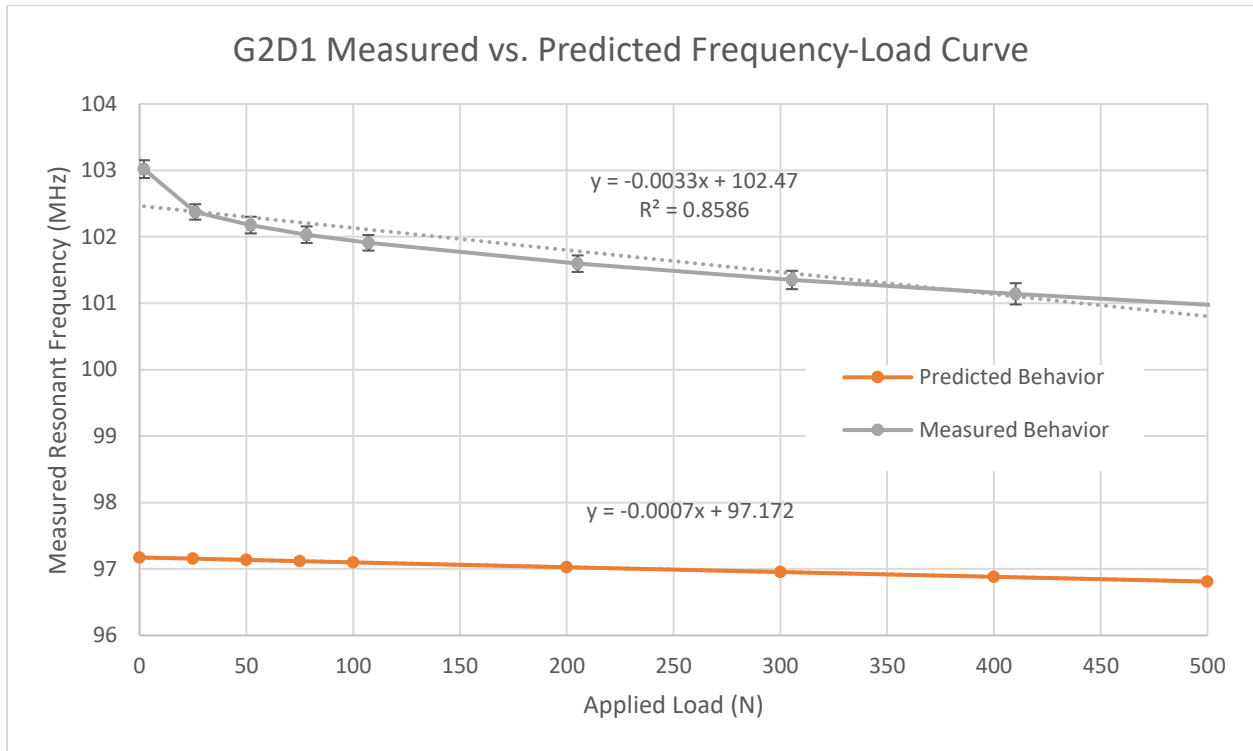


Figure 67: Mean measured versus predicted frequency-load behavior of a solid G2D1 sensor is compared. Error bars show one standard deviation based on three measurements.

All second-generation frequency-load behavior is shown in Appendix 17-22. The known thickness range for this generation was 75.84 to 134.22 μm based on SEM imaging. Only the G2D15 sensors were sacrificed for imaging, so an average thickness of 105 μm was used for G2D1, G2D9, and G2D16 predictions. No G1D3 and G1D7 sensors were available due to issues with functionality, likely due to manufacturing errors.

A total of six solid G3D15 sensors were tested under the standard 500 N compression protocol.

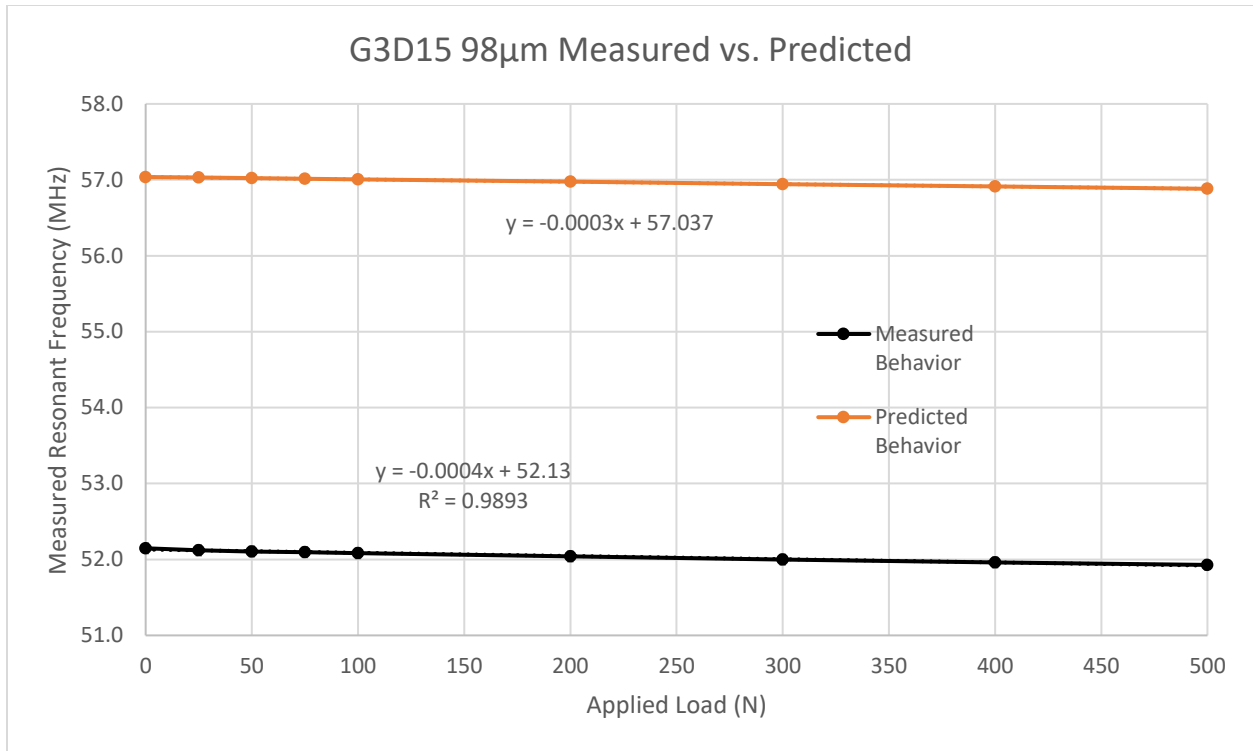


Figure 68: Mean measured versus predicted frequency-load behavior of a solid G3D15 sensor is compared. Error bars show one standard deviation based on three measurements.

All third-generation frequency-load behavior is shown in Appendix 23-28. The thickness for each third-generation solid sensor was known via SEM imaging, providing more accurate predictions of resonant frequency-applied load behavior. All fabricated third-generation solid sensors were viable.

9.6 Analysis of Frequency-Force Behavior (Sensitivity)

Sensor resonant frequencies were accurately modeled over the entire 500 N load range to within a 10 % error. Sensor sensitivity, or the total shift in frequency over a 500 N loading range, was predicted to within the same order of magnitude as the measured shifts over a 500 N loading range. The frequency-force slope was primarily linear, and all predicted frequency-force slopes

across all sensor designs had a minimal R^2 value of 0.89 when the first 50 μm point was removed.

Figure 69 shows the variability in measured sensitivities across all available solid sensors.

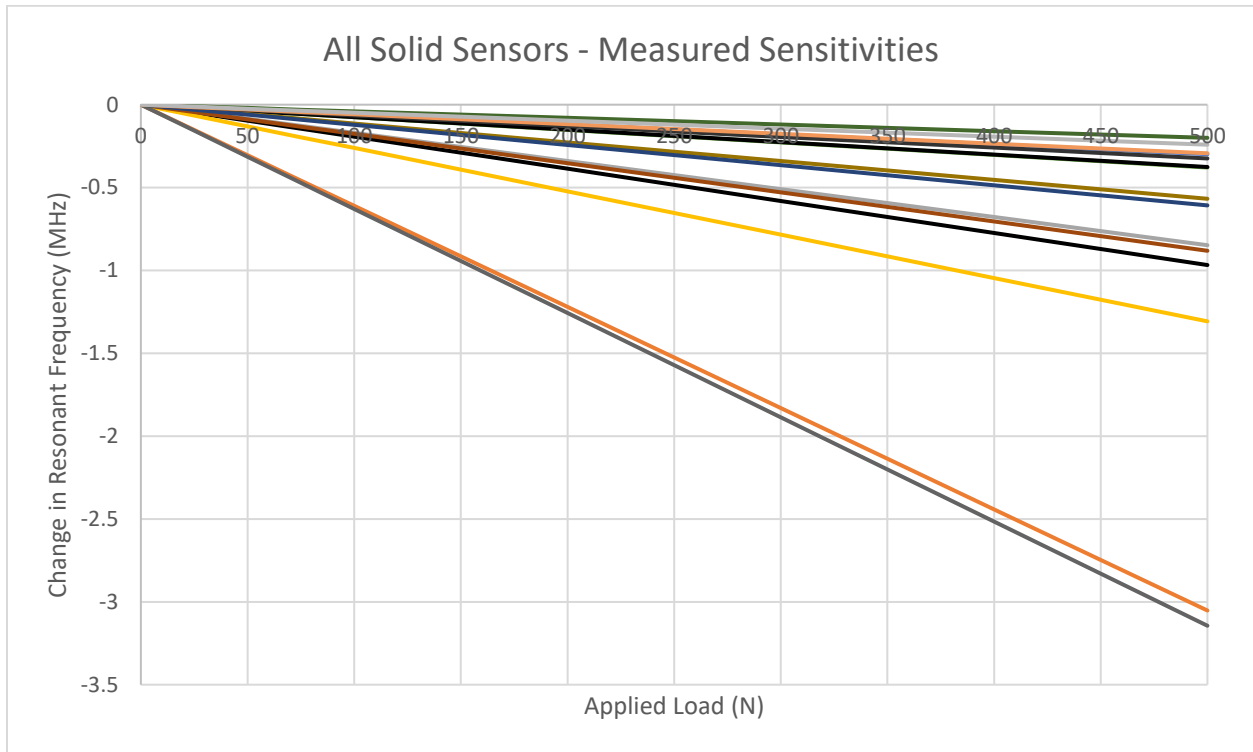


Figure 69: The measured slope (MHz/N) of each solid sensor ranged from -0.25 MHz/N to a little over -3 MHz/N.

Comparing this chart to the predicted values, as seen in Figure 70,

Additionally, sensitivities were high enough for all sensors to resolve ± 1 N changes in force. Appendix 29-31 shows tables containing adjusted sensitivities for each generation of solid sensors.

To address force sensor sensitivity uncertainties due to manufacturing, third-generation coils were used to build sensors with varying thicknesses. This approach emulated deformations in the intervening layer when testing these sensors unloaded. The resulting data were used to validate the force sensor model across a wide range of intervening layer thicknesses.

9.7 Varying Thickness Parylene C Layers

9.7.1 Results of Fabrication and Testing of Varying Thickness Sensors

A total of eleven different parylene C thickness sensors were manufactured for final force sensor model validation. Unloaded sensors were measured and plotted in a curve that simulates a loaded sensor's deformation and frequency response. The sensors were measured in triplicate using the coil characterization protocol. They were then sacrificed for SEM imaging to measure intervening layer thickness. Figure 71 shows the measured versus predicted resonant frequency-parylene C thickness curve.

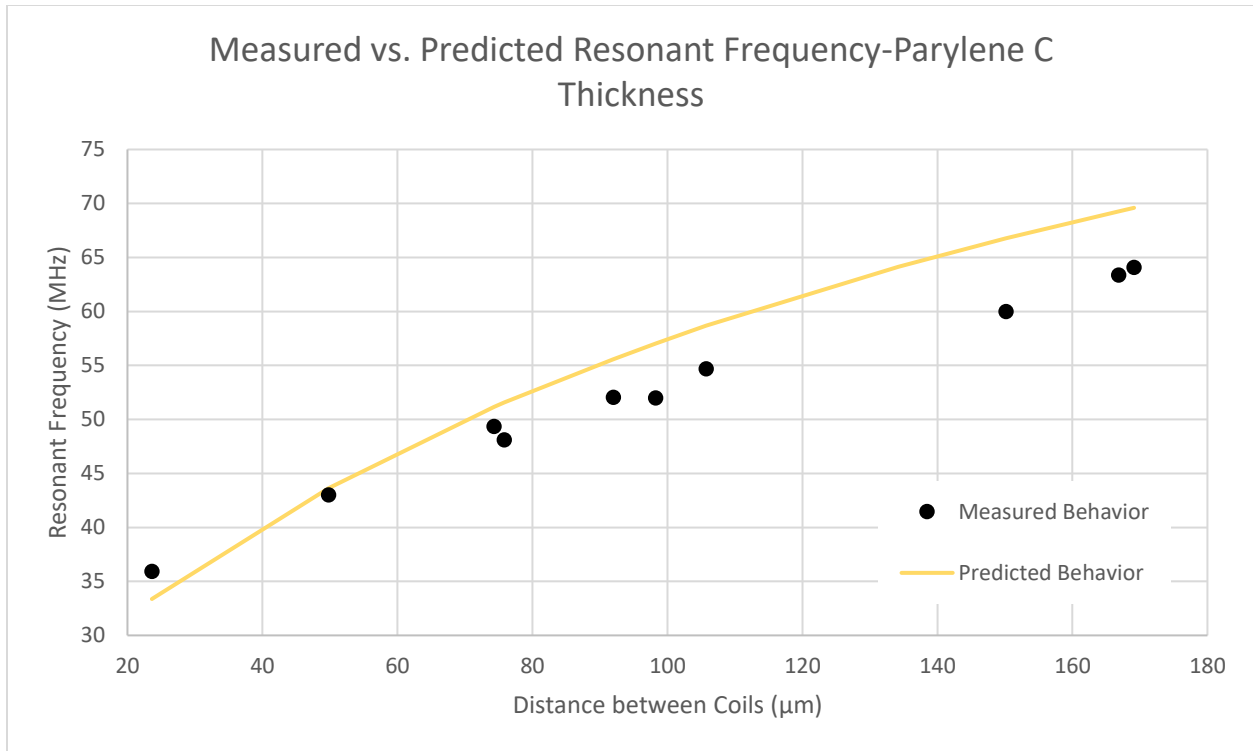


Figure 71: All eleven parylene C G3D15 sensors are measured and plotted to build a frequency-parylene C thickness curve.

The total parylene C thickness range was 23.6-169.1 μm. The R^2 value for the predicted curve was 0.89, and RMSE was 4.32 MHz between the two curves. The mean error between the measured and predicted data was 6.78%. The model could predict the resonant and physical behavior of parylene C force sensors to within a 10% error over a wide range of intervening layer thicknesses.

9.7.2 Analysis of Varying Thickness Sensors

The only variable geometric parameter between these sensors was the intervening layer thickness. The model accurately predicted a solid sensor's resonant frequency within 10% error, so establishing this frequency-intervening layer thickness relationship removed sensitivity uncertainties attributable to experimental protocol and sensor fabrication, such as non-parallelism. The 0.89 R^2 value indicated that there may still be some other manufacturing uncertainties present,

or that the model could still be improved. The measured data did not follow the expected asymptotic-logarithmic frequency trend of a passive resonant sensor, reaffirming concerns with manufacturing. Conversely, the predicted curve crossed the measured data at approximately 43 MHz and diverged at higher thicknesses. This trend could be indicative of unaccounted electrical behavior in solid sensors. Despite these sources of error, the model predicted solid sensor resonant frequency within a 10% error, and it could reasonably predict frequency-load behavior of wireless, passive force sensors.

Successful modeling of a large range of intervening thicknesses plus a wide array of geometries indicates the model will prove a useful tool in developing and understanding wireless, passive resonant force sensors. Accurate modeling of coil and air sensor behavior validates the predictive accuracy of a force sensor's resonant frequency. The results from the solid sensors indicate that the manufactured sensors will function effectively as force sensors in the previously defined design space of a smart cervical interbody implant.

10. DISCUSSION

10.1 Implications of Modeling Resonant Sensor Behavior

10.1.1 Passive Resonant Force Sensor Physics

The analytical model provides a detailed breakdown of sensor electrical behavior using only geometric parameters and known material properties. A detailed understanding of capacitances and inductances at the individual coil and mutual sensor level gives insight into minute changes in sensor behavior in response to changes in input parameters. This approach allows for the design and iteration of resonating coils and sensors that are tailored to specific applications, such as their use in smart implants. This geometric approach also allows the model of our sensors to be adapted to other types of sensors. This includes wireless, passive resonant sensing of physiologically relevant parameters such as multi-axial forces, pressures, temperature, pH, and strains. The only change required in the model is determining how intervening layer deformation responds to a measurand.

The model determines the resultant deformation in a sensor's intervening layer in response to an applied load. This deformation is then applied to the calculations of electrical behavior, changing the expected inductance and capacitance. The resonant frequency then changes as a result of these changes in inductance and capacitance.

10.1.2 Model Iteration and Refinement

The sensor model is based on known resonant RLC circuit behavior and antenna theory, but it is adapted and heavily modified to accurately model passive resonant force sensors in a physiologically relevant setting. The surrounding environment of the sensors is assumed to be heterogenous, and multiple candidate materials and resonant sensor configurations require that the model can represent these variable sensor environments. Fully modeling parasitic capacitances via

the full sensor layer stack method allows for precise calculations of the effects of the sensor's environment on its electrical behavior. Additionally, incorporating a wide array of geometries in sensor design in the model requires tweaks to electrical calculations as certain geometric values are approached, such as the effective permittivity adjustment for mutual capacitance. The capacitive interactions between the coil traces and the intervening layer are considered for the total effective permittivity between the two coils, but only if the trace height to intervening layer thickness exceeds a ratio of 0.2. Also, if the ratio of trace width to trace spacing exceeds three, the coil inductance approximation method in Equation 6 supersedes the other in Equation 7. These conditionals ensure that the model can overcome geometric limitations for certain calculations, allowing for prediction of resonant frequencies in sensors across a wide array of geometric parameters. Specific manufacturing methods are considered in the model. A sensor with a thin ($< 100 \mu\text{m}$) intervening layer has different mechanical calculations than a sensor with a thick intervening layer. Conformal intervening layers complicate area inputs for stress-strain calculations, as the two coated coils comprising the sensor do not uniformly contact each other. Therefore, the mechanical area is assessed the same way as the overlapping electrical trace area, where only the intersecting areas of traces are considered for stress-strain calculations.

10.1.3 Improvements and Future Work

A limitation of the model is its inability to accurately predict the behavior of coils and subsequently sensors with a low number of turns due to limitations in individual coil inductance approximations. Alternative approaches to approximating inductances of large diameter, large trace coils with a low number of turns could expand the model's capabilities.

The model also makes key assumptions about coil alignment that may not be reflective of actual sensor conditions. The model could be improved if it incorporated error estimations for

misaligned coils. The inductance and capacitance approximations are capable of accounting for misalignment, but the challenge lies in properly quantifying the average misalignment of an air or solid sensor. Errors from non-parallel coils within the sensor also contribute to overall frequency prediction errors. Coil and inductance approximation methods in the model, however, currently cannot account for non-parallel coil interactions. Additionally, like misalignment, the average degree of non-parallelism is challenging to quantify. Therefore, model validation depends on good, accurate manufacturing practices.

10.1.4 Significance and Translation

We developed an analytical model for predicting the frequency behavior of wireless, passive resonant force sensors and their constituent coils. The model details each electrical calculation that goes into resonant frequency calculations, allowing it to be broken down and adapted to other passive resonator applications.

The model is a tool for designing, prototyping, and iterating solid force sensors that are used in smart orthopedic applications. More specifically, the model provides the framework for designing sensors for a smart cervical interbody implant for future *in vitro* and *in vivo* applications.

10.2 Implications of Rapid Prototyping of Force Sensors

10.2.1 Sensor Design Constraints

Larger sensors are easier to read due to their lower resonant frequency and higher signal quality, but smaller sensors are more applicable to use in smart implants. Therefore, a parametric study was employed for two purposes. First, it determined the performance of an array of sensor designs, including sensors made with minimal geometric sizes and sensors with larger geometry, to stress the model and ensure that it could accurately predict the resonant frequency behavior across the entire selected range of geometric values. Second, this parametric study included

designs that were appropriate for incorporation into a modified cervical interbody implant. Design parameters were selected such that these sensors could achieve a 68 MHz resonant frequency with an intervening layer thickness that remained within the sensor design constraints.

Force sensor design and manufacture is highly dependent upon the expected range of physiologically relevant loads. Given available information regarding cervical compressive loads, the ideal intervening layer material is sensitive enough to deform under a 0-500 N load and withstands a peak 1000 N load. It also has a high dielectric constant to facilitate strong mutual inductive and capacitive interactions. The ideal material has a uniform profile to ensure parallelism between coils within a sensor and maintain consistent, predictable frequency behavior as it deforms. Additionally, successful model validation depends on use of an intervening material with consistent material properties, eliminating manufacture of heterogeneous materials such as thermosets with curing agents. Model validation also depends on the ability to accurately control intervening layer thickness, as knowing exact sensor geometric parameters is critical to accurate resonant frequency prediction. Given these constraints, parylene C was selected as the intervening material for use in force sensors designed for smart cervical interbody implants.

10.2.2 PCB Fabrication Methods

PCB coils have material properties suitable for force sensor applications. FR4, a common substrate used in printed circuit boards, has a much higher modulus than parylene C at 14 to 22 GPa, depending on the manufacturer. It also has a high dielectric constant appropriate for use in everyday circuitry. FR4 is significantly easier to modify for iterating smart implant designs than equivalent high dielectric materials such as glass. FR4, however, is limited to model validation and *in vitro* applications, as its biocompatibility is not established.

PCB coil fabrication methods are well established in industry and research. The abundant number of resources for board design enable rapid design and prototyping of coils. Design tools such as EAGLE streamline the board design process, making iteration of new designs simple. PCB manufacturers accept schematics from these design tools and quickly turn around manufacturing guidance for PCB design. Following final design submission, boards are made via single layer etches of copper coated FR4 substrates. The etching technique itself is inexpensive, and it can be done in batches. Established manufacturing techniques make PCB-based coils an attractive option for rapid, inexpensive prototyping of force sensors.

10.2.3 Modified Parylene C Deposition

The parylene C deposition protocol was modified to allow for thicker layer depositions, theoretically increasing uniformity by avoiding multiple, smaller layer depositions. Additionally, thicker depositions allow for a wider range of force sensor designs, as they can be made with intervening layers ranging from 10 μm to 170 μm , drastically altering resonant behavior. This modified protocol enables rapid force sensor prototyping, as running multiple deposition processes for a single desired thickness is resource and time intensive. Slowly stepping up parylene C dimer evaporation temperatures from 100° C to 180° C slows the flow of parylene passing through the pyrolysis and deposition chambers, allowing more parylene C to polymerize into a film on a sample.

However, unexpected issues with manufacturing quality arose with this modified process. There are no documented examples of thick parylene C layers (> 100 μm), so insight into material properties and deposition quality is limited. SEM imaging of parylene deposition quality showed that significant defects were present in single deposition parylene C layers exceeding 50 μm . These defects were likely the cause for several subsequent manufacturing issues, such as non-parallelism

between coils comprising force sensors. Non-uniformity resulting from these defects also exacerbates voids, or “air gaps”, in annealed parylene C layers. These factors may have contributed to shifts in resonant frequency that were not accounted for in the analytical model. Despite these challenges, parylene C remains a suitable candidate for wireless, passive resonant force sensors used in smart spinal implants.

10.2.4 Improvements and Future Work

Parylene C is the ideal mechanical material for force sensors, but its electrical properties can be improved to raise its dielectric constant. Parylene C can be doped by creating an organic-inorganic composite of parylene C and SiO₂, increasing its dielectric constant from 2.95 to approximately 3.5 [109]. Raising the relative permittivity of the intervening layer lowers the resultant sensor resonant frequency. Lowering the resonant frequency would enable smaller sensor designs. Smaller sensor designs are highly desirable in smart implants, as they reduce the amount of modification needed for existing implant designs.

Additionally, irregularities and non-uniformities in thick parylene C depositions can be reduced by improving annealing protocols. The ability to evenly heat and pressure the entire coil surface would reduce coil non-parallelism within sensors. Die bonding the coils under a vacuum would increase reflow, improving uniformity and reducing air gaps between traces. Alternatively, microwave annealing can fuse separate parylene C layers at lower temperatures than the current annealing protocol, increasing the number of candidate substrates for coil fabrication. Less air gaps between traces also result from this annealing method [107].

10.2.5 Significance and Translation

PCB-based manufacture enables rapid prototyping of force sensors for iteration and testing for smart implants. It also enables quick, simple, and inexpensive fabrication of an array of high-quality force sensors for model validation.

10.3 Implications of Accurate Predictability of Resonant Force Sensors

10.3.1 Coil Model Validation

The analytical model accurately predicts coil behavior across a wide range of geometries (8-26 mm outer diameter, 0-14 mm inner diameter, and 50-485 μm trace width and spacing). The model also handles changes in substrate material and geometric properties, as evidenced by the Borofloat and different types of FR4 composing various coil designs.

10.3.2 Air Sensor Model Validation

Coils were paired and placed on a specialized fixture that could hold both an antenna and the paired coils of interest. A mechanical test system stepped the coils apart up to 1000 μm . First-generation air sensor predictions averaged an R^2 of 0.65. Second-generation air sensors averaged an R^2 of 0.63 (G2D1 had a difficult to predict curve at a very low R^2 of 0.22). Third-generation air sensors averaged an R^2 of 0.99. This improvement in curve fit is likely due to improvements in alignment and manufacturing methods. The center and corner drill-holes built into second and third generation coils as well as the added alignment holes in the alumina silicate fixtures facilitated easier air sensor alignment. Third generation air coils differed slightly by placing the coils aligned and in contact with each other on the inferior fixture prior to attaching the superior coil to the superior fixture. Overall, the analytical model reasonably predicted air sensor behavior between 50 and 1000 microns, provided that experimental protocol was well controlled and

consistent. Displacement between 0 and 50 μm were still difficult to resolve, even with a high precision extensometer measuring displacements.

10.3.3 Solid Sensor Model Validation

A mechanical test system applied an axial compressive load, and changes in the resonant frequency were measured in real time in response to the load. Most solid sensor frequencies were accurately predicted to within 10% error, even with uncertainties surrounding manufacturing consistency. Measured sensor sensitivity (F_0 - F slopes) was within the same order of magnitude as the predicted slopes. Measured sensitivities ranged from 1.5x to 6x greater than the predicted sensitivities. More importantly, all solid sensors had measurable changes in frequency over a 500 N applied load. The net shift in frequency averaged 1.02 MHz for first-generation sensors, 0.74 MHz for second-generation sensors, and 0.28 MHz for third-generation sensors after removing the 0-50 N applied loads. Keeping the 0-50 N response resulted in a higher net shift in frequency, but the response was not linear if these values were included.

The network analyzer reliably resolves kHz range shifts in resonant frequency, so the sensors were easily capable of resolving ± 1 N changes in load. Given uncertainties in the non-linear response of the solid sensors to an applied load, a set of sensors with the same geometric parameters apart from intervening layer thickness were fabricated.

Sensors built with varying thicknesses of a single design emulated sensor deformation over a much larger range than the standard micron/submicron strain found in a single sensor compressed to 500 N. The analytical model succeeded in predicting solid sensor behavior over a large range of intervening thicknesses (30-160 μm)

10.3.4 Improvements and Future Work

A key improvement in model validation will come from eliminating uncertainties at small displacements in air and solid sensors. These uncertainties may result from limits in mechanical testing equipment. It is challenging to measure high compressive loads while maintaining the ability to resolve the micron and sub-micron deformations that occur in the parylene C force sensors.

The linear behavior of parylene C under compression is also a major assumption. Studies of parylene C typically only address thin film properties [99], as thin films are the most common application of parylene C. The thick layers used in the force sensors are considered bulk materials that experience applied stresses and strains differently than a thin film would. Additionally, defects such as air gaps and contamination present in the annealed parylene C intervening layer could alter the expected mechanical properties of parylene C. Materials testing of bulk tensile and compressive moduli of annealed parylene C will provide a more reliable measure of relevant material properties, improving predictions for frequency-applied load behavior in parylene C force sensors.

10.3.5 Significance and Translation

The preceding analysis on coil and air sensor behavior validates the predictive accuracy of the force sensor's resonant frequency. The results from the solid sensors indicate that the manufactured sensors will function effectively as force sensors in the previously defined design space of a smart cervical interbody implant.

10.4 Overall Significance

This model can be used by researchers and engineers to build passive resonant force sensors for smart orthopedic implants. This tool enables fast and accurate design of a force sensor

that can be used to gain valuable data of musculoskeletal forces in the body. This data can be used to further iterate sensor and smart orthopedic implant designs to improve patient outcomes.

We developed techniques for rapid and inexpensive fabrication of passive resonant sensors. By creating high quality, functional sensors in a short period of time, smart implant development and testing is not limited by more restrictive sensor fabrication techniques such as microfabrication and hand-fabrication. As a result, these techniques reduce the time and cost of prototyping smart implants utilizing passive resonant sensor technology. Access to rapid prototyping techniques enable quicker testing and iteration of smart orthopedic implants, reducing the time needed to approach a final design that can be used for data acquisition and therapeutic purposes.

We successfully demonstrate real-time force sensing with rapidly prototyped, PCB-based, resonant force sensors designed via the model. The model successfully predicted the resultant coil and sensor designs' resonant behavior to within 10% error of the measured resonant behavior. Accurate resonant frequency prediction of force sensors designed with the model validate its usefulness as a tool to develop smart orthopedic implants. This predictive model will be a useful tool for medical researchers and engineers to determine whether their smart orthopedic implants utilizing these novel wireless, passive, resonant force sensors will function as desired.

11. CONCLUSION

We have built a predictive model for wireless, passive, resonant force sensor behavior that can be used as a tool to rapidly design, develop, and iterate force sensors for various smart orthopedic implant applications. More specifically, it succeeds in predicting the behavior of passive resonant force sensors designed for use in a smart cervical interbody implant. The model was validated through extensive testing of printed circuit board (PCB) and microfabricated coils, paired PCB “air sensors”, and PCB force sensors across a wide range of geometries.

We have also developed a rapid prototyping and fabrication protocol for coil and sensor development. PCB-based manufacturing produces high quality, easily measurable sensors quickly and inexpensively. PCB coils are reliable and are excellent candidates for force sensors due to their mechanical and electrical properties. Parylene C is the functional intervening layer between the coils that allows the entire sensor structure to measure forces. Parylene C deforms in response to the physiologically relevant loads in the cervical spine, and its unique deposition process makes it an excellent candidate for force sensor model validation.

Instrumenting interbody implants with wireless, passive, resonant sensors is a novel approach to measuring forces in the lower cervical spine. This force sensor model also provides the framework for future approaches to measuring *in vivo* forces in the lower cervical spine. This *in vivo* force data can improve biomechanical models that elucidate the mechanical factors that cause DDD and ultimately debilitating neck pain. *In vivo* data will inform further optimizations of cervical fusion implants and improve patient outcomes.

REFERENCES

- [1] “Human Anatomy and Physiology Lab (BSB 141): The Vertebral Column.” Lumen Learning Web site. <https://courses.lumenlearning.com/ap1x94x1/chapter/the-vertebral-column/>. (accessed June 16, 2020).
- [2] A. White and M. Panjabi, *Clinical Biomechanics of the Spine. 2nd ed.* Philadelphia, PA, USA: J.B. Lippincott Company, 1990.
- [3] H. Carter and H. Gray. *Gray’s Anatomy: The Anatomical Basis of Clinical Practice.* 41st ed. S. Standring. London, UK: Elsevier Churchill, 2015.
- [4] S. Roberts *et al.*, “Histology and pathology of the human intervertebral disc,” *J. Bone Joint Surg. Am.*, vol. 88-A, no. suppl 2, pp. 10–14, Apr. 2006, doi: 10.2106/JBJS.F.00019.
- [5] L. J. Smith, N. L. Nerurkar, K. S. Choi, B. D. Harfe, and D. M. Elliott, “Degeneration and regeneration of the intervertebral disc: Lessons from development,” *Dis. Model. Mech.*, vol. 4, no. 1, pp. 31–41, Jan. 2011, doi: 10.1242/dmm.006403.
- [6] P. P. Raj, “Intervertebral disc: Anatomy-physiology-pathophysiology-treatment,” *Pain Pract.*, vol. 8, no. 1, pp. 18–44, Apr. 2008, doi: 10.1111/j.1533-2500.2007.00171.x.

- [7] S. J. Edmondston and K. P. Singer, “Thoracic spine: anatomical and biomechanical considerations for manual therapy,” *Man. Ther.*, vol. 2, no. 3. pp. 132–143, Aug. 1997, doi: 10.1054/math.1997.0293.
- [8] C. J. Snijders, G. A. Hoek van Dijke, and E. R. Roosch, “A biomechanical model for the analysis of the cervical spine in static postures,” *J. Biomech.*, vol. 24, no. 9, pp. 783–792, Apr. 1991, doi: 10.1016/0021-9290(91)90303-5.
- [9] H. Choi and R. Vanderby Jr., “Comparison of biomechanical human neck models: Muscle forces and spinal loads at C4/5 level,” *J. Appl. Biomech.*, vol. 15, no. 2. pp. 120–138, Jan. 1999, doi: 10.1123/jab.15.2.120.
- [10] K. J. Netto, A. F. Burnett, J. P. Green, and J. P. Rodrigues, “Validation of an EMG-driven, graphically based isometric musculoskeletal model of the cervical spine,” *J. Biomech. Eng.*, vol. 130, no. 3, Jun. 2008, doi: 10.1115/1.2913234.
- [11] Y. H. Kim, B. Khuyagbaatar, and K. Kim, “Recent advances in finite element modeling of the human cervical spine,” *J. Mech. Sci. Technol.*, vol. 32, no. 1, pp. 1–10, Jan. 2018, doi: 10.1007/s12206-017-1201-2.
- [12] V. K. Goel, C. R. Clark, D. McGowan, and S. Goyal, “An in-vitro study of the kinematics of the normal, injured and stabilized cervical spine,” *J. Biomech.*, vol. 17, no. 5, pp. 363–376, 1984, doi: 10.1016/0021-9290(84)90030-7.

- [13] M. M. Panjabi, T. Miura, P. A. Crip-ton, J. L. Wang, A. S. Nain, and C. DuBois, “Development of a system for in vitro neck muscle force replication in whole cervical spine experiments.,” *Spine*, vol. 26, no. 20, pp. 2214–2219, 2001, doi: 10.1097/00007632-200110150-00012.
- [14] D. J. DiAngelo and K. T. Foley, “An improved biomechanical testing protocol for evaluating spinal arthroplasty and motion preservation devices in a multilevel human cadaveric cervical model.,” *Neurosurg. Focus*, vol. 17, no. 3, p. 22-29, Sep. 2004, doi: 10.3171/foc.2004.17.3.4.
- [15] A. G. Hadjipavlou, M. N. Tzermiadianos, N. Bogduk, and M. R. Zindrick, “The pathophysiology of disc degeneration: A CRITICAL REVIEW,” *J. Bone Jt. Surg. - Br. Vol.*, vol. 90-B, no. 10, pp. 1261–1270, Oct. 2008, doi: 10.1302/0301-620X.90B10.20910.
- [16] M. A. Adams, B. J. C. Freeman, H. P. Morrison, I. W. Nelson, and P. Dolan, “Mechanical initiation of intervertebral disc degeneration,” *Spine*, vol. 25, no. 13, pp. 1625–1636, 2000, doi: 10.1097/00007632-200007010-00005.
- [17] J. A. Iorio, A. M. Jakoi, and A. Singla, “Biomechanics of degenerative spinal disorders,” *Asian Spine J.*, vol. 10, no. 2, pp. 377–384, 2016, doi: 10.4184/asj.2016.10.2.377.

- [18] A. I. Binder, “Cervical spondylosis and neck pain,” *Br. Med. J.*, vol. 334, no. 7592, pp. 527–531, Mar. 2007, doi: 10.1136/bmj.39127.608299.80.
- [19] M. Bernhardt, R. A. Hynes, H. W. Blume, and A. A. White III, “Cervical spondylotic myelopathy,” *J. Bone Jt. Surg.*, vol. 75-A, no. 1, pp. 119–128, Jan. 1993, doi: 10.2106/00004623-199301000-00016.
- [20] M. A. Adams and P. Dolan, “Spine biomechanics,” *J. Biomech.*, vol. 38, no. 10, pp. 1972–1983, Oct. 2005, doi: 10.1016/j.jbiomech.2005.03.028.
- [21] GBD 2015 SDG Collaborators, “Global, regional, and national comparative risk assessment of 79 behavioural, environmental and occupational, and metabolic risks or clusters of risks, 1990–2015: a systematic analysis for the Global Burden of Disease Study 2015,” *Lancet*, vol. 388, pp. 1659–1724, Oct. 2016, doi: 10.1016/S0140-6736(16)31679-8.
- [22] D. G. Hoy, M. Protani, R. De, and R. Buchbinder, “The epidemiology of neck pain,” *Best Pract. Res. Clin. Rheumatol.*, vol. 24, no. 6, pp. 783–792, Dec. 2010, doi: 10.1016/j.berh.2011.01.019.
- [23] S. Hogg-Johnson *et al.*, “The burden and determinants of neck pain in the general population. Results of the Bone and Joint Decade 2000-2010 Task Force on Neck Pain and Its Associated Disorders,” *J. Manipulative Physiol. Ther.*, vol. 32, no. 2S., pp. S46–S60, 2009, doi: 10.1016/j.jmpt.2008.11.010.

- [24] J. Guzman *et al.*, “A new conceptual model of neck pain. Linking onset, course, and care: The Bone and Joint Decade 2000-2010 Task Force on Neck Pain and Its Associated Disorders,” *J. Manipulative Physiol. Ther.*, vol. 32, no. 2S., pp. S17–S28, Feb. 2009, doi: 10.1016/j.jmpt.2008.11.007.
- [25] M. Van Middelkoop *et al.*, “Surgery versus conservative care for neck pain: A systematic review,” *Eur. Spine J.*, vol. 22, no. 1, pp. 87–95, Jan. 2013, doi: 10.1007/s00586-012-2553-z.
- [26] H. N. Herkowitz, “A comparison of anterior cervical fusion, cervical laminectomy, and cervical laminoplasty for the surgical management of multiple level spondylotic radiculopathy,” *Spine*, vol. 13, no. 7, pp. 774–780, Jul. 1988, doi: 10.1097/00007632-198807000-00011.
- [27] M. Palit *et al.*, “Anterior discectomy and fusion for the management of neck pain,” *Spine*, vol. 24, no. 21, pp. 2224–2228, Nov. 1999, doi: 10.1097/00007632-199911010-00009.
- [28] K. K. Kani and F. S. Chew, “Anterior cervical discectomy and fusion: review and update for radiologists,” *Skeletal Radiol.*, vol. 47, no. 1, pp. 7–17, Jan. 2018, doi: 10.1007/s00256-017-2798-z.
- [29] G. Matgé, “Cervical cage fusion with 5 different implants: 250 Cases,” *Acta Neurochir. (Wien)*, vol. 144, no. 6, pp. 539–550, Jun. 2002, doi: 10.1007/s00701-002-0939-0.

- [30] M. J. Lee, R. Bazaz, C. G. Furey, and J. Yoo, “Influence of anterior cervical plate design on dysphagia: A 2-year prospective longitudinal follow-up study,” *J. Spinal Disord. Tech.*, vol. 18, no. 5, pp. 406–409, Oct. 2005, doi: 10.1097/01.bsd.0000177211.44960.71.
- [31] S. M. Perren, “Evolution of the internal fixation of long bone fractures: The scientific basis of biological internal fixation: choosing a new balance between stability and biology,” *J. Bone Jt. Surg.*, vol. 84, no. 8, pp. 1093–1110, Nov. 2002, doi: 10.1302/0301-620X.84B8.13752.
- [32] E. C. Benzel, L. Gilbertson, and R. A. Mericle, “Enhancing spinal fusion,” *Clin. Neurosurg.*, vol. 55, pp. 63–71, 2008, doi: 10.1227/01.neu.0000333429.28626.28.
- [33] J. M. Peterson *et al.*, “Stiffness matters: Part II - The effects of plate stiffness on load-sharing and the progression of fusion following ACDF in vivo,” *Spine (Phila. Pa. 1976)*, vol. 43, no. 18, pp. E1069–E1076, Sep. 2018, doi: 10.1097/BRS.0000000000002644.
- [34] R. C. Sasso and N. M. Best, “Cervical kinematics after fusion and bryan disc arthroplasty,” *J. Spinal Disord. Tech.*, vol. 21, no. 1, pp. 19–22, Feb. 2008, doi: 10.1097/BSD.0b013e3180500778.
- [35] J. Cegoñino, A. Calvo-Echenique, and A. Pérez-Del Palomar, “Influence of different fusion techniques in lumbar spine over the adjacent segments: A 3D finite element study,” *J. Orthop. Res.*, vol. 33, no. 7, pp. 993–1000, Jul. 2015, doi: 10.1002/jor.22854.

- [36] F. Burny *et al.*, “Concept, design and fabrication of smart orthopedic implants,” *Med. Eng. Phys.*, vol. 22, no. 7, pp. 469–479, Sep. 2000, doi: 10.1016/S1350-4533(00)00062-X.
- [37] E. H. Ledet, B. Liddle, K. Kradinova, and S. Harper, “Smart implants in orthopedic surgery, improving patient outcomes: a review,” *Innov. Entrep. Health*, vol. 5, pp. 41–51, Sep. 2018, doi: 10.2147/IEH.S133518.
- [38] S. S. Karipott, B. D. Nelson, R. E. Guldberg, and K. G. Ong, “Clinical potential of implantable wireless sensors for orthopedic treatments,” *Expert Rev. Med. Devices*, vol. 15, no. 4, pp. 255–264, Apr. 2018, doi: 10.1080/17434440.2018.1454310.
- [39] T. R. Waugh, “Intravital measurements during instrumental correction of idiopathic scoliosis,” *Acta Orthop. Scand.*, vol. suppl-93, pp. 1-87, 1966, doi: 10.3109/ort.1966.37.suppl-93.01.
- [40] A. Rohlmann, G. Bergmann, and F. Graichen, “A spinal fixation device for in vivo load measurement,” *J. Biomech.*, vol. 27, no. 7, pp. 961–967, Jul. 1994, doi: 10.1016/0021-9290(94)90268-2.
- [41] A. Rohlmann, F. Graichen, U. Weber, and G. Bergmann, “Monitoring in vivo implant loads with a telemeterized internal spinal fixation device,” *Spine (Phila. Pa. 1976)*, vol. 25, no. 23, pp. 2981–2986, Dec. 2000, doi: 10.1097/00007632-200012010-00004.

- [42] A. Rohlmann, U. Gabel, F. Graichen, A. Bender, and G. Bergmann, “An instrumented implant for vertebral body replacement that measures loads in the anterior spinal column,” *Med. Eng. Phys.*, vol. 29, no. 5, pp. 580–585, Jun. 2007, doi: 10.1016/j.medengphy.2006.06.012.
- [43] A. Rohlmann *et al.*, “Activities of everyday life with high spinal loads,” *PLoS One*, vol. 9, no. 5, pp. 1–9, 2014, doi: 10.1371/journal.pone.0098510.
- [44] E. H. Ledet, M. P. Tymeson, D. J. DiRisio, B. Cohen, and R. L. Uhl, “Direct real-time measurement of in vivo forces in the lumbar spine,” *Spine J.*, vol. 5, no. 1, pp. 85–94, Jan. 2005, doi: 10.1016/j.spinee.2004.06.017.
- [45] D. S. Munro, A. R. Lingley, E. C. Tsai, and M. T. Khbeis, “Development of a microfabricated sensor system to measure lumbar spinal fusion,” *ASME Int. Mech. Eng. Congr. Expo. Proc.*, vol. 3, pp. 1–7, 2016, doi: 10.1115/IMECE2016-65703.
- [46] “Resonance in Series RLC Circuit.” Electrical4U Web Site. <https://www.electrical4u.com/resonance-in-series-rlc-circuit/>. (Accessed February 15th, 2020).
- [47] S. Ball. “Building a Digital Dip Meter.” Circuit Cellar Web Site. http://circuitcellar.com/wp-content/uploads/2013/01/CC25_ProjCard_Pres_Ball-CC271.pdf. (Accessed June 20th, 2019).

- [48] Makarov S. *Antenna and EM Modeling with MATLAB*. New York, NY, USA: Wiley-Interscience, 2002.
- [49] V. I. Slyusar, “60 years of electrically small antennas theory,” *2007 6th Int. Conf. Antenna Theory Tech. ICATT’07*, vol. i, pp. 116–118, Sep. 2007, doi: 10.1109/ICATT.2007.4425129.
- [50] C. C. Collins, “Miniature passive pressure transensor for implanting in the eye,” *IEEE Trans. Biomed. Eng.*, Vol. BME-14, no. 2, pp. 74–83, Apr. 1967, doi: 10.1109/TBME.1967.4502474.
- [51] M. A. Fonseca, M. G. Allen, J. Kroh, and J. White, “Flexible wireless passive pressure sensors for biomedical applicatons,” in *Solid-State Sensors, Actuators, Microsystems Work.*, Hilton Head Island, South Carolina, USA, 2005, pp. 37–42.
- [52] J. A. Potkay, “Long term, implantable blood pressure monitoring systems,” *Biomed. Microdevices*, vol. 10, no. 3, pp. 379–392, Jun. 2008, doi: 10.1007/s10544-007-9146-3.
- [53] P. J. Chen, S. Saati, R. Varma, M. S. Humayun, and Y. C. Tai, “Wireless intraocular pressure sensing using microfabricated minimally invasive flexible-coiled LC sensor implant,” *J. Microelectromechanical Syst.*, vol. 19, no. 4, pp. 721–734, Aug. 2010, doi: 10.1109/JMEMS.2010.2049825.

- [54] R. A. Wachs *et al.*, “Elementary implantable force sensor: For smart orthopaedic implants,” *Adv Biosens Bioelectron*, vol. 2, no. 4, Dec. 2013, doi: 10.1161/CIRCULATIONAHA.110.956839.
- [55] J. F. Drazan, T. M. Wassick, R. Dahle, L. A. Beardslee, N. C. Cady, and E. H. Ledet, “A simple sensing mechanism for wireless, passive pressure sensors,” presented at the *Proc. Annu. Int. Conf. IEEE Eng. Med. Biol. Soc. EMBS*, 2016, pp. 1890-1893, doi: 10.1109/EMBC.2016.7591090.
- [56] M. K. Dion *et al.*, “Smart orthopaedic implants: Applications in total knee arthroplasty,” *Am. J. Eng. Appl. Sci.*, vol. 9, no. 4, pp. 1232–1238, Dec. 2016, doi: 10.3844/ajeassp.2016.1232.1238.
- [57] E. H. Ledet, D. D’Lima, P. Westerhoff, J. A. Szivek, R. A. Wachs, and G. Bergmann, “Implantable sensor technology: From research to clinical practice,” *J. Am. Acad. Orthop. Surg.*, vol. 20, no. 6, pp. 383–392, Jun. 2012, doi: 10.5435/JAAOS-20-06-383.
- [58] J. Drazan, “An implantable wireless sensor for continuous monitoring of intracompartmental pressures,” Ph.D. dissertation, Dept. Biomed. Eng., Rensselaer Polytechnic Ins., Troy, NY, USA, 2017.
- [59] J. F. Drazan *et al.*, “Simple implantable wireless sensor platform to measure pressure and force,” *Med. Eng. Phys.*, vol. 59, pp. 1–7, Sep. 2018, doi: 10.1016/j.medengphy.2018.06.006.

- [60] C. M. Zierhofer and E. S. Hochmair, "Geometric approach for coupling enhancement of magnetically coupled coils," *IEEE Trans. Biomed. Eng.*, vol. 43, no. 7, pp. 708–714, Jul. 1996, doi: 10.1109/10.503178.
- [61] S. S. Mohan, M. D. M. Hershenson, S. P. Boyd, and T. H. Lee, "Simple accurate expressions for planar spiral inductances," *IEEE J. Solid-State Circuits*, vol. 34, no. 10, pp. 1419–1420, Oct. 1999, doi: 10.1109/4.792620.
- [62] U. M. Jow and M. Ghovanloo, "Modeling and optimization of printed spiral coils in air and muscle tissue environments," *IEEE Trans. Biomed. Circuits Syst.*, vol. 3, no. 5, pp. 339–347, Oct. 2009, doi: 10.1109/TBCAS.2009.2025366.
- [63] J. Olivo, S. Carrara and G. De Micheli, "Modeling of printed spiral inductors for remote powering of implantable biosensors", *Proc. 5th Int. Symp. Med. Inform. Commun. Technol. (ISMICT)*, 2011, pp. 29-32, doi: 10.1109/ISMICT.2011.5759790.
- [64] N. Shah, M. Etemadi, R. Kant, K. Goldman, and S. Roy, "Quality factor optimization of inductive antennas for implantable pressure sensors," *IEEE Sens. J.*, vol. 14, no. 8, pp. 2452–2460, Aug. 2014, doi: 10.1109/JSEN.2013.2285220.
- [65] I. J. Bahl. & R. Garg, "Simple and accurate formulas for a microstrip with finite strip thickness," *Proc. IEEE 65*, 1977, pp. 1611–1612, doi: 10.1109/PROC.1977.10783.

- [66] Q. Shi, J. Wang, D. Chen, and J. Chen, “In vitro and in vivo characterization of wireless and power-free micro platform enabling gastrointestinal pressure,” *Biomed. Microdevices*, vol. 16, no. 6, pp. 859–868, Dec. 2014, doi: 10.1007/s10544-014-9890-0.
- [67] S. H. Tan, E. C. Teo, and H. C. Chua, “Quantitative three-dimensional anatomy of cervical, thoracic and lumbar vertebrae of Chinese Singaporeans,” *Eur. Spine J.*, vol. 13, no. 2, pp. 137–146, Mar. 2004, doi: 10.1007/s00586-003-0586-z.
- [68] J. Bazaldúa Cruz *et al.*, “Morphometric study of cervical vertebrae C3-C7 in a population from northeastern Mexico,” *Int. J. Morphol.*, vol. 29, no. 2, pp. 325–330, Jun. 2011, doi: 10.4067/S0717-95022011000200003.
- [69] S. P. Moroney, A. B. Schultz, J. A. A. Miller, and G. B. J. Andersson, “Load-displacement properties of lower cervical spine motion segments,” *J. Biomech.*, vol. 21, no. 9, pp. 769–779, 1988, doi: 10.1016/0021-9290(88)90285-0.
- [70] J. Lu, N. A. Ebraheim, H. Yang, J. Rollins, and R. A. Yeasting, “Anatomic bases for anterior spinal surgery: Surgical anatomy of the cervical vertebral body and disc space,” *Surg. Radiol. Anat.*, vol. 21, no. 4, pp. 235–239, 1999, doi: 10.1007/s00276-999-0235-2.

- [71] H. Choi and R. Vanderby Jr., “Comparison of biomechanical human neck models: Muscle forces and spinal loads at C4/5 level,” *J. of Appl. Biomech.*, vol. 15, no. 2, pp. 120–138, 1999, doi: 10.1123/jab.15.2.120.
- [72] M. Shea, W. T. T. Edwards, A. A. White, and W. C. C. Hayes, “Variations of stiffness and strength along the human cervical spine,” *J. Biomech.*, vol. 24, no. 2, pp. 95–107, 1991, doi: 10.1016/0021-9290(91)90354-P.
- [73] R. W. Nightingale, J. H. McElhaney, W. J. Richardson, and B. S. Myers, “Dynamic responses of the head and cervical spine to axial impact loading,” *J. Biomech.*, vol. 29, no. 3, pp. 307–318, Mar. 1996, doi: 10.1016/0021-9290(95)00056-9.
- [74] M. Dreischarf, A. Shirazi-Adl, N. Arjmand, A. Rohlmann, and H. Schmidt, “Estimation of loads on human lumbar spine: A review of in vivo and computational model studies,” *J. Biomech.*, vol. 49, no. 6, pp. 833–845, Apr. 2016, doi: 10.1016/j.jbiomech.2015.12.038.
- [75] H. S. Ahn and D. J. DiAngelo, “Biomechanical testing simulation of a cadaver spine specimen,” *Spine (Phila. Pa. 1976)*, vol. 32, no. 11, pp. E330–E336, May 2007, doi: 10.1097/01.brs.0000263331.78903.61.
- [76] S. P. Moroney, A. B. Schultz, and J. A. A. Miller, “Analysis and measurement of neck loads,” *J. Orthop. Res.*, vol. 6, no. 5, pp. 713–720, 1988, doi: 10.1002/jor.1100060514.

[77] T. Miura, M. M. Panjabi, and P. A. Crip-ton, “A method to simulate in vivo cervical spine kinematics using in vitro compressive preload,” *Spine (Phila. Pa. 1976).*, vol. 27, no. 1, pp. 43–48, Jan. 2002, doi: 10.1097/00007632-200201010-00011.

[78] S. J. Edmondston and K. P. Singer, “Thoracic spine: Anatomical and biomechanical considerations for manual therapy,” *Man. Ther.*, vol. 2, no. 3. pp. 132–143, Aug. 1997, doi: 10.1054/math.1997.0293.

[79] C. J. Snijders, G. A. Hoek van Dijke, and E. R. Roosch, “A biomechanical model for the analysis of the cervical spine in static postures,” *J. Biomech.*, vol. 24, no. 9, pp. 783–792, 1991, doi: 10.1016/0021-9290(91)90303-5.

[80] S. Kumaresan, N. Yoganandan, F. A. Pintar, and D. J. Maiman, “Finite element modeling of the cervical spine: Role of intervertebral disc under axial and eccentric loads,” *Med. Eng. Phys.*, vol. 21, no. 10, pp. 689–700, Dec. 1999, doi: 10.1016/S1350-4533(00)00002-3.

[81] K. Ono *et al.*, “Cervical vertebral motions and biomechanical responses to direct loading of human head,” *Traffic Inj. Prev.*, vol. 4, no. 2, pp. 141–152, Jun. 2003, doi: 10.1080/15389580309861.

[82] J. M. Peterson, C. Chlebek, A. M. Clough, A. K. Wells, and E. H. Ledet, “Stiffness matters: Part I - The effects of plate stiffness on the biomechanics of ACDF in vitro,” *Spine (Phila. Pa. 1976).*, vol. 43, no. 18, pp. E1061–E1068, Sep. 2018, doi: 10.1097/BRS.0000000000002643.

- [83] Y. Yan *et al.*, “In vitro evaluation of translating and rotating plates using a robot testing system under follower load,” *Eur. Spine J.*, vol. 26, no. 1, pp. 189–199, Jan. 2017, doi: 10.1007/s00586-015-4203-8.
- [84] *Industrial Laminating Thermosetting Products*, LI 1-1998, National Electrical Manufacturers Association, 1998.
- [85] D. Yan *et al.*, “Low-cost wireless temperature measurement: Design, manufacture, and testing of a PCB-based wireless passive temperature sensor,” *Sensors (Basel)*., vol. 18, no. 2, Feb. 2018, Art. no. 532, doi: 10.3390/s18020532.
- [86] W. Wu, Q. Wang, and W. Li, “Comparison of tensile and compressive properties of carbon/glass interlayer and intralayer hybrid composites,” *Materials (Basel)*., vol. 11, no. 7, Jun. 2018, Art. no. 1105, doi: 10.3390/ma11071105.
- [87] GA, “GA-170-LL/GA-170B-LL: Low Z-CTE Multi-functional epoxy resin CCL and prepreg,” GA-170-LL datasheet.
- [88] “Glass Epoxy (G-10, FR-4, G-11)”. Dielectric Manufacturing Web Site. <https://dielectricmfg.com/knowledge-base/glass-epoxy/>. (Accessed May 8th, 2019).

- [89] “G-Etronax EP FR4 Epoxy, Glass Fabric Reinforcement”. Matweb Web Site. <http://www.matweb.com/search/datasheettext.aspx?matguid=3f2d87c453014823ad3e591deb466024>. (Accessed May 8th, 2019).
- [90] Isola, “185HR Laminate and Prepreg,” 185HR datasheet.
- [91] US Food and Drug Administration, *Radio Frequency Wireless Technology in Medical Devices*. Rockville, MD, 2013.
- [92] M. K. Dion, “Analysis of intraoperative technique and its effect on loading patterns across the patellofemoral joint using a smart patellar implant,” Ph.D. dissertation, Dept. Biomed. Eng., Rensselaer Polytechnic Ins., Troy, NY, USA, 2017.
- [93] N. A. Pallotta, “An evaluation of polymers for the encapsulation of mechanically loaded in vivo sensors,” M.S. thesis, Dept. Biomed. Eng., Rensselaer Polytechnic Ins., Troy, NY, USA, 2009.
- [94] Y. Qin, M. M. R. Howlader, M. J. Deen, Y. M. Haddara, and P. R. Selvaganapathy, “Polymer integration for packaging of implantable sensors,” *Sensors Actuators, B Chem.*, vol. 202, no. 31, pp. 758–778, Oct. 2014, doi: 10.1016/j.snb.2014.05.063.

- [95] W. F. Gorham, "A new, general synthetic method for the preparation of linear poly-p-xylylenes," *J. Polym. Sci. Part A-1 Polym. Chem.*, vol. 4, no. 12, pp. 3027–3039, Dec. 1966, doi: 10.1002/pol.1966.150041209.
- [96] H. S. Kim and K. Najafi, "Wafer bonding using parylene and wafer-level transfer of free-standing parylene membranes," in *12th Intl. Conf. Solid State Sens., Act., and Microsys.*, 2003, pp. 790–793, doi: 10.1109/SENSOR.2003.1215592.
- [97] Specialty Coating Systems. "SCS Parylene Properties." <https://scscoatings.com/what-is-parylene/parylene-properties/>, 2017. (Accessed June 1, 2017).
- [98] C. Hassler, R. P. Von Metzen, P. Ruther, and T. Stieglitz, "Characterization of parylene C as an encapsulation material for implanted neural prostheses," *J. Biomed. Mater. Res. - Part B Appl. Biomater.*, vol. 93, no. 1, pp. 266–274, Apr. 2010, doi: 10.1002/jbm.b.31584.
- [99] T. A. Harder, T. J. Yao, Q. He, C. Y. Shih, and Y. C. Tai, "Residual stress in thin-film parylene-C," in *Proc. IEEE Micro Electro Mech. Syst.*, pp. 435–438, 2002, doi: 10.1109/memsys.2002.984296.
- [100] J. Lin, P. Deng, G. Lam, B. Lu, Y. Lee, and Y. Tai. "Creep of parylene C film," in *16th Intl. Solid-State Sens., Act. and Microsys. Conf.* Beijing, China, 2011, doi:10.1109/TRANSDUCERS.2011.5969483.

- [101] C. W. Tsao, L. Hromada, J. Liu, P. Kumar, and D. L. DeVoe, “Low temperature bonding of PMMA and COC microfluidic substrates using UV/ozone surface treatment,” *Lab Chip*, vol. 7, no. 4, pp. 499–505, Apr. 2007, doi: 10.1039/b618901f.
- [102] J. Charmet, J. Bitterli, O. Sereda, M. Liley, P. Renaud, and H. Keppner, “Optimizing parylene C adhesion for MEMS processes: Potassium hydroxide wet etching,” *J. Microelectromechanical Syst.*, vol. 22, no. 4, pp. 855–864, Aug. 2013, doi: 10.1109/JMEMS.2013.2248126.
- [103] J. Gao *et al.*, “Adhesion promoter for a multi-dielectric-layer on a digital microfluidic chip,” *RSC Adv.*, vol. 5, no. 60, pp. 48626–48630, May 2015, doi: 10.1039/c5ra08202a.
- [104] P. Kramer, A. K. Sharma, E. E. Hennecke, and H. Yasuda, “Polymerization of para-xylylene derivatives (parylene polymerization). I. Deposition kinetics for parylene N and parylene C,” *J. Polym. Sci. A1.*, vol. 22, no. 2, pp. 475–491, Feb. 1984, doi: 10.1002/pol.1984.170220218.
- [105] M. Gazicki-Lipman, “Vapor deposition polymerization of para-Xylylene derivatives - Mechanism and applications,” *J. Vac. Soc. Japan*, vol. 50, no. 10, pp. 601–608, 2007, doi: 10.3131/jvsj.50.601.
- [106] J. Ortigoza-Diaz *et al.*, “Techniques and considerations in the microfabrication of parylene c microelectromechanical systems,” *Micromachines (Basel)*, vol. 9, no. 9, Aug. 2018, Art. no. 422, doi: 10.3390/mi9090422.

[107] H. S. Noh, K. S. Moon, A. Cannon, P. J. Hesketh, and C. P. Wong, “Wafer bonding using microwave heating of parylene intermediate layers,” *J. Micromechanics Microengineering*, vol. 14, no. 4, pp. 625–631, Feb. 2004, doi: 10.1088/0960-1317/14/4/025.

[108] “Aluminum Silicon Oxide,” American Elements Web Site. <https://www.americanelements.com/aluminum-silicon-oxide-1302-93-8>. (Accessed March 4th, 2020).

[109] P. Tewari, R. Rajagopalan, E. Furman, and M. T. Lanagan, “Control of interfaces on electrical properties of SiO₂-Parylene-C laminar composite dielectrics,” *J. Colloid Interface Sci.*, vol. 332, no. 1, pp. 65–73, Apr. 2009, doi: 10.1016/j.jcis.2008.12.060.

APPENDICES

Appendix A Additional Figures

A.1 Gen 1 Air Sensor Figures

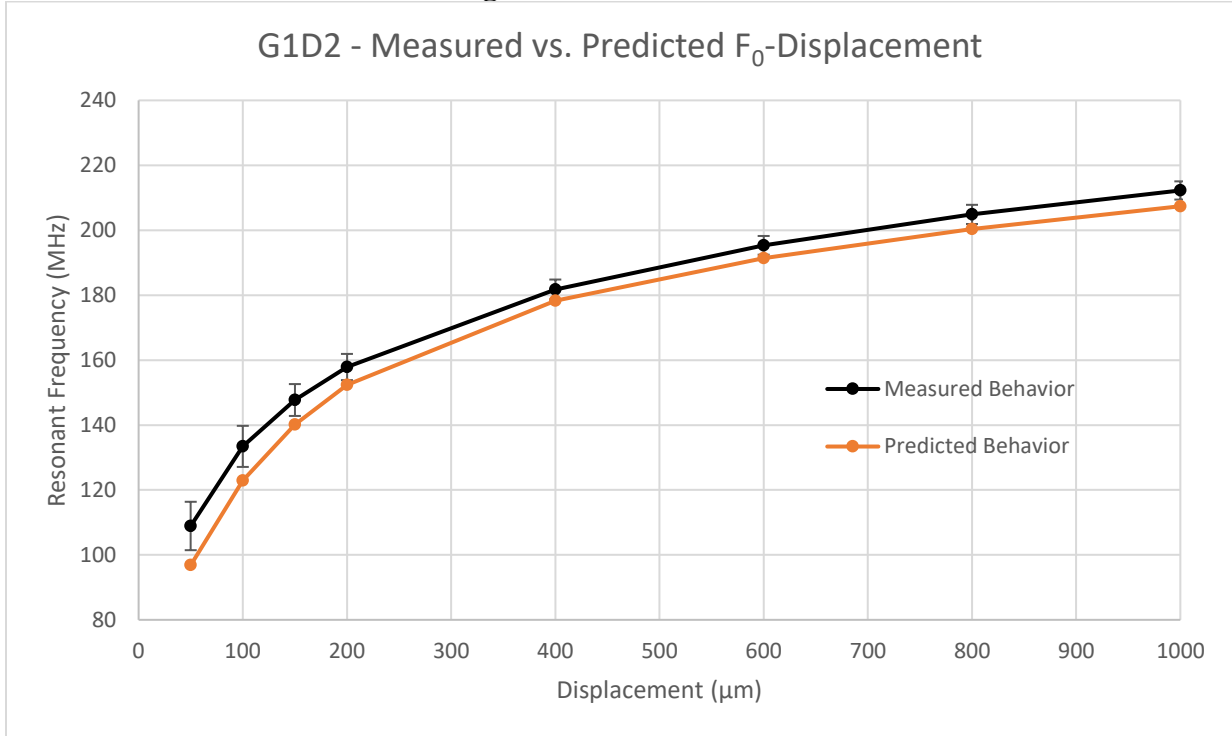


Figure 72: G1D2 air sensor. Error bars show one standard deviation based on three measurements.

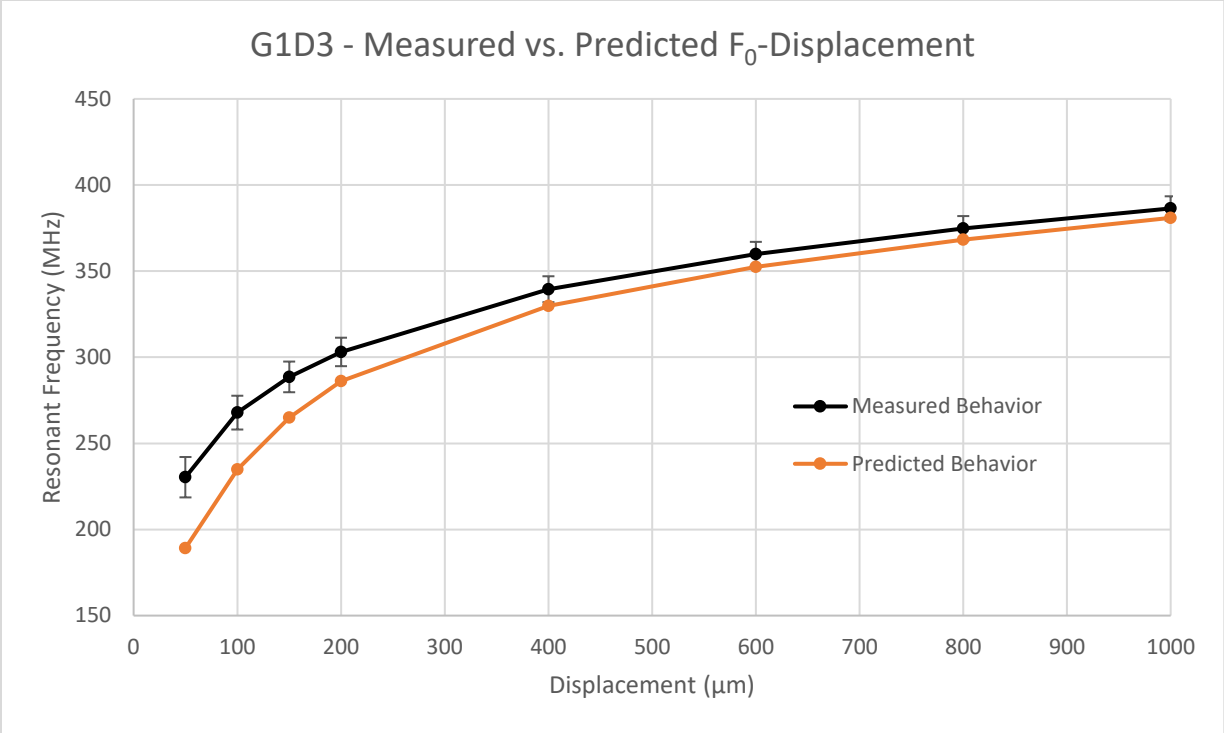


Figure 73: G1D3 air sensor. Error bars show one standard deviation based on three measurements.

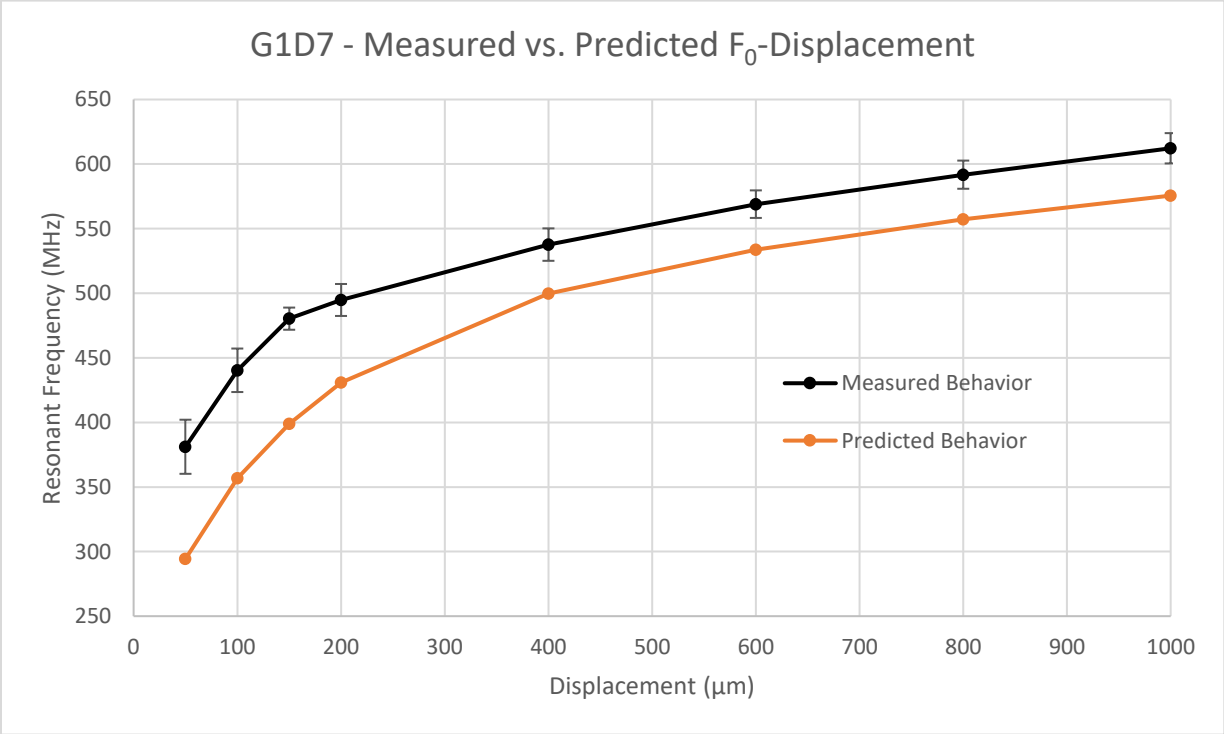


Figure 74: G1D7 air sensor. Error bars show one standard deviation based on three measurements.

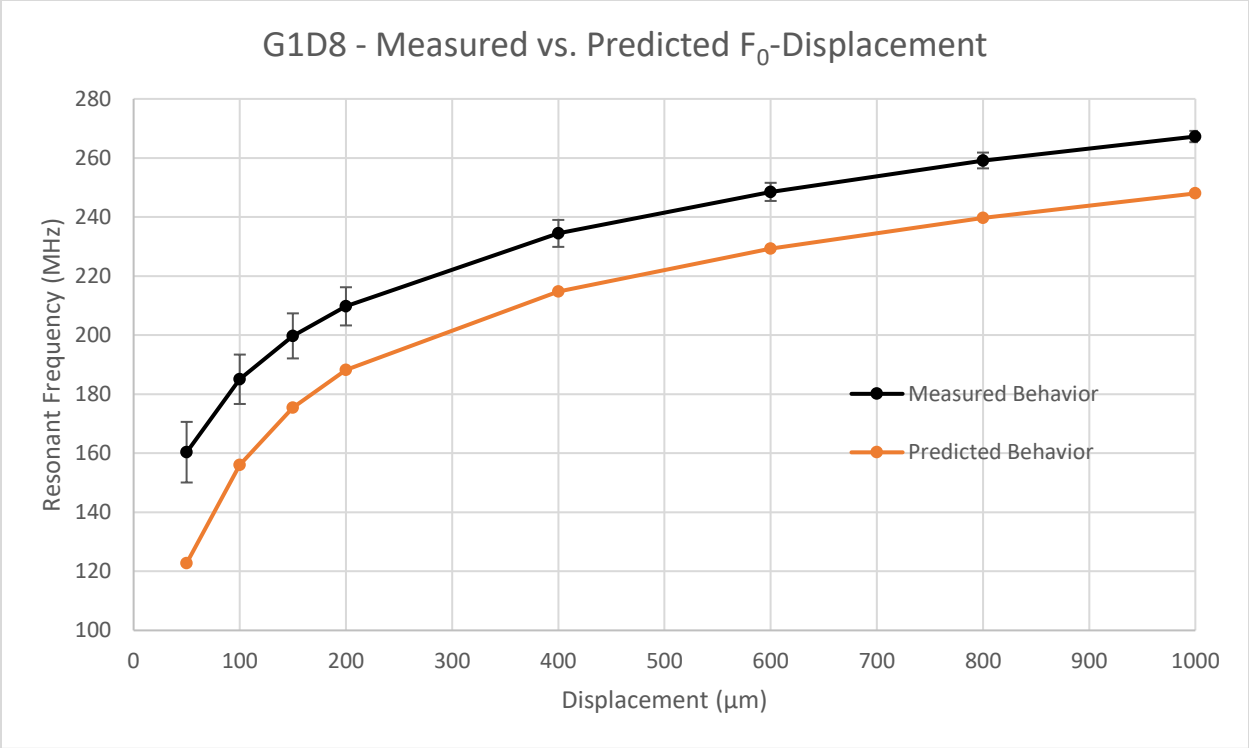


Figure 75: G1D8 air sensor. Error bars show one standard deviation based on three measurements.

A.2 Gen 2 Air Sensor Figures

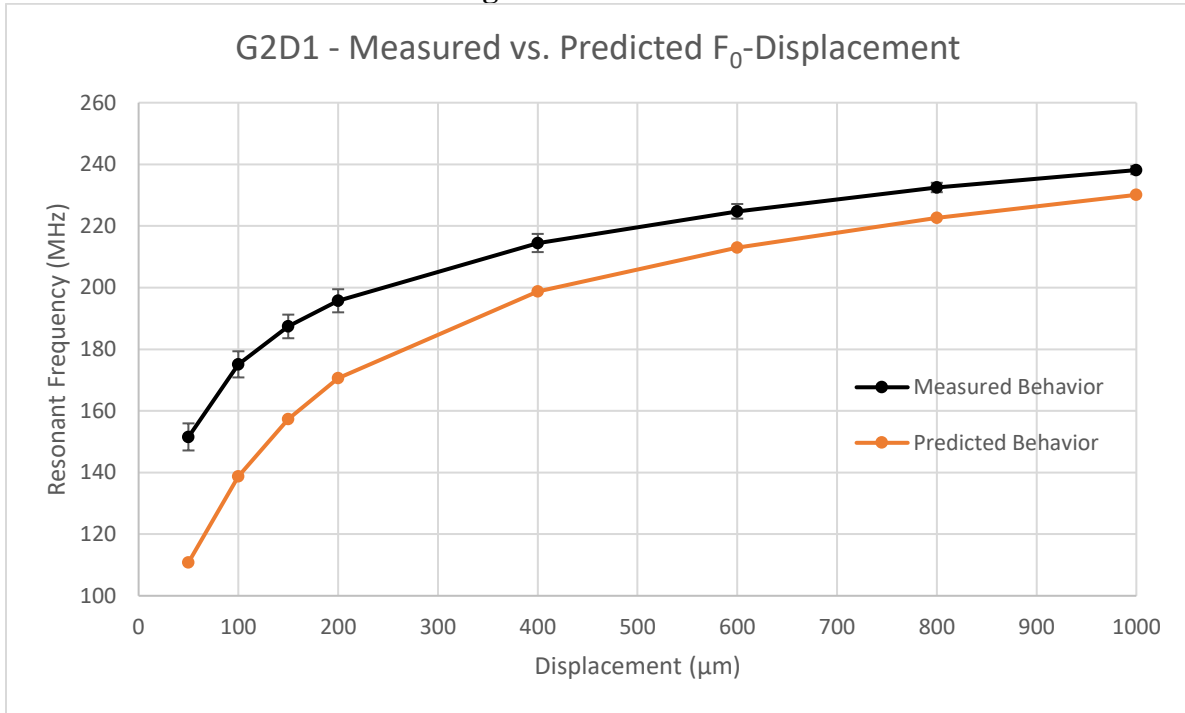


Figure 76: G2D1 air sensor. Error bars show one standard deviation based on three measurements.

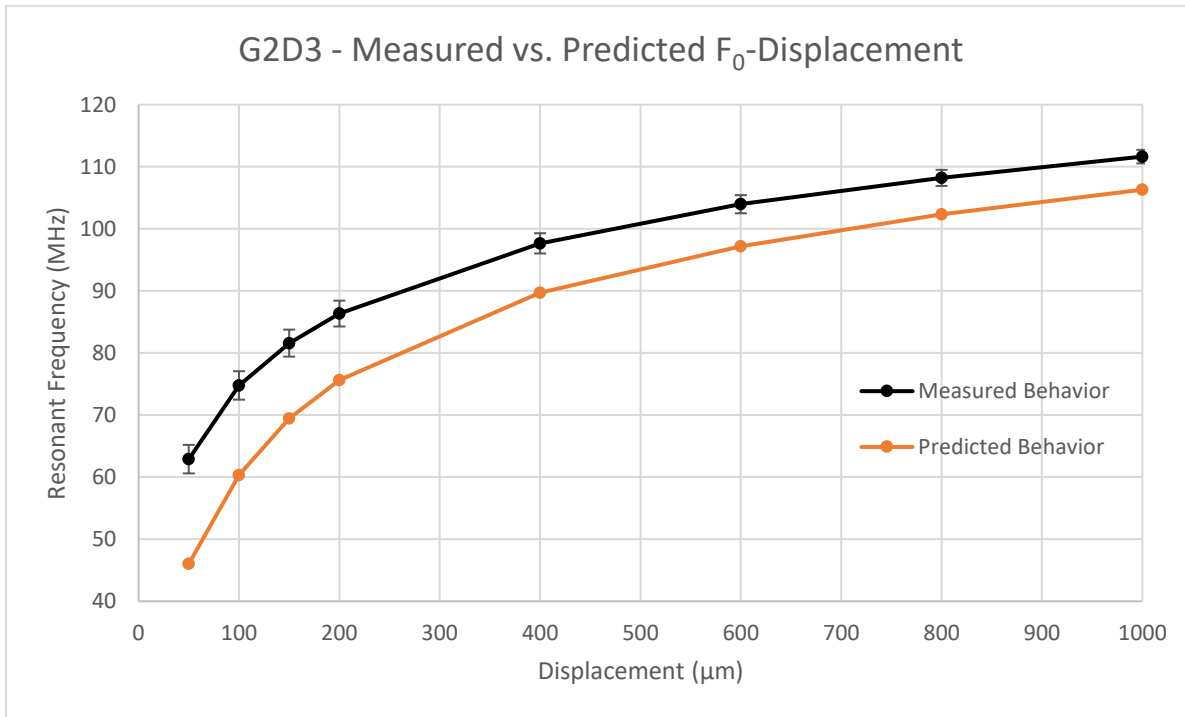


Figure 77: G2D3 air sensor. Error bars show one standard deviation based on three measurements.

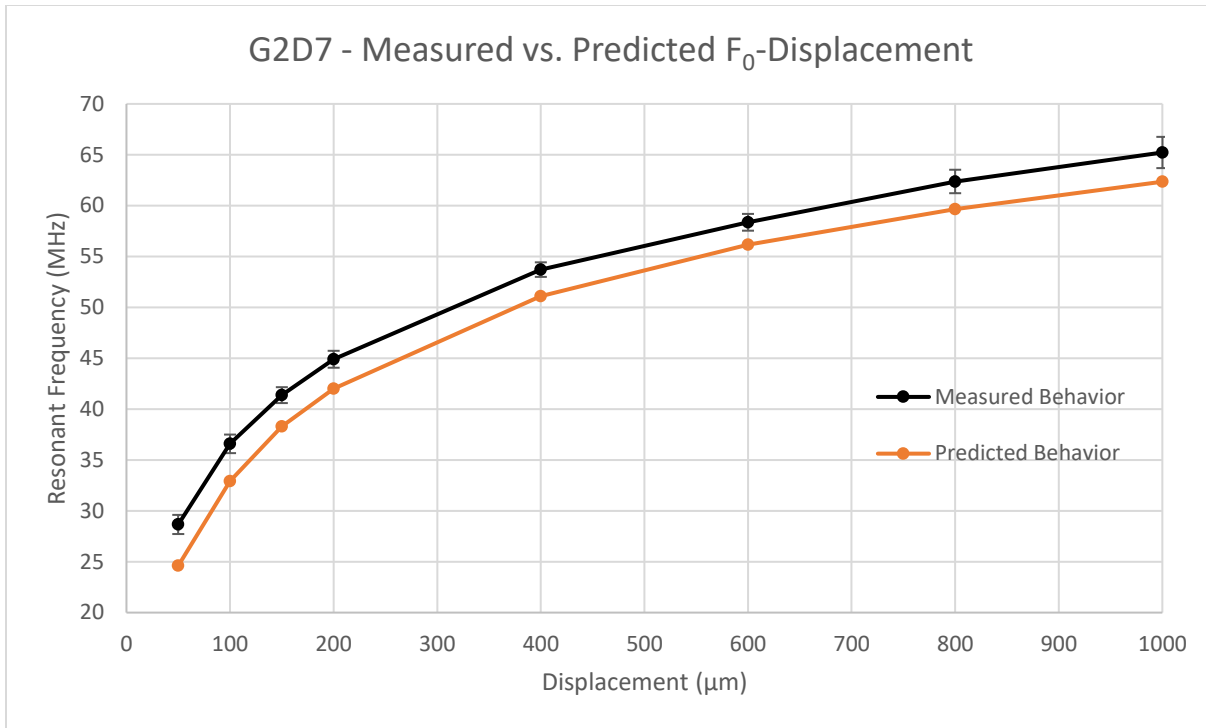


Figure 78: G2D7 air sensor. Error bars show one standard deviation based on three measurements.

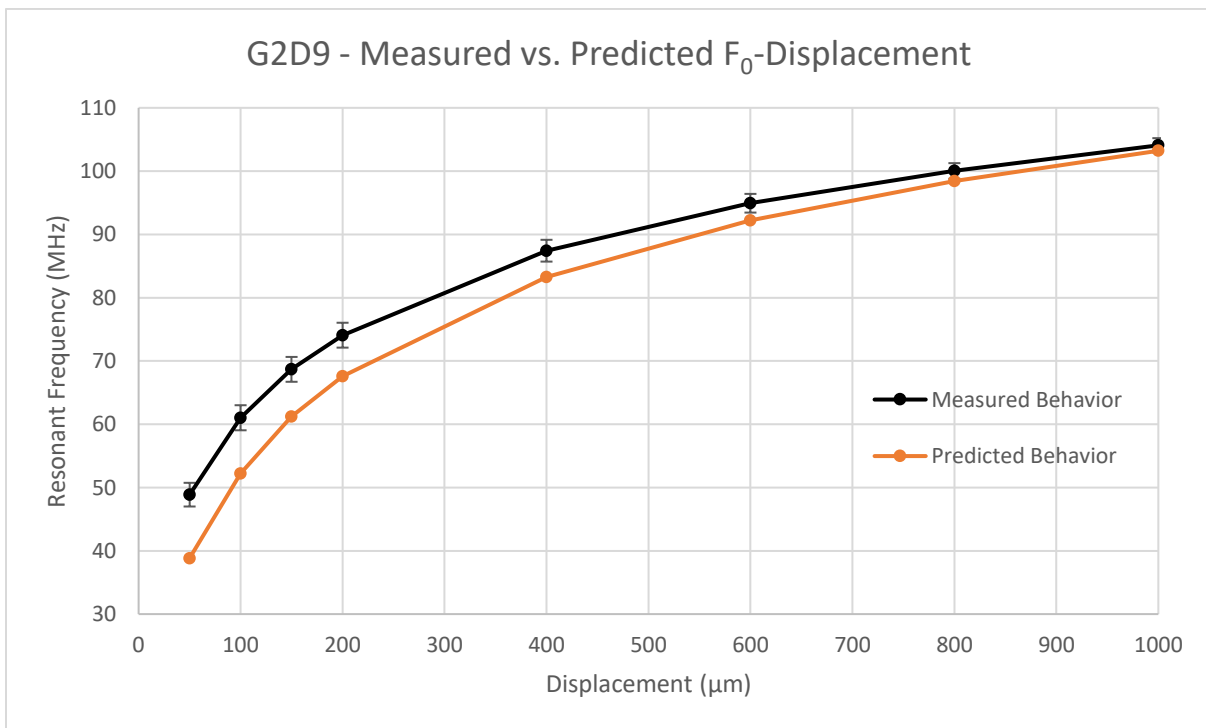


Figure 79: G2D9 air sensor. Error bars show one standard deviation based on three measurements.

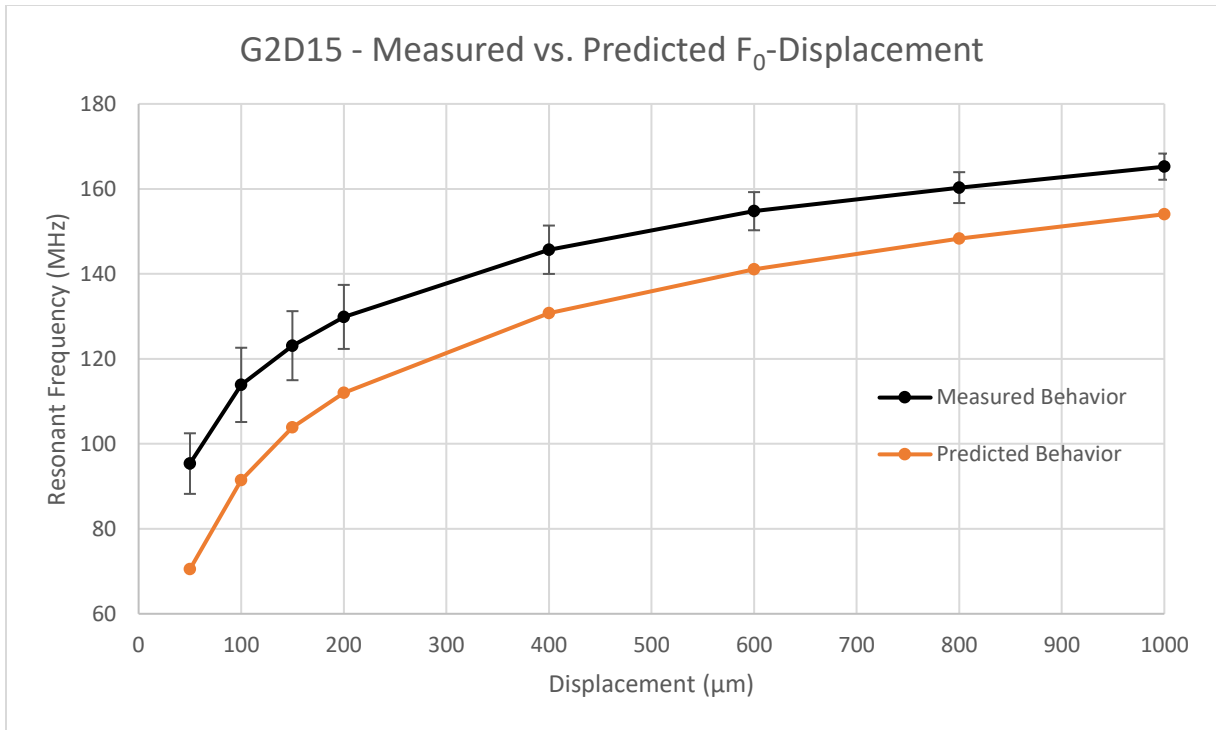


Figure 80: G2D15 air sensor. Error bars show one standard deviation based on three measurements.

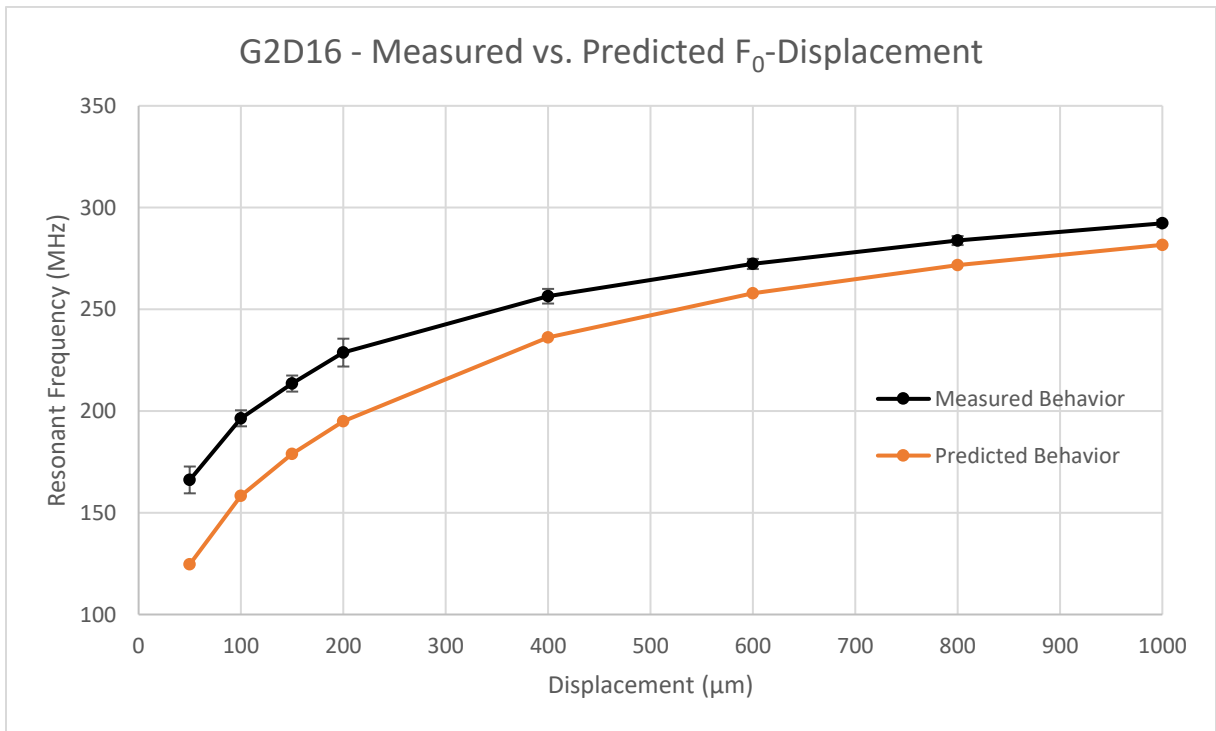


Figure 81: G2D16 air sensor. Error bars show one standard deviation based on three measurements.

A.3 Gen 3 Air Sensor Figures

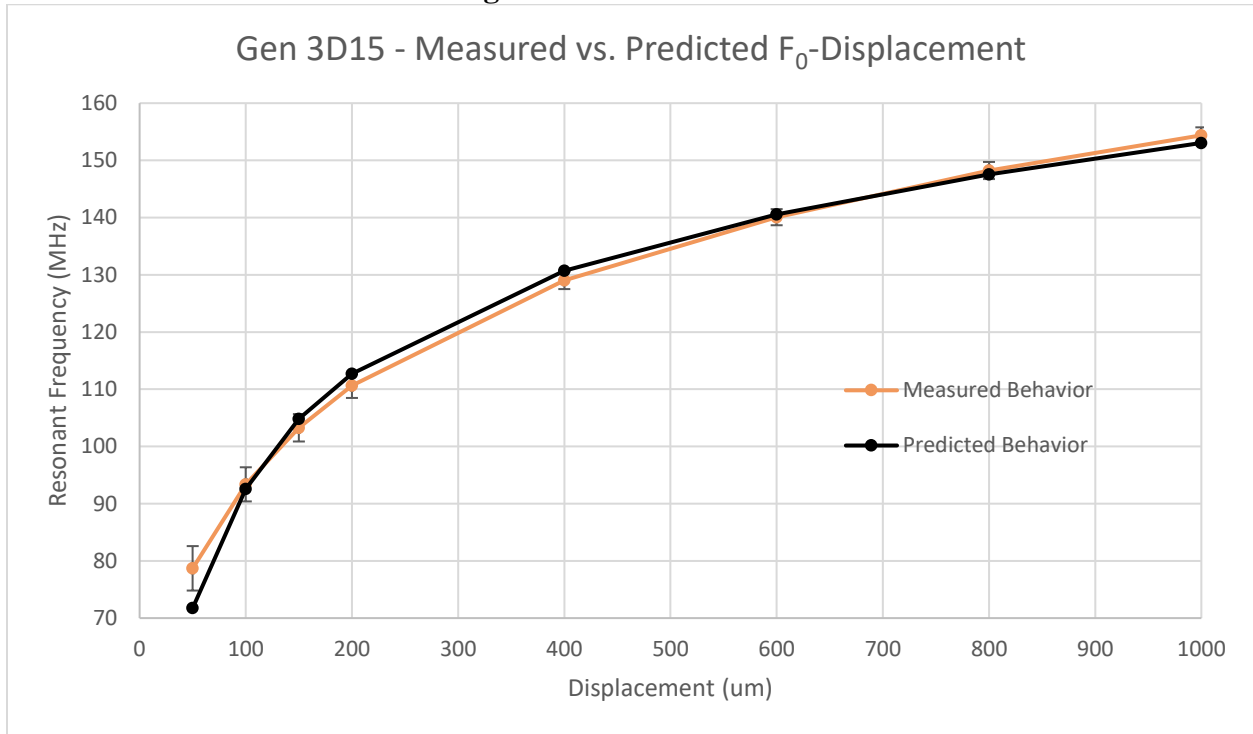


Figure 82: G3D15 air sensor. Error bars show one standard deviation based on three measurements.

A.4 Gen 1 Solid Sensor Figures

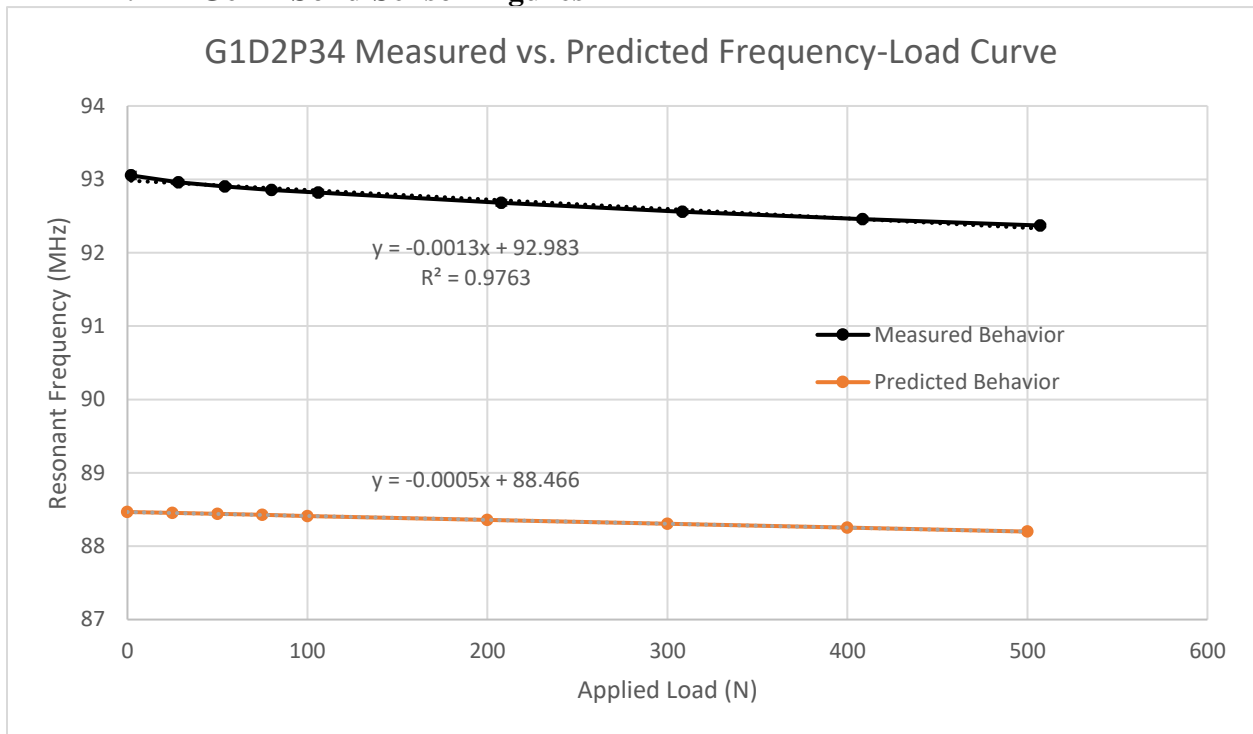


Figure 83: G1D2P34 solid sensor. Error bars show one standard deviation based on three measurements.

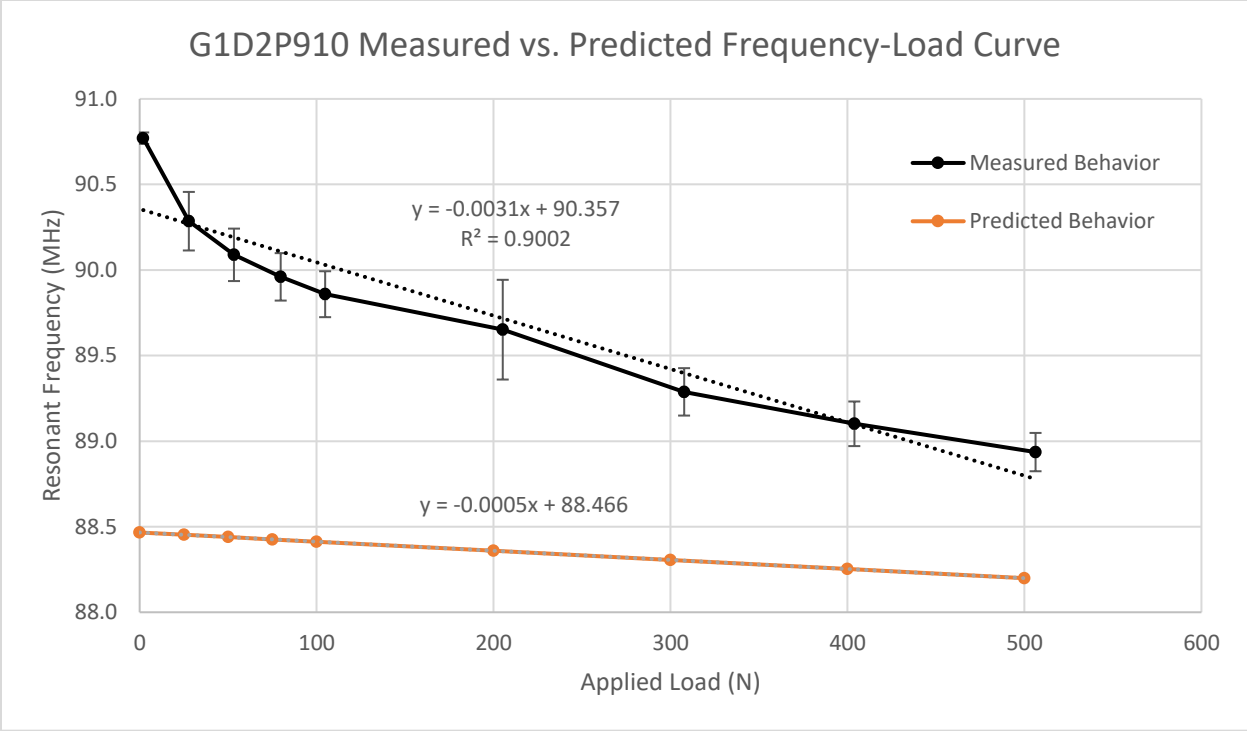


Figure 84: G1D2P910 solid sensor. Error bars show one standard deviation based on three measurements.

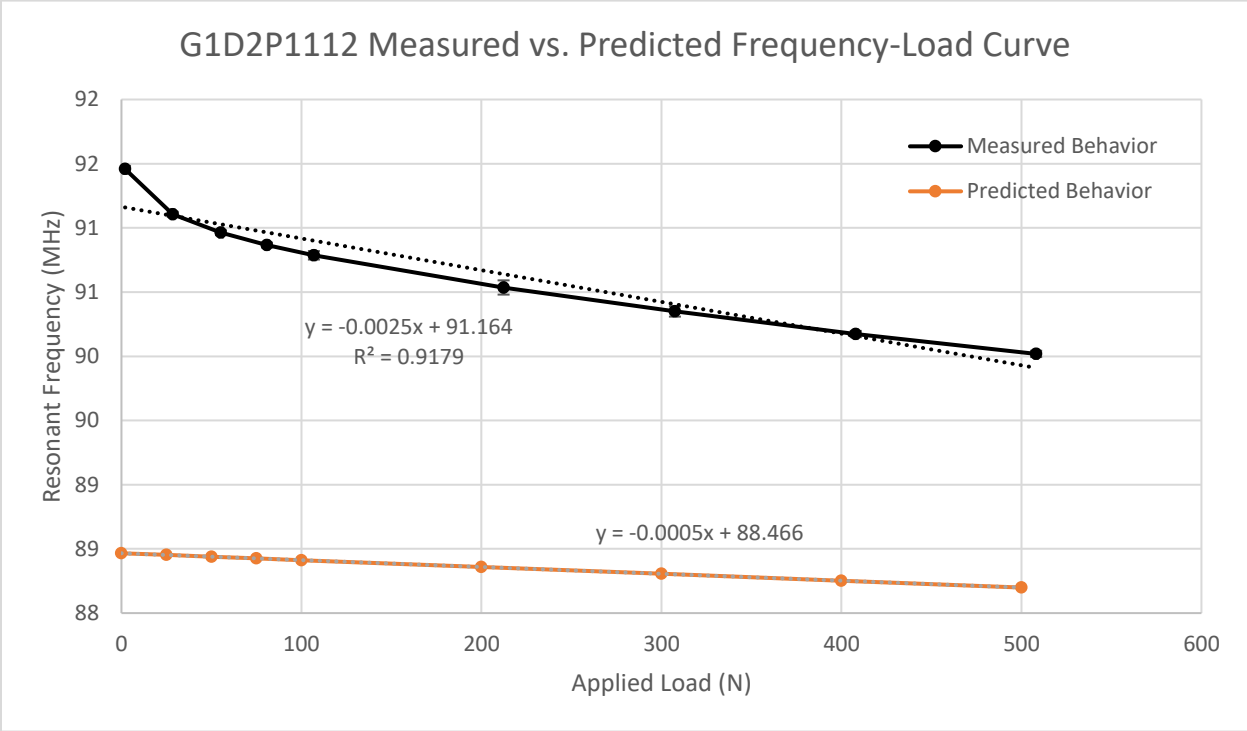


Figure 85: G1D2P1112 solid sensor. Error bars show one standard deviation based on three measurements.

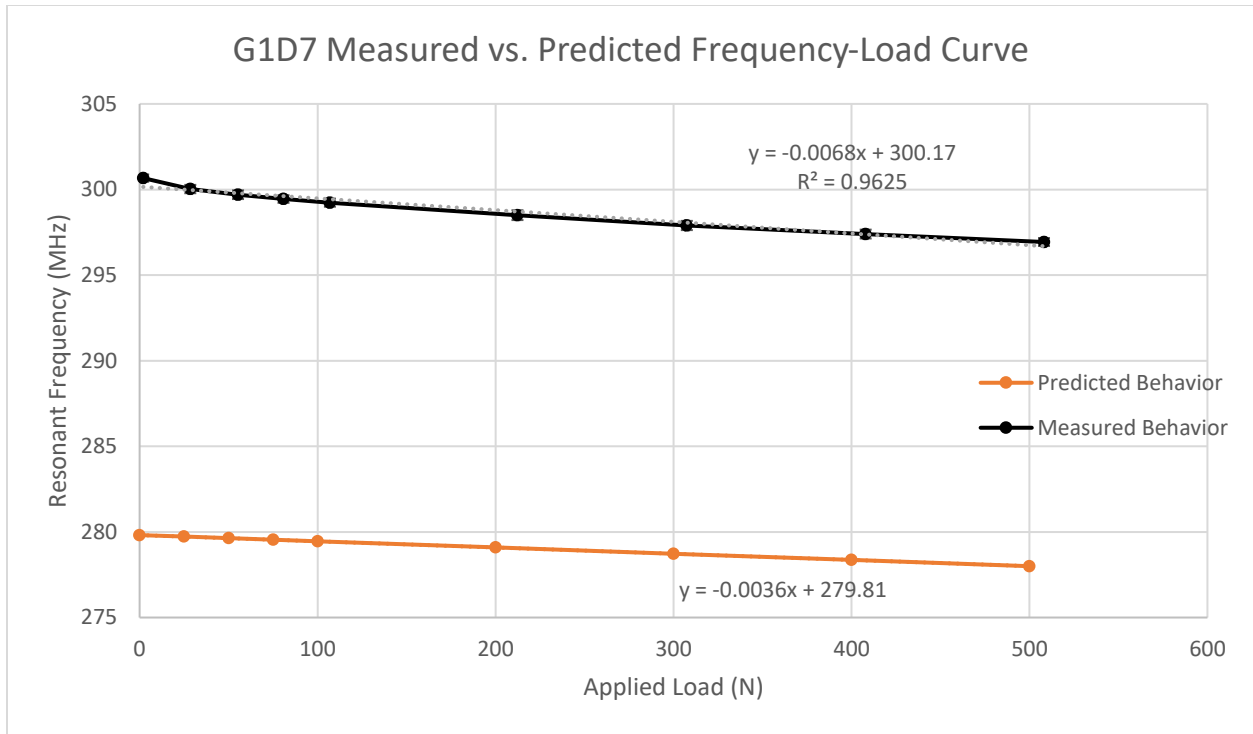


Figure 86: G1D7 solid sensor. Error bars show one standard deviation based on three measurements.

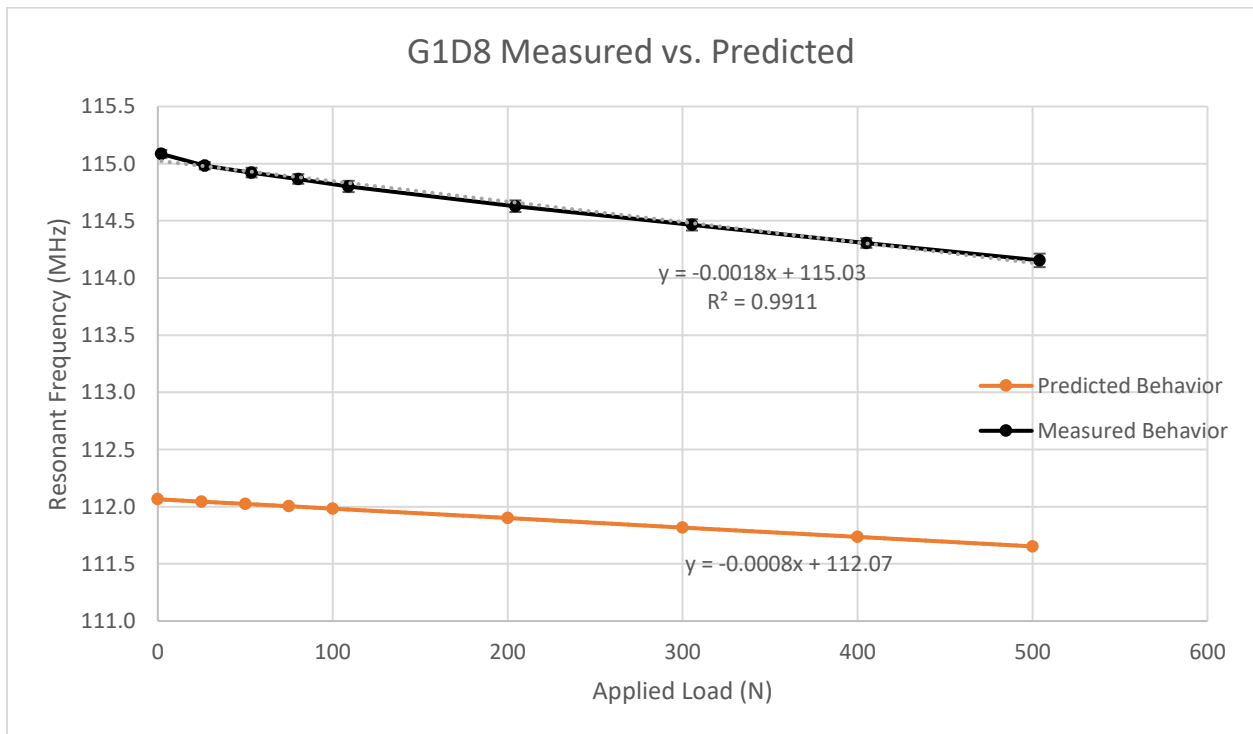


Figure 87: G1D8 solid sensor. Error bars show one standard deviation based on three measurements.

A.5 Gen 2 Solid Sensor Figures

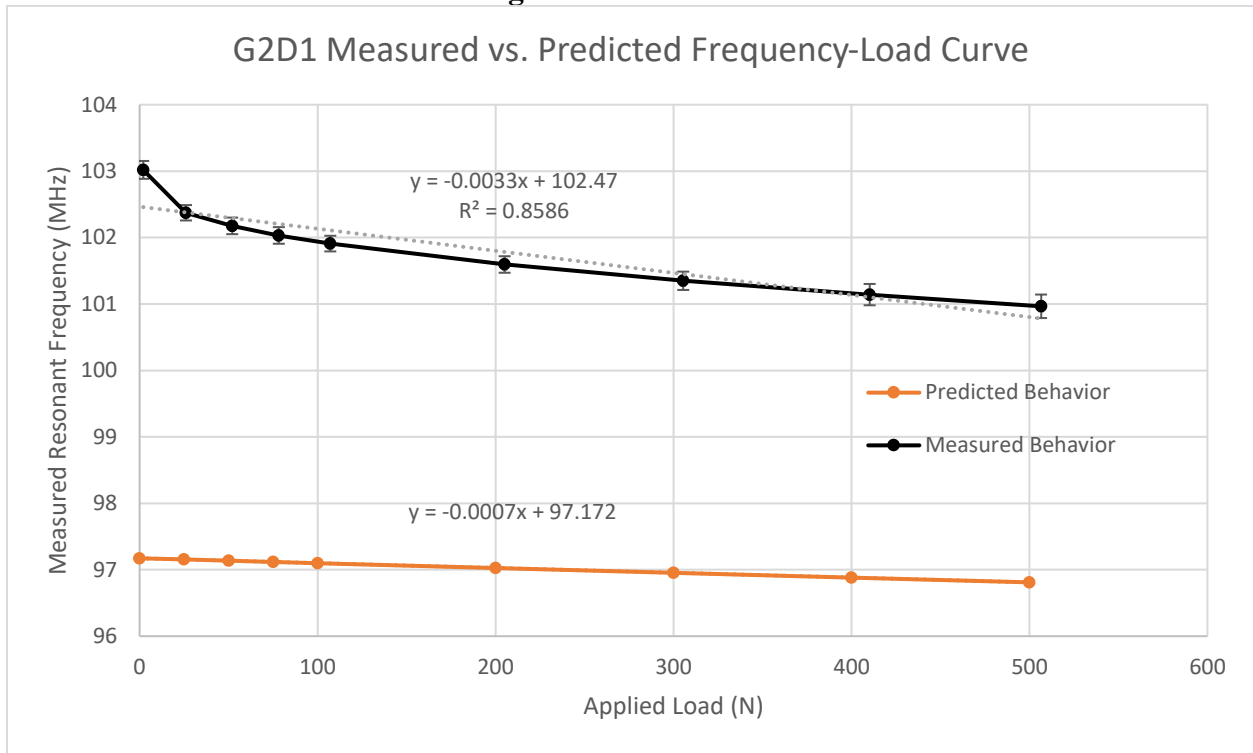


Figure 88: G2D1 solid sensor. Error bars show one standard deviation based on three measurements.

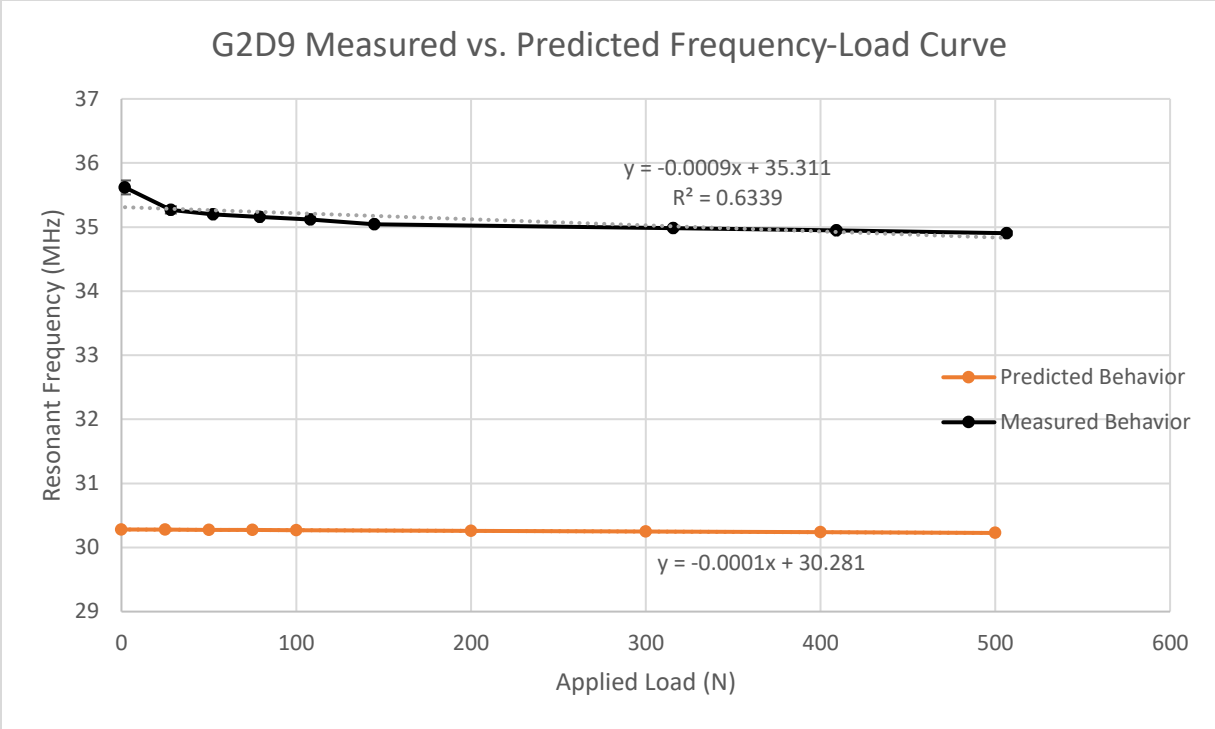


Figure 89: G2D9 solid sensor. Error bars show one standard deviation based on three measurements.

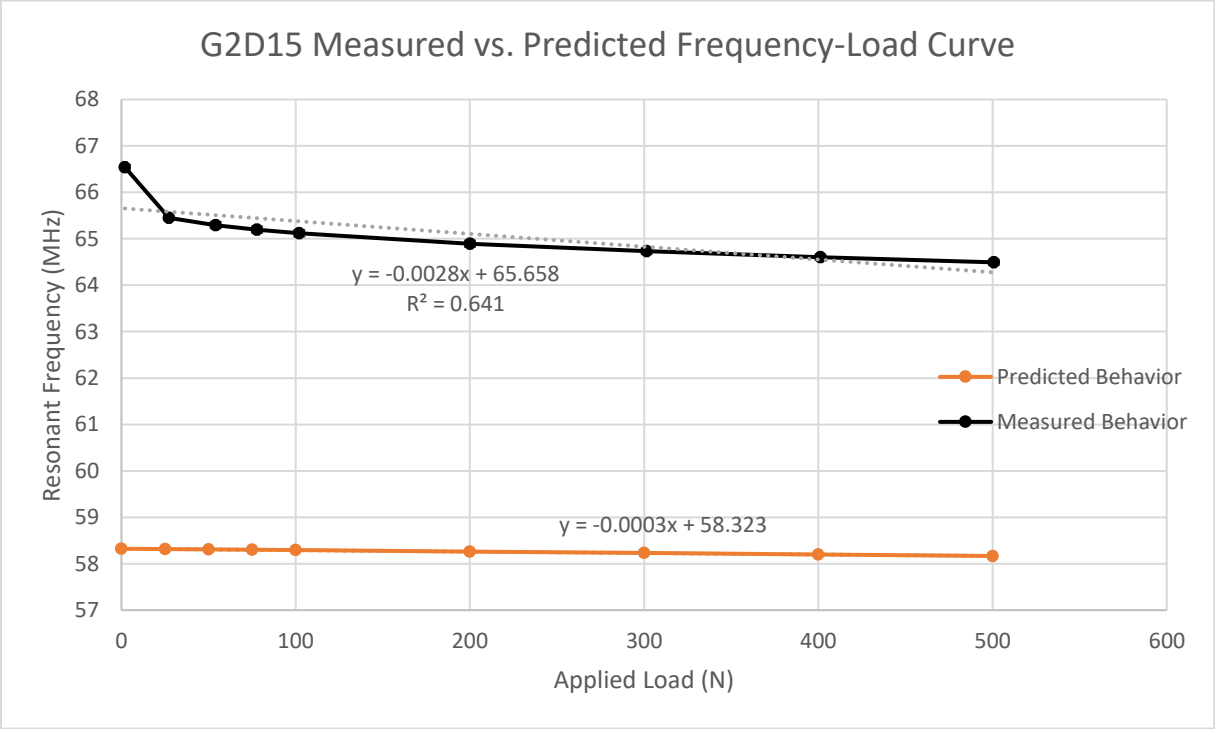


Figure 90: G2D15 – 150 μm solid sensor. Error bars show one standard deviation based on three measurements.

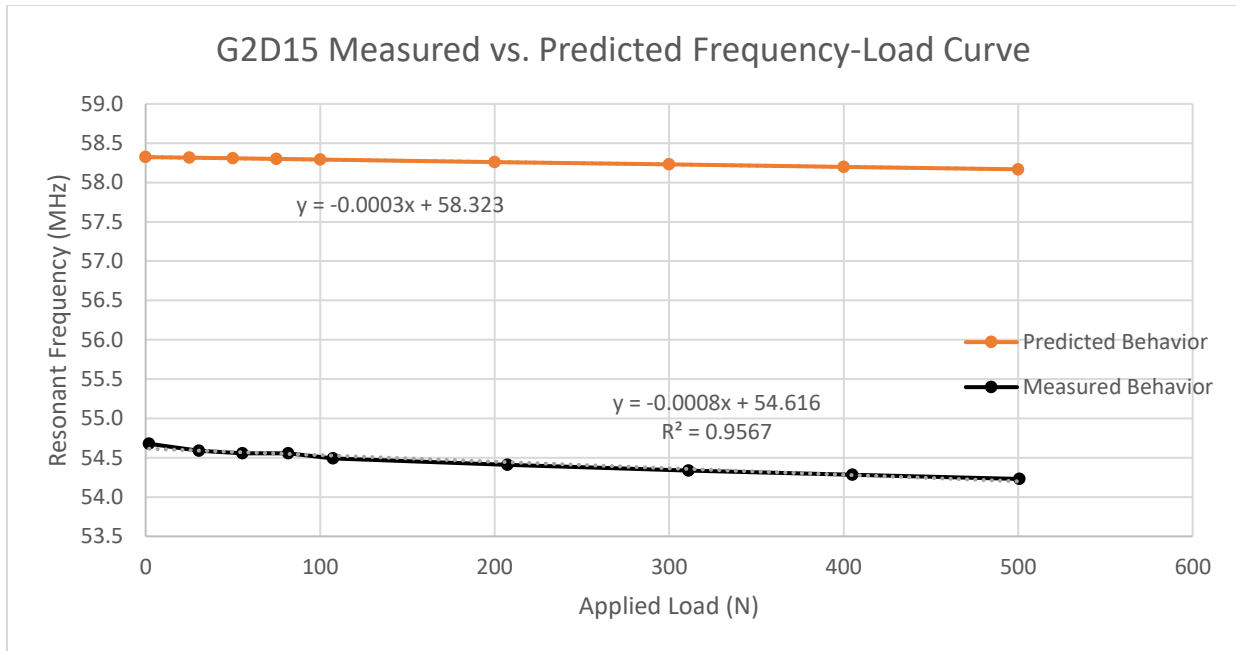


Figure 91: G2D15 – 100 μm solid sensor. Error bars show one standard deviation based on three measurements.

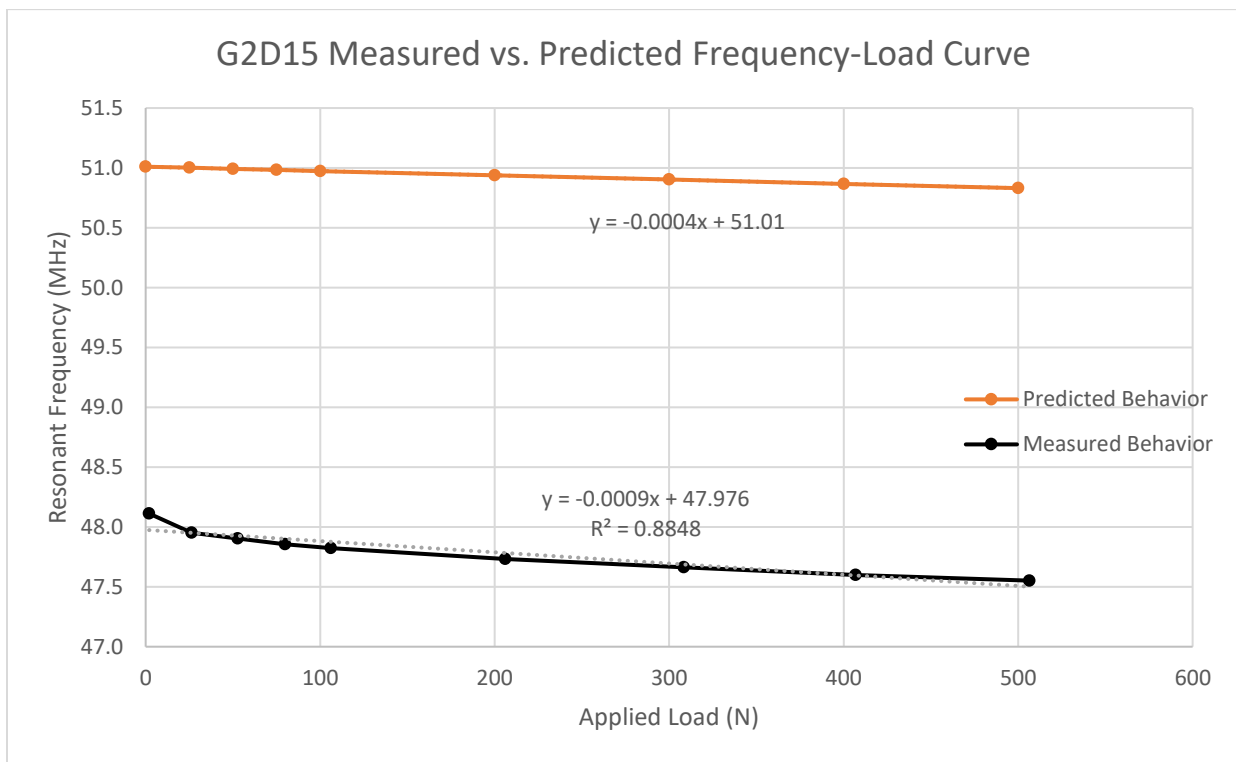


Figure 92: G2D15 – 74 μm solid sensor. Error bars show one standard deviation based on three measurements.

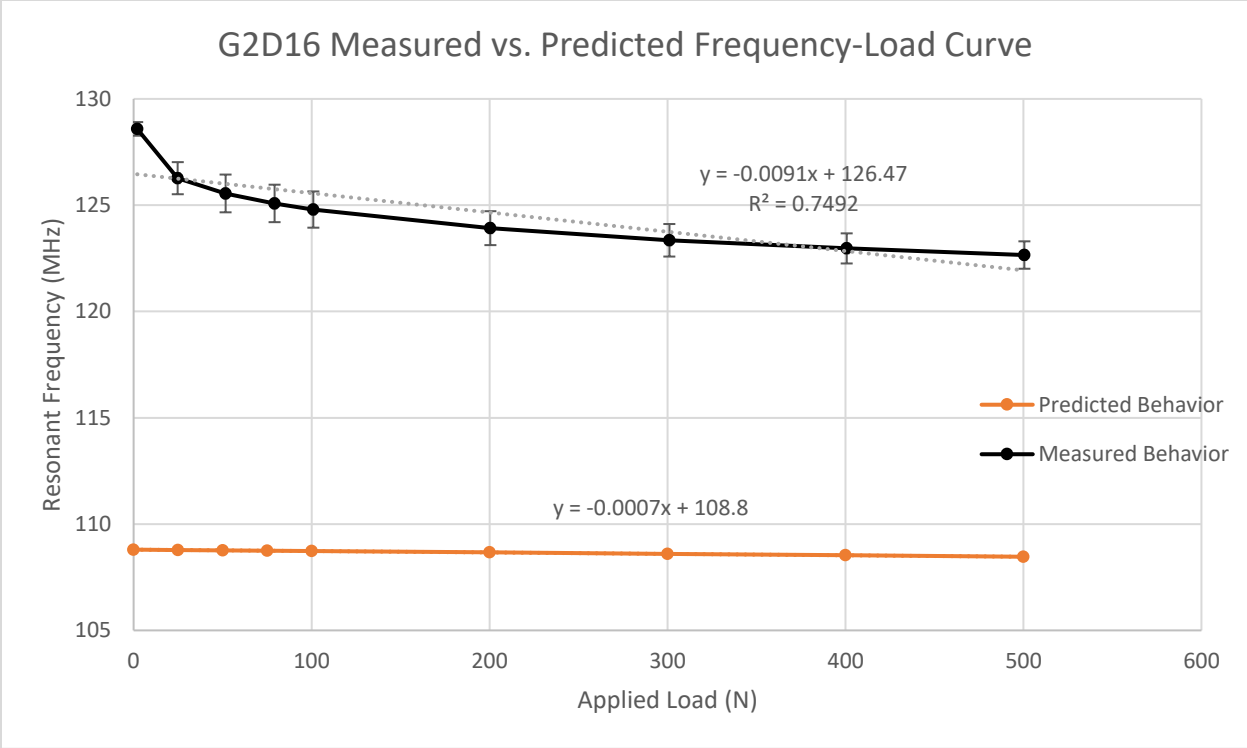


Figure 93: G2D16 solid sensor. Error bars show one standard deviation based on three measurements.

A.6 Gen 3 Solid Sensor Figures

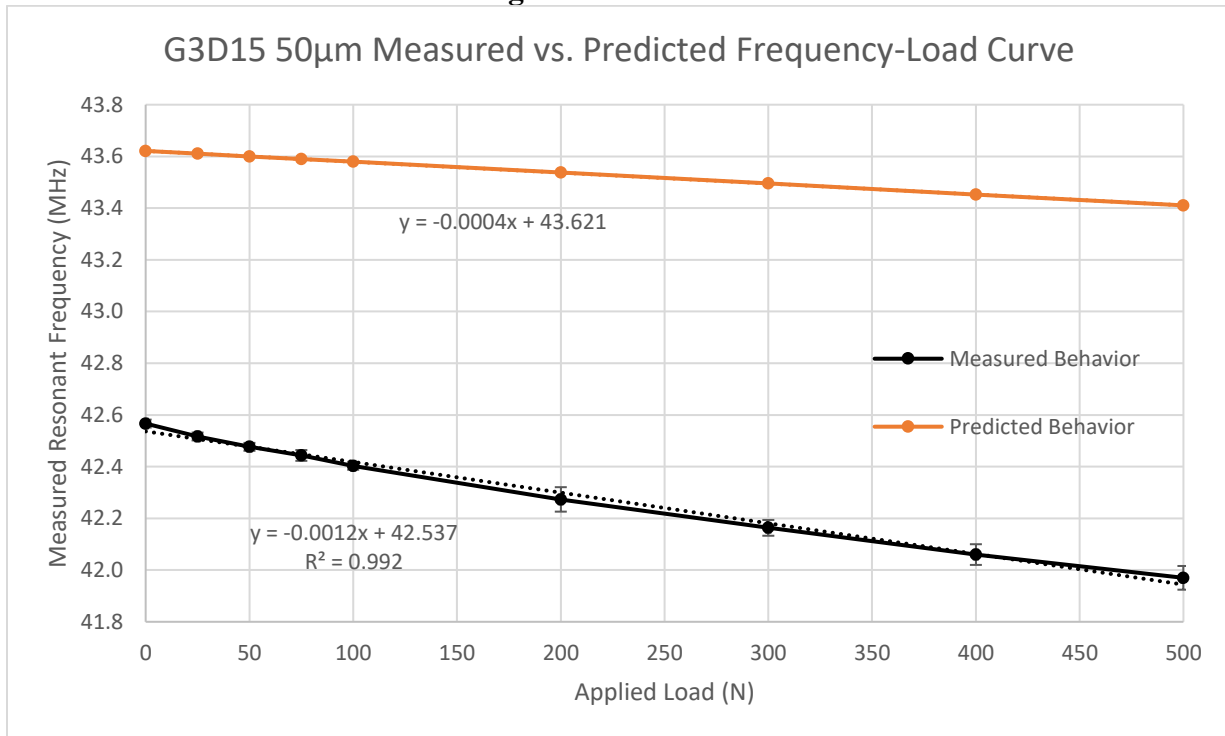


Figure 94: G3D15 – 50 μ m solid sensor. Error bars show one standard deviation based on three measurements.

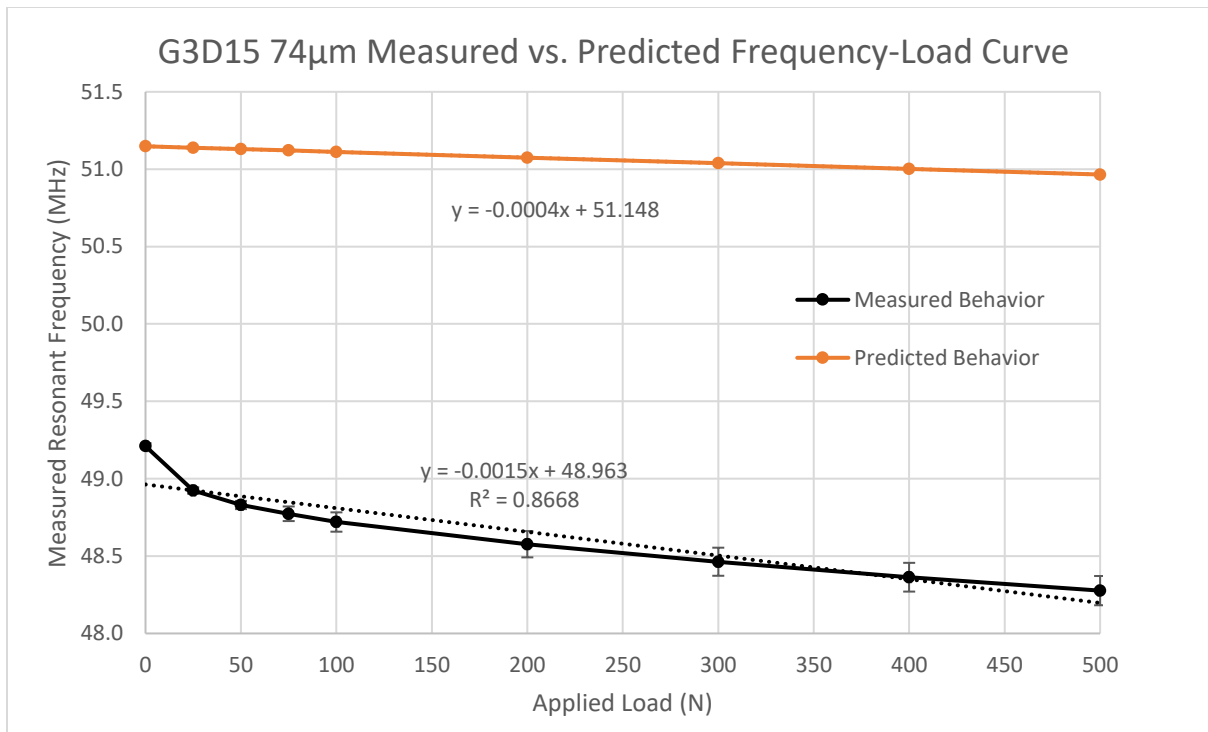


Figure 95: G3D15 – 74 µm solid sensor. Error bars show one standard deviation based on three measurements.

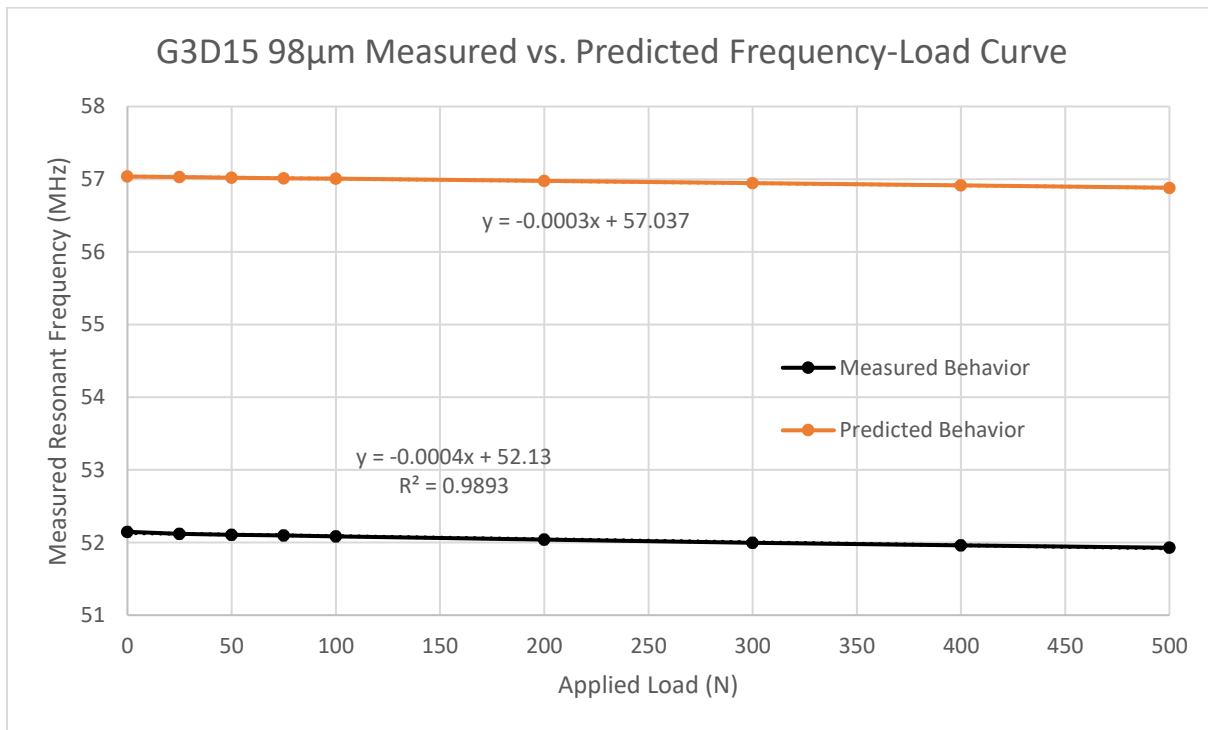


Figure 96: G3D15 – 98 µm solid sensor. Error bars show one standard deviation based on three measurements.

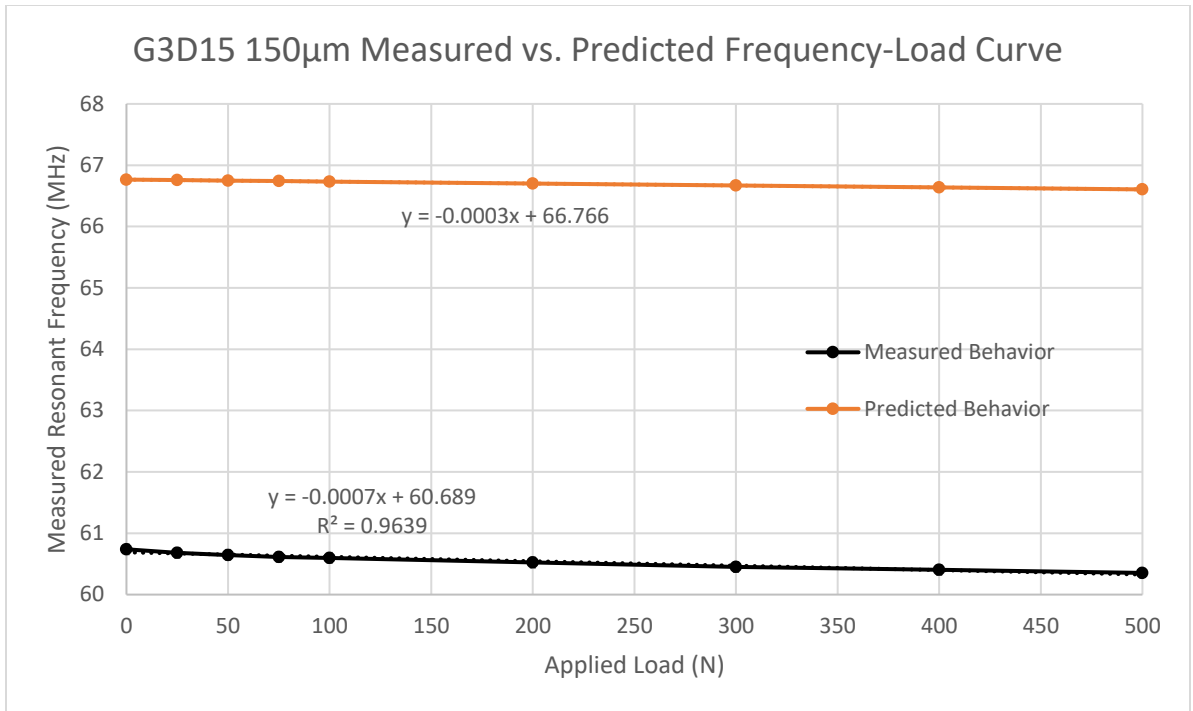


Figure 97: G3D15 – 150 µm solid sensor. Error bars show one standard deviation based on three measurements.

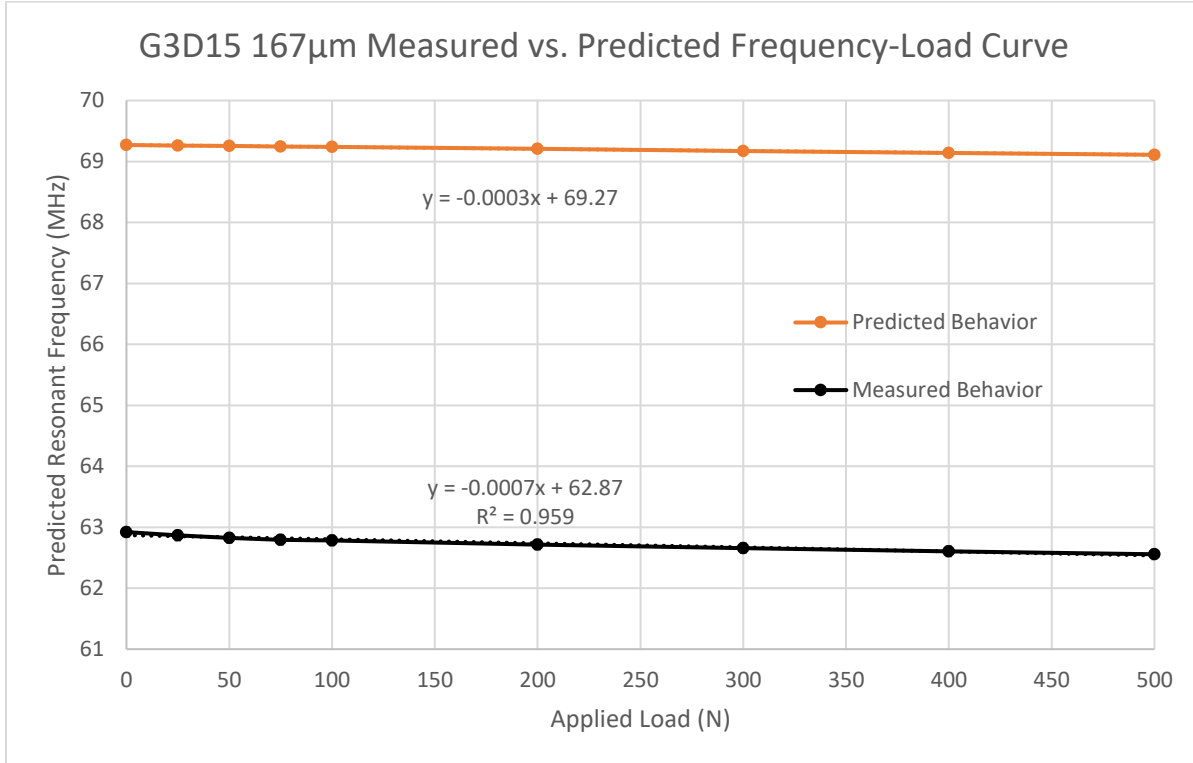


Figure 98: G3D15 – 167 µm solid sensor. Error bars show one standard deviation based on three measurements.

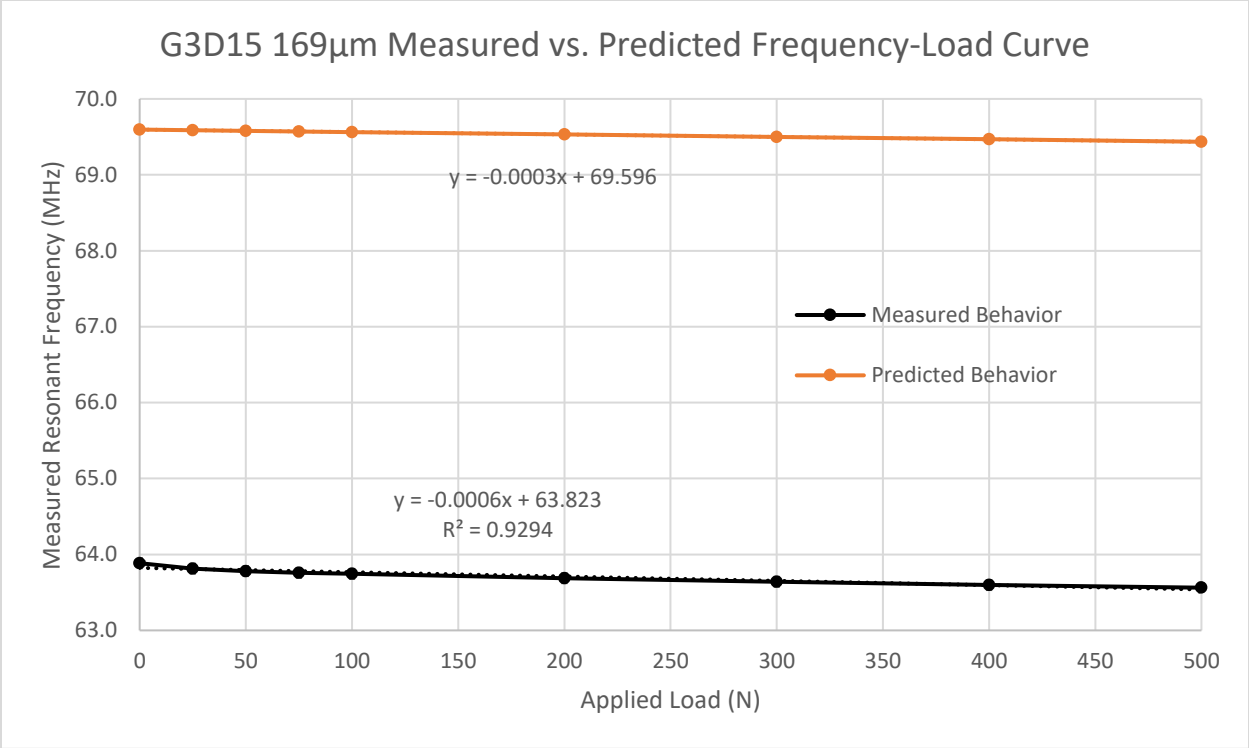


Figure 99: G3D15 – 169 µm solid sensor. Error bars show one standard deviation based on three measurements.

A.7 Gen 1 Sensitivities for Solid Sensors

Table 27: Adjusted sensitivities of first-generation solid sensors. Units are in MHz/N.

Gen 1		
G1D2	G1D7	G1D8
-0.00194	-0.0061	-0.0017

A.8 Gen 2 Sensitivities for Solid Sensors

Table 28: Adjusted sensitivities of second-generation solid sensors. Units are in MHz/N.

Gen 2					
G2D1	G2D9	G2D15 - 74	G2D15 - 105	G2D15 - 150	G2D16
-0.00261	-0.0006	-0.00076	-0.00075	-0.00176	-0.00629

A.9 Gen 3 Sensitivities for Solid Sensors

Table 29: Adjusted sensitivities of third generation solid sensors. Numbers after G3 indicate parylene layer thickness. Units are in MHz/N.

Gen 3					
G3 - 50	G3 - 74	G3 - 98	G3 - 150	G3 - 167	G3 - 169
-0.00114	-0.00122	-0.0004	-0.00065	-0.00059	-0.00048

Appendix B Permissions

B.1 Permissions for Section 1

This file contains license details and terms and conditions for the reproduction of material used in Section 1 of this dissertation.

File Name: Schroeder_2020_Permissions_Section1.zip

File Type: Compressed file (ZIP) containing multiple Portable Document File (PDF) files

File Size: 1526 KB

Required Software: WinRar/7zip and any standard PDF viewer

Special Hardware Requirements: None

B.2 Permissions for Section 5

This file contains license details and terms and conditions for the reproduction of material used in Section 5 of this dissertation.

File Name: Schroeder_2020_Permissions_TanFig20

File Type: Portable Document Format (PDF)

File Size: 293 KB

Required Software: Any standard PDF viewer

Special Hardware Requirements: None